The electrochemistry of zinc in ionic liquids with the trifluoromethylsulfonate anion and their mixtures with water

Doctoral Thesis

(Dissertation)

to be awarded the degree
Doctor rerum naturalium (Dr. rer. nat.)

Submitted by

Zhen Liu

from Nei Mongol, P.R. China

Approved by the Faculty of
Natural and Materials Science
Clausthal University of Technology

Date of Oral Examination: 26. May 2015

Chairperson of the Board of Examiners:

Prof. Dr. Winfried Daum

Chief Reviewer:

Prof. Dr. rer. nat. Frank Endres

Reviewer:

Prof. Dr. Diethelm Johannsmann

The electrochemistry of zinc in ionic liquids with the trifluoromethylsulfonate anion and their mixtures with water

Zhen Liu

Abstract

Ionic liquids have received significant attention as an alternative to conventional electrolytes for metal deposition/dissolution processes due to some favorable properties. A fundamental study of zinc electrodeposition from ionic liquids is important for electroplating processes and for anode materials for rechargeable zinc based batteries.

The electrochemical behavior of zinc in ionic liquids was investigated by cyclic voltammetry and chronoamperometry. The zinc deposits were characterized by scanning electron microscopy (SEM) and X-ray diffraction (XRD). *In situ* scanning tunneling microscopy (STM) is conducted to investigate the initial phase formation of electrodeposited zinc at the electrolyte/electrode interface. The solvation of zinc ions in ionic liquids and in ionic liquid+water mixtures was investigated by FTIR and Raman spectroscopy.

- The ionic liquids 1-ethyl-3-methylimidazolium trifluoromethylsulfonate ([EMIm]TfO) and 1-butyl-1-methylpyrrolidinium trifluoromethylsulfonate ([$Py_{1,4}$]TfO) were chosen for the investigation of zinc electrodeposition. The electrochemical behavior of Zn/Zn(II) in the ionic liquids was studied as a function of deposition overpotential, temperature and water content. The influence of an additive on the deposition of zinc was also investigated.

- Nanostructured zinc matrix, such as free-standing zinc nanowires and macroporous zinc, were synthesized as well. Such materials might be potential anode candidates for future generation lithium ion batteries. An ionic liquid-based polymer gel electrolyte was prepared by combining the ionic liquid [$Py_{1,4}$]TfO, with $Zn(TfO)_2$ and poly(vinylidene fluoride-co-hexafluoropropylene) (PVdF-HFP). The ionic liquid polymer gel electrolyte exhibits high conductivity and good mechanical stability, allowing a quasi-reversible zinc deposition/stripping.

- *In situ* STM results indicate that the structure of [EMIm]TfO on Au(1 1 1) is rather complex. Furthermore, the addition of $Zn(TfO)_2$ changes the interfacial structure significantly. The first STM-probed Zn islands appear at +0.3 V vs. Zn, and their growth leads to the formation of a thin zinc layer. A bulk deposition of Zn is observed with *in situ* STM at −0.1 V vs. Zn. Furthermore, *in situ* STM reveals that the deposition of Zn is accompanied by the formation of Au-Zn surface alloys.

- The solvation of zinc ions in ionic liquids and in ionic liquid+water mixtures was studied by FT-IR and Raman spectroscopy. The structure and physicochemical properties of the ionic liquids is strongly dependent on the interactions between cations, anions and water. The average coordination number of TfO^- per Zn^{2+} cation is different in two ionic liquids due to the different interactions between cations and anions. Zinc ions interact preferentially with water in ionic liquid+water mixtures, leading to aqueous zinc species.

Foreword

The present document is a thesis consisting of a general introduction and a summary of the eight following articles:

[A] Electrodeposition of zinc films from ionic liquids and ionic liquid/water mixtures, Z. Liu, S. Zein El Abedin, F. Endres, *Electrochimica Acta*, 2013, **89**, 635–643.

[B] Template-assisted electrodeposition of highly ordered macroporous zinc structures from an ionic liquid, Z. Liu, A. Prowald, S. Zein El Abedin, F. Endres, *Journal of Solid State Electrochemistry*, 2013, **17**, 1185–1188.

[C] Electrochemical synthesis of vertically aligned zinc nanowires using track-etched polycarbonate membranes as templates, Z. Liu, S. Zein El Abedin, M. Shapouri Ghazvini, F. Endres, *Physical Chemistry Chemical Physics*, 2013, **15**, 11362–11367.

[D] Electrodeposition of zinc-copper and zinc-tin films and free-standing nanowire arrays from ionic liquids, Z. Liu, S. Zein El Abedin, F. Endres, *ChemElectroChem*, 2015, **2**, 389–395.

[E] Influence of an additive on zinc electrodeposition in the ionic liquid 1-ethyl-3-methylimidazolium trifluoromethylsulfonate, Z. Liu, S. Zein El Abedin, N. Borisenko, F. Endres, *ChemElectroChem*, DOI: 10.1002/celc.201500108.

[F] Electrodeposition and stripping of zinc from an ionic liquid polymer gel electrolyte for rechargeable zinc-based batteries, Z. Liu, S. Zein El Abedin, F. Endres, *Journal of Solid State Electrochemistry*, 2014, **18**, 2683–2691.

[G] *In situ* STM study of zinc electrodeposition on Au (111) from the ionic liquid 1-ethyl-3-methylimidazolium trifluoromethylsulfonate, Z. Liu, N. Borisenko, S. Zein El Abedin, F. Endres, *Journal of Solid State Electrochemistry*, 2014, **18**, 2581–2587.

[H] Raman and FT-IR spectroscopic studies of 1-ethyl-3-methylimidazolium trifluoromethylsulfonate, its mixtures with water and the solvation of zinc ions,
Z. Liu, S. Zein El Abedin, F. Endres, *ChemPhysChem*, 2015, **16**, 970–977.

Content

3 Results and discussion

1 Introduction

1.1 Ionic liquids

Ionic liquids are salts in liquid state at temperatures < 100 ℃, which consist of entirely ions. The cation and anion of the ionic liquids are usually poorly coordinated, resulting in melting points of these solvents usually below 100 ℃, or even at room temperature.

The history of ionic liquids is widely regarded as starting from the synthesis of ethylammonium nitrate reported in 1914 by Walden [1]. In the 1950s the first room temperature ionic liquids (RTIL) based on $AlCl_3$ were reported [2]. Such RTILs have been widely studied as solvents for conducting various reactions and as electrolytes for electrodeposition of Al. However, this kind of RTIL is moisture sensitive. Another type of ionic liquids, with imidazolium or pyridinium cations, and halide or tetrafluoroborate anions, has been extensively studied since the late 1970s [3-5]. They were initially developed as electrolytes in battery applications. In the last decades, a large number of air and water stable ionic liquids was prepared and used as solvents [6-10], furthermore attention has been paid towards the development of less toxic ionic liquids with *e.g.* ammonium cations.

The combination of a huge amount of cations and anions leads to a theoretical number of 10^{18} ionic liquids. Typical structures of cations and anions are shown in Fig. 1.1.1.

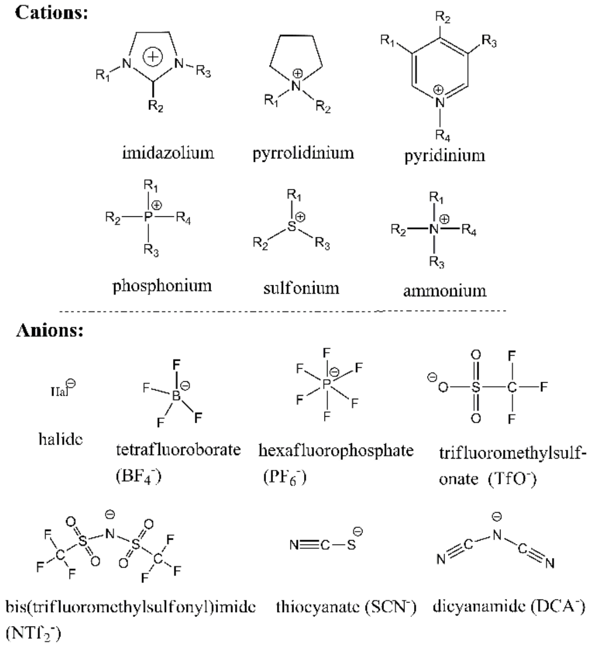

Fig. 1.1.1 *Some cations and anions of common ionic liquids.*

1.2 Some physical properties of ionic liquids

Ionic liquids (ILs) exhibit many attractive physicochemical properties, including negligible vapor pressure, low flammability, high thermal stabilities and large electrochemical windows, which make them suitable in numerous task-specific applications [9, 11-14]. The properties of ionic liquids, such as melting point, viscosity, and conductivity, can be controlled by the selection of suitable cations and anions. Therefore, ionic liquids are often termed as "designer solvents".

1.2.1 Melting point

Ionic liquids have quite low melting points compared with classical inorganic salts. NaCl has a melting point of 800 ℃, due to strong electrostatic interactions and the correspondingly high lattice energy of the salt. However, ionic liquids such as [EMIm]Cl and [BMIm]Cl, have a melting point of 87 ℃ and 65 ℃, respectively [15]. The good distribution of charge by the organic cations results in a reduction of the electrostatic interactions between the ions, which in turn results in a reduction in the melting point of the salt. The melting point of the ionic liquids is governed by both the cationic species and the anionic species. The interaction strength between cations and anions also affects the melting point. Cations with low symmetry, weak intermolecular interaction and a good distribution of charge generally favor low melting points.

1.2.2 Thermal stability

Ionic liquids are thermally stable because of their very high decomposition temperature (up to 300 ℃). Ionic liquids have a very large liquid range (*e.g.* $[C_4mim][NTf_2]$: −89 to 450 °C [16]) and very low vapor pressure. That allows the applications of ionic liquids at high temperature as solvent for organic reactions at high temperature, thermal energy storage, heat-transfer fluids and high-temperature lubricants [17-20].

1.2.3 Viscosity and conductivity

Ionic liquids have usually a higher viscosity than aqueous solutions. The higher viscosity of the ionic liquid results in lower diffusion coefficients. The viscosities of the ionic liquids are typically in the range of 10–500 mPas [21-23]. Increasing temperature can effectively reduce the viscosity by more than one order of magnitude. Different cations and anions and their interactions have a strong effect on the viscosity. The interactions are a result of a subtle balance between Coulomb forces, hydrogen bonds and dispersion forces. The conductivity of ionic liquids is inversely proportional to viscosity, generally being greater than that of organic solvents/electrolyte systems. The conductivity depends both on the number of charge carriers and on their mobility. The conductivity of an ionic liquid is also strongly dependent upon temperature.

1.2.4 Electrochemical windows

Ionic liquids have larger electrochemical windows than aqueous solution. Water has an electrochemical window of only about 1.2 V, while, ionic liquids have a significantly larger electrochemical window, *e.g.*, 5.7 V for 1-butyl-1-methylpyrrolidinium trifluoromethylsulfonate, $[Py_{1,4}]TfO$ on Au(1 1 1) electrode, and 5.5 V for 1-butyl-1-methylpyrrolidinium bis(trifluoromethylsulfonyl)amide $[Py_{1,4}]Tf_2N$ on glassy carbon [24]. A large number of pure metals and alloys, including reactive and refractory metals and semiconductors which cannot be deposited from aqueous solutions can be deposited from ionic liquid solutions. As shown in Fig. 1.2.1, the electrodeposition of metals like Al, Nb, semiconductors like Si, Ge and polymers like poly(3,4-ethylenedioxythiophene) (PEDOT), poly(para-phenylene) (PPP) can be synthesized in ionic liquids [25].

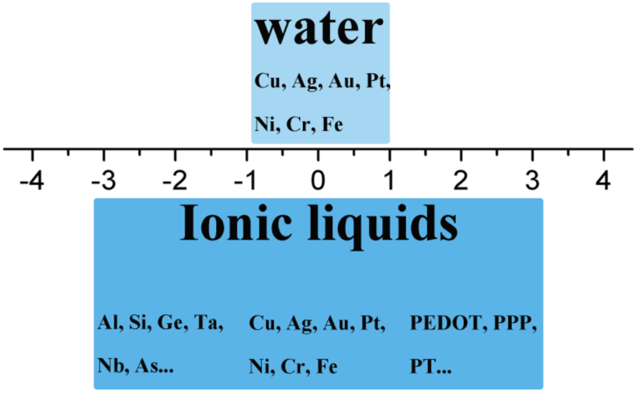

Fig. 1.2.1 *The electrochemical windows of water and ionic liquids with possible deposits. PEDOT: poly(3,4-ethylenedioxythiophene), PPP: poly(paraphenylene), PT: polythiophene.*

1.3 Electrodeposition from ionic liquids

The electrodeposition of many metals and alloys can be achieved from aqueous solutions, such as copper, zinc, silver, gold, nickel and chromium, which are largely used in electrorefining, decoration, corrosion protection and other functional surface finishings. However, some of the deposition processes are based on toxic solution (*e.g.*, cyanide, strong acidic and alkaline solution) and have rather low current efficiencies (*e.g.*, chromium).

Furthermore, electroplating of a range of elements, such as, aluminum, magnesium, tantalum, silicon, germanium and gallium, cannot be achieved in aqueous baths due to hydrolysis of water. The electrodeposition of metals and alloys from ionic liquids has gained much attention in the recent years due to their advantageous physicochemical properties, which makes them interesting alternatives to aqueous electrolytes for electrodeposition [25-28]. Ionic liquids have an electrochemical window of up to ± 3 V vs. NHE, which makes them interesting candidates for the electrodeposition of not only reactive metals and semiconductors but also polymers. Furthermore, ionic liquids are well suited to perform at elevated temperatures due to their low vapor pressures. Most importantly, they have a wide range of solubility for metal salts or molecular compounds. Most ionic liquids are nonflammable and nontoxic, thereby providing key environmental advantages when compared to organic solvents. First generation ionic liquids based on $AlCl_3$ were extensively studied for electrodeposition due to their high conductivity, wide potential windows and excellent solvation power for many metal salts. Metals such as, Al, Fe, Co, Cu, Pd, Ag, Au, Sn, Te, Cr and Zn can be deposited from them [25]. However, one disadvantage of such liquids often is their sensitivity to air and water, therefore experiments must be carried out under inert gas conditions or at least under dry air. For this reason, air and water stable ionic liquids were explored for electrodeposition. The research group of Sun in Taiwan developed chlorozincate ionic liquids for the electrodeposition of metals, like Al, Zn, Cu, Ni, Sn and alloys such as Cu-Zn, Zn-Sn, Co-Ni [29-35]. The research group of Abbott (Leicester University) studied the deposition of metal and alloys from deep eutectic solvents based on the mixture of choline chloride with urea, or with ethylene glycol, glycerol and propylene glycol [27, 36-40]. Compared to real ionic liquids, this kind of solvents is much cheaper and easier to prepare. The research group of Endres focused on air and water stable ionic liquid for metals deposition such as Zn, Sn, Cu, Li, Nb and Fe, semiconductors such as Si, Ge, Si_xGe_{1-x}, Ga and In, polymers such as PEDOT and PPP [41-45]. Although there have been many publications in this area, much efforts are still needed to fully understand the relationship between the metal speciation, the electrodeposition mechanism and the deposit morphology.

1.4 Electrodeposition of zinc from ionic liquids

1.4.1 Pure ionic liquids

The electrochemical deposition of zinc and its alloys is of great practical importance and widely used in the field of corrosion-resistant coatings and energy storage devices, like Zn batteries, *e.g.* Traditionally, zinc plating is performed in cyanide baths, in alkaline cyanide free baths and in acid zinc chloride baths. Such electrolytes are toxic, quite corrosive and can possibly have a negative impact on the environment. Therefore it is of interest to find alternative electrolytes for zinc deposition.

The electrodeposition of Zn and its alloys from ionic liquids has attracted attention in the recent years. In water, the electrodeposition of zinc and its alloys is usually accompanied by hydrogen evolution and often low current efficiencies result. Problems associated with hydrogen evolution can in principle be avoided by employing ionic liquids as they can be made water free. For example, high quality deposits of metals like Au, Pt and Pd and their alloys can be made in ionic liquids without evolution of hydrogen [27].

The electrodeposition of Zn was studied in a range of ionic liquids, particularly from $AlCl_3$-based ionic liquids [46] and air and water stable chloro-zincate ionic liquids [47, 48]. The reducible zinc species in the chlorozincate ionic liquids were found to be coordinately unsaturated species like $ZnCl_5^{3-}$, $Zn_2Cl_7^{3-}$ and $(ZnCl_2)_n$ [49]. As they are easier to prepare and to handle than the corresponding chloroaluminates, the chlorozincates were studied in more detail in the recent decades. Sun *et al.* published a series of papers dealing with Zn and Zn alloy deposition from chloro-zincate ionic liquids [32, 33]. In addition, Abbott *et al.* [38, 50, 51] studied the electrodeposition of Zn from deep eutectic solvents composed of $ZnCl_2$ and choline chloride. Recently, the deposition of zinc from air and water stable ionic liquids, 1-ethyl-3-methylimidazolium and N-butyl-N-methylpyrrolidinium dicyanamides [52-54], 1-butyl-1-methylpyrrolidinium bis(trifluoromethylsulfonyl)imide [55, 56], and 1-butyl-3-methylimidazolium trifluoromethylsulfonate [57] has been reported. In this thesis, the focus is set on the fundamental aspects of zinc deposition from two kinds of ionic liquids, namely 1-butyl-1-methylpyrrolidinium trifluoromethylsulfonate ($[Py_{1,4}]TfO$) and 1-ethyl-3-methylimidazolium trifluoromethylsulfonate ([EMIm]TfO).

1.4.2 Ionic liquid+water mixtures

An advantage of adding water to an ionic liquid is a decrease in viscosity and a subsequent increase in conductivity. Ionic liquid+water mixtures can be considered as potential electrolytes for rechargeable Zn-air batteries. However, an increase in water content can also result in a reduction in the electrochemical window of the ionic liquid. Understanding of the influence of water addition on the physical and electrochemical properties of ionic liquids is critical to the development of suitable electrolyte systems. Simons *et al.* [58] investigated the electrodeposition and dissolution of Zn^{2+} from 1-ethyl-3-methylimidazolium dicyanamide ([EMIm]DCA). The concentration of water was found to be a critical parameter for obtaining a uniform, dendrite-free morphology. The physical and transport properties of the ionic liquid 1-butyl-1-methylpyrrolidinium dicyanamide containing Zn^{2+} and H_2O were also investigated [59]. Mu *et al.* reported an influence of water on the Zn/Zn(II) redox behavior in 1-butly-1-methyl-pyrrolidinium bis(trifluoromethylsulfonyl)imide ionic liquids [60]. Improved Zn/Zn(II) reversibility and enhanced kinetic properties of Zn/Zn(II) redox behavior were observed in the presence of 2.0 wt% of water. The mixtures of ionic liquids with water are of considerable interest and it is possible to tune the properties of electrolytes to produce dendrite-free morphology and reversible Zn/Zn(II) redox behavior for application in rechargeable zinc based batteries.

1.4.3 The influence of additives on zinc deposition

In order to improve the deposit morphology and physical performance, the additives are often present in the electrodeposition baths. Depending on the nature of the additives they can affect the electrodeposition process either by forming complexes with the metal ions or by adsorption on the electrode surface. The influence of a variety of additives on the electrodeposition of metals in ionic liquids is a new area of interest and much more attention should be paid. The effect of additives on the electrodeposition of cobalt [61], nickel [62], silver [63] and lithium [64] from ionic liquids and of tin [65] and zinc [66, 67] from deep eutectic solvents was reported.

Zinc is a relatively cheap and abundant material and can be used as anode material in batteries. Rechargeable zinc-air batteries are considered as promising candidates as energy storage devices due to their relatively high energy density of up to ~500 Wh/kg. The most severe obstacle against the development of electrically rechargeable zinc based batteries is the formation of dendritic structures during charging, which is followed by poor cycling properties or even short cut. Considerable attention has been devoted to develop effective additives in aqueous electrodeposition baths for controlling the various qualities of electroplated Zn coatings [68-75]. The additives play a prominent role in producing bright and leveled deposits with an improved quality. However, still little is known about additives in ionic liquid electrolytes and the additives may play a different role in ionic liquids compared with aqueous systems. There are only two studies on the electrodeposition of zinc from deep eutectic solvents in the presence of additives. Abbott *et al.* [66] reported that the additives ethylene diamine and ammonia affected the zinc nucleation mechanism and the deposit morphology by altering the double layer structure. Pereira *et al.* [67] reported the effect of the tartrate ion on the electrodeposition of zinc from a choline chloride-ethylene glycol deep eutectic solvent. In their studies, it was shown that the grain size and morphology of the deposits, and the electrochemical behavior could be altered by addition of suitable additives to the IL based plating baths.

1.5 Ionic liquids as electrolyte for batteries

1.5.1 Rechargeable lithium-ion battery

Lithium-ion batteries are nowadays widely used in consumer electronics, such as cellphone, laptops and cameras. In 1991, Sony released the first commercial lithium-ion battery using lithium cobalt oxide ($LiCoO_2$) as the positive electrode and graphite as the negative electrode (Fig. 1.5.1).

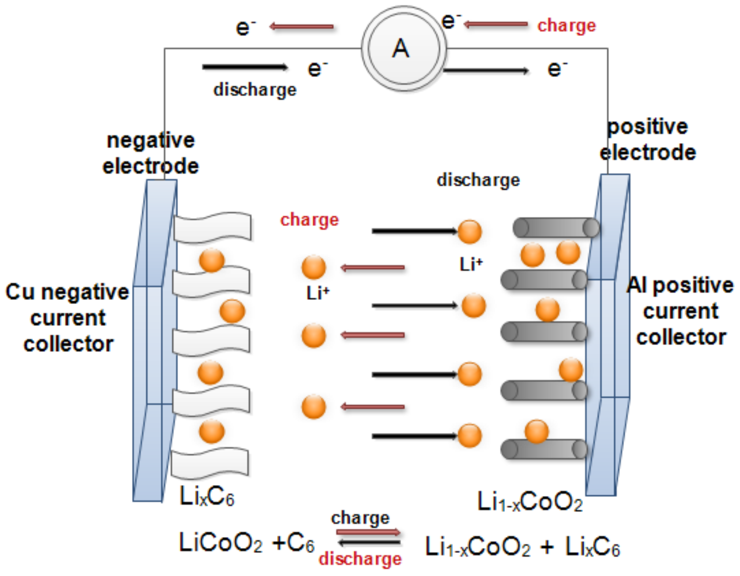

Fig. 1.5.1 *Rechargeable lithium-ion battery using lithium cobalt oxide ($LiCoO_2$) as the positive electrode and graphite as negative electrode. (Source: Nova Battery Systems)*

In 1996, Goodenough *et al.* proposed lithium iron phosphate ($LiFePO_4$) and other phosphor-olivines as positive electrode materials to improve the capacity and performance [76]. Recently, a silicon composites anode is used in batteries and they have a 20% higher capacity than previously available batteries [77]. The electrolytes used in these batteries are based on organic solvent, such as ethylene carbonate, dimethyl carbonate and diethyl carbonate. One concern about batteries is the safety as they have a potentially hazardous flammable electrolyte. The application of ionic liquids as electrolytes in batteries is a relatively new area of study that is steadily gaining attraction in the electrochemical and engineering communities. Ionic liquid electrolytes are relatively safe, since they can be nonvolatile and nonflammable. Furthermore, the thickness of the battery can be apparently reduced by employing ionic liquids as electrolytes as indicated in Fig. 1.5.2 [78-81].

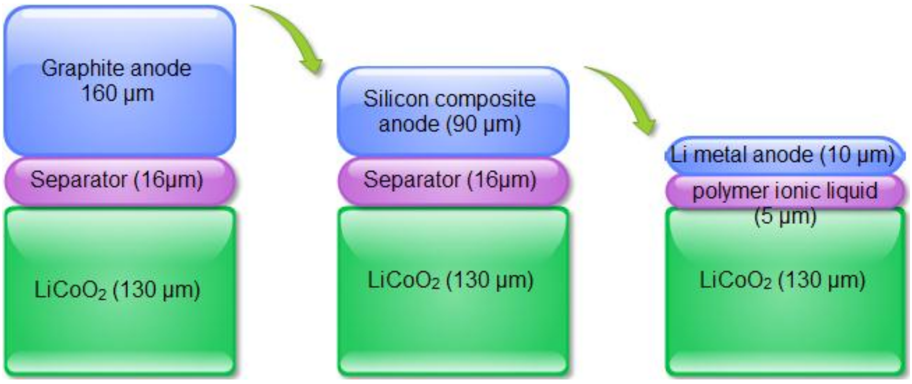

Fig. 1.5.2 *Thickness of the rechargeable lithium-ion battery by using different anode materials and electrolytes. (Source: Solid Energy)*

1.5.2 Rechargeable zinc-air battery

1.5.2.1 Ionic liquid electrolytes

Zinc-air batteries, for example, can have an energy density of ~0.5 kWh kg^{-1} which is three times more than the one of current lithium polymer batteries. Rechargeable zinc based batteries are important for electrochemical energy storage, as zinc is a cheap and well available material.

Zinc-air batteries use oxygen from the atmosphere as cathode reactant. Metallic zinc is oxidized on the anode. Zinc-air batteries have a higher energy density than other types, due to the fact that the cathodic reactant is not packaged in.

The chemical equations for an alkaline zinc-air battery are:

$$\text{Anode: } Zn + 4OH^- \rightarrow Zn(OH)_4^{2-} + 2e^-$$

$$Zn(OH)_4^{2-} \rightarrow ZnO + H_2O + 2OH^-$$

$$\text{Cathode: } 1/2\ O_2 + H_2O + 2e^- \rightarrow 2OH^-$$

$$\text{Overall: } 2Zn + O_2 \rightarrow 2ZnO$$

As zinc-air batteries are open to the atmosphere, one disadvantage is the evaporation of water from the aqueous alkaline electrolytes and the absorption of CO_2 from the atmosphere. That is the main reason why much attention has been focused on using ionic liquids as electrolytes in rechargeable zinc-air batteries. In a recent perspective paper, it is demonstrated that ionic liquid electrolytes can support redox processes of metals at the anode and the oxygen reduction and evolution processes at the cathode [82].

1.5.2.2 Ionic liquid polymer gel electrolytes

Polymer electrolytes could offer some distinct advantages over liquid electrolytes, such as improved safety, reduced leakage, simplified assembling process, and flexible design [83]. Polymer gel electrolytes containing Zn^{2+} ions with improved ionic conductivity based on poly(vinylidenefluoride) (PVdF), poly(acrylonitrile) (PAN), and poly(ethylene glycol)diacrylate (PEGDMA), dissolved in suitable organic solvents such as propylene carbonate (PC), ethylene carbonate (EC), and dimethylsulfoxide (DMSO) have been reported [84-87]. However, these organic solvents are unsuitable for open systems such as zinc-air batteries, as they are volatile and flammable.

Ionic liquids can be used in polymer electrolytes as substitutes for volatile organic solvents. Furthermore, polymers containing charged species have often a high ionic conductivity and can be expected to serve as electrolytes in zinc-based or lithium-ion batteries. It was reported that ionic liquid polymer gel electrolytes show excellent thermal stability, wide electrochemical windows, high mechanical stability, and high ionic conductivity at room temperature [88-91]. The polymer network provides mechanical integrity to such systems, while the incorporated IL in the polymer matrix improves the ionic conductivity. A conductivity in the range of 10^{-4}–10^{-3} S cm^{-1} was achieved, as reported in literature [50, 92, 93].

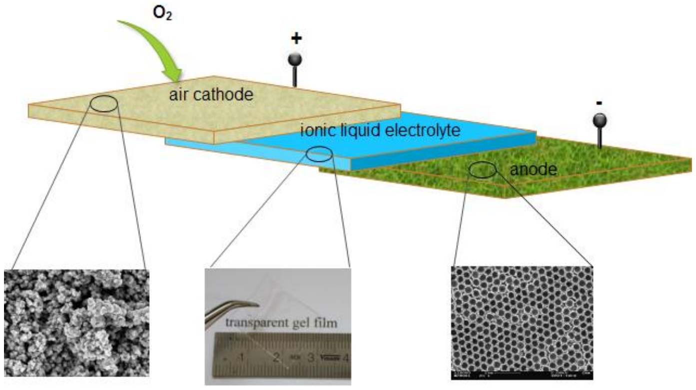

Fig. 1.5.3 *Ionic liquids polymer gel electrolytes for rechargeable zinc-air battery.*

The types of cations and anions in the ILs, the kind of the polymer, and the amounts of IL in the polymer must affect the conductivity and mechanical properties of such polymer electrolytes. Fig. 1.5.3 shows the schematic view of a zinc-air battery using an ionic liquid polymer gel as electrolyte.

1.5.2.3 Zinc-air battery technology

Rechargeable zinc-air batteries mainly consist of a zinc electrode, an electrolyte, a separator and an air electrode [94]. A zinc electrode with a porous structure or nanostructured zinc material such as zinc nanowires could provide a large surface area, thus largely improving discharge capacity. Furthermore, the morphology of the zinc electrode must maintain stable over thousand charge/discharge cycles. It has been shown in literature as was mentioned above that dendrite-free zinc can be obtained in ionic liquid electrolytes. Moreover, adding additives to the ionic liquid electrolytes can also improve the morphology of the zinc deposit.

The air electrode is mainly composed of a catalytic layer and a current collector. In bi-electrodes systems, as shown in Fig. 1.5.4, the air electrode has to perform both the oxygen reduction reaction (ORR) and the oxygen evolution reaction (OER) efficiently. The catalysts such as Co_3O_4 [95], $La_{0.6}Ca_{0.4}CoO_3$ [96] and $La_{0.6}Ca_{0.4}MnO_3$ [97] can be used for ORR and OER. Bi-electrodes are easy to prepare and the structure is compact, however it has a limited cycle life as the ORR and OER are using the same electrode.

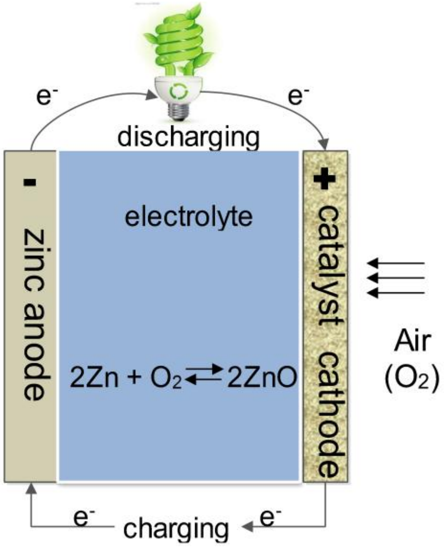

Fig. 1.5.4 *Rechargeable zinc-air battery based on bi-electrodes.(Source: International Zinc Association)*

For that reason, triple electrodes were used for rechargeable zinc-air batteries (Fig. 1.5.5), where charging uses a third electrode located on the other side of zinc electrode. Therefore, the batteries have a longer life and an improved cycle life. The catalysts such as Pt, MnO_2 have been investigated for ORR. These catalysts also show high catalytic activity in ionic liquid electrolytes [82].

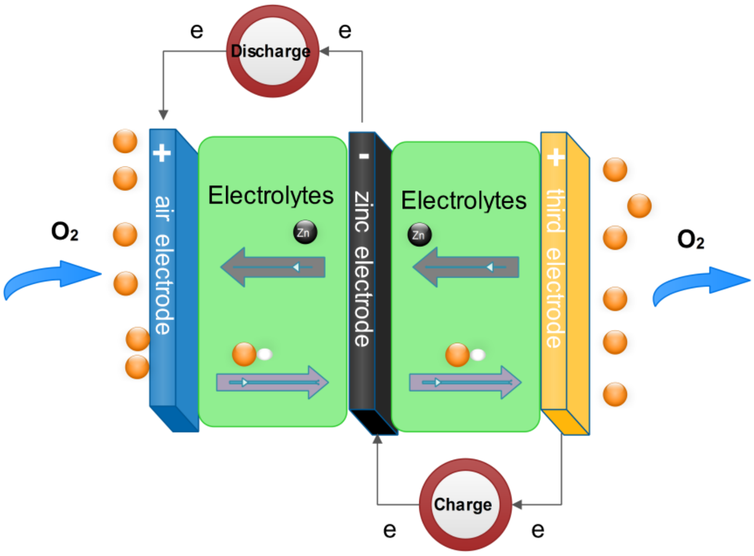

Fig. 1.5.5 *Schematic view of zinc-air battery based on tri-electrodes.*

Redox flow batteries have some advantages over solid state batteries. In redox flow batteries the electrolytes can be pumped into and out of a reservoir tank. After discharging, the electrolytes are pumped out of the cell and new electrolytes are pumped in for charging.

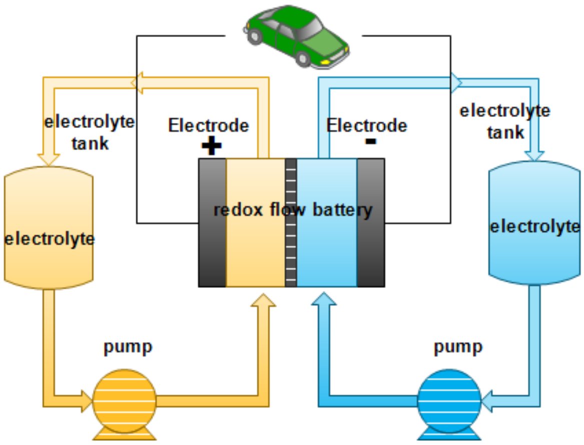

Fig. 1.5.6 *Schematic view of redox flow rechargeable zinc-air battery. (Source: Batteries and the Green Energy Revolution)*

The electrolytes can be easily regenerated outside of the cell. Such a system prevents zinc passivation and reduces dendrite formation. Depending on the volume of the tank, flow batteries can have a wide power range and higher capacity ratings. Fig. 1.5.6 depicts the schematic view of a redox flow battery system.

1.6 The scope of this thesis

The development of rechargeable zinc-air batteries is mainly limited by the dendritic zinc growth during charging and CO_2 absorption in aqueous KOH solutions. As a first step, the electrodeposition of zinc from ionic liquid electrolytes was investigated.

The goal of this work is to get a fundamental knowledge of zinc electrochemical performance in ionic liquid electrolytes. As displayed in Fig. 1.6.1, the interaction between the species and their interaction with the substrate are rather complex and each of the interactions can limit the deposition process. The interaction between cation and anion, ionic liquid mixtures with water and the solvation of zinc ions were studied by FTIR and Raman spectroscopy. The electrodeposition of zinc in pure ionic liquid, ionic liquid+water mixtures and ionic liquid/additive was studied by CV, SEM, XRD and *in-situ* STM. Furthermore, dendrite free zinc film, zinc nanowires and macroporous materials were prepared.

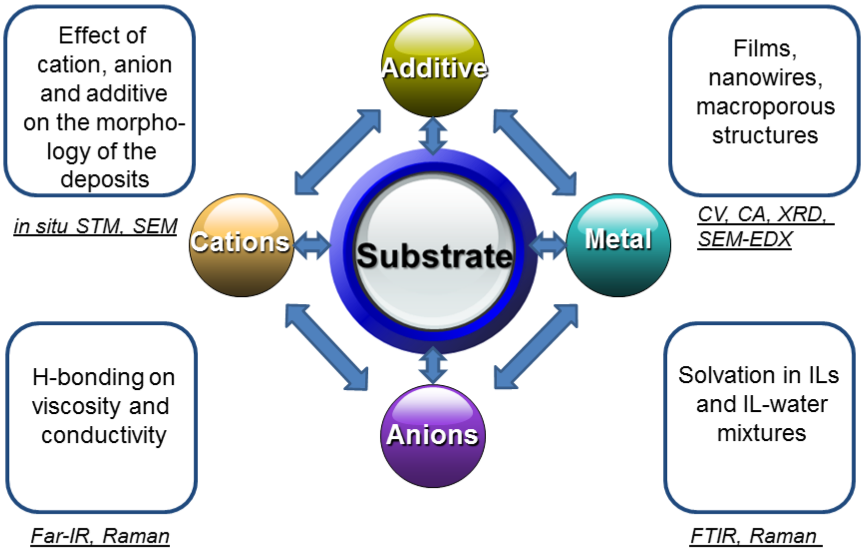

Fig. 1.6.1 *Scheme shows the interaction between the species and their interaction with substrate in the electrochemical system.*

2 Experimental

2.1 Chemicals

Zn(TfO)$_2$ powder (IO-LI-TEC, Germany, 99%) was used as a zinc source. The ionic liquids, 1-ethyl-3-methylimidazolium trifluoromethylsulfonate ([EMIm]TfO), 1-butyl-1-methylpyrrolidinium trifluoromethylsulfonate ([Py$_{1,4}$]TfO) and 1-ethyl-3-methylimidazolium dicyanamide ([EMIm]DCA), were also purchased from IO-LI-TEC, Germany (Fig. 2.1.1). The ionic liquids were dried under vacuum at 120 ℃ to water contents of below 3 ppm and stored in closed bottles in an argon filled glove box (OMNI-LAB from vacuum atmospheres) before use (prepared by Barbara Holly). The additive, 1,2-dimethyl-3-(trifluoromethyl)-1H-pyrazol-2-ium trifluoromethylsulfonate (98%) was obtained from SOLVAY FLUOR, Germany (Fig. 2.1.1).

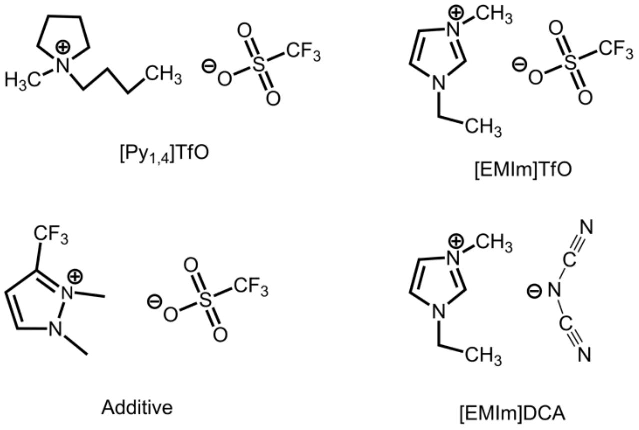

Fig. 2.1.1 *Chemical structure of the ionic liquids and the additive.*

2.2 Electrodeposition of zinc films

The electrochemical cell made of poly(tetrafluoroethylene) (Teflon) was clamped over a Teflon covered Viton O-ring, thus yielding a geometric surface area of 0.3 cm^2. A 25 mL glass beaker was employed as an electrochemical cell for the experiments at elevated temperature. The cell was kept closed by a Teflon cap during high temperature experiments in water containing ionic liquids to avoid the loss of water content via evaporation. Gold substrates (gold on glass from Arrandee Inc., Germany) were used as working electrodes. Prior to use the gold substrates were refluxed with isopropanol and heated in a hydrogen flame to red glow for a few minutes to remove possible contaminations. A platinum wire

(Alfa, UAS, 99,99%) was used as counter electrode. A zinc wire (Alfa, USA, 99,99%) or a platinum wire was used as reference and quasi reference electrode, respectively. The reference and counter electrodes were directly immersed in the solutions without using a separate compartment.

2.3 Polystyrene sphere templates for macroporous zinc

The polystyrene sphere template was prepared by dipping a gold substrate (200–300 nm thick gold films on chromium covered borosilicate glass, Arrandee, Germany) into the polystyrene suspension (10 vol% PS with a diameter of 600 nm dispersed in ethanol) for a few seconds at 40 ℃ and pulled out. After drying, the PS-covered substrate was heated at 100 ℃ for 2 h, which lead to a better cohesion of the spheres (prepared by Alexandra Prowald). The electrochemical cell made of Teflon was clamped over a Teflon covered Viton o-ring, thus yielding a geometric surface area of 0.3 cm^2. After deposition, the PS template was chemically removed by tetrahydrofuran. Subsequently, the samples were rinsed with isopropanol to ensure removal of the ionic liquid and then dried under vacuum (Fig. 2.3.1).

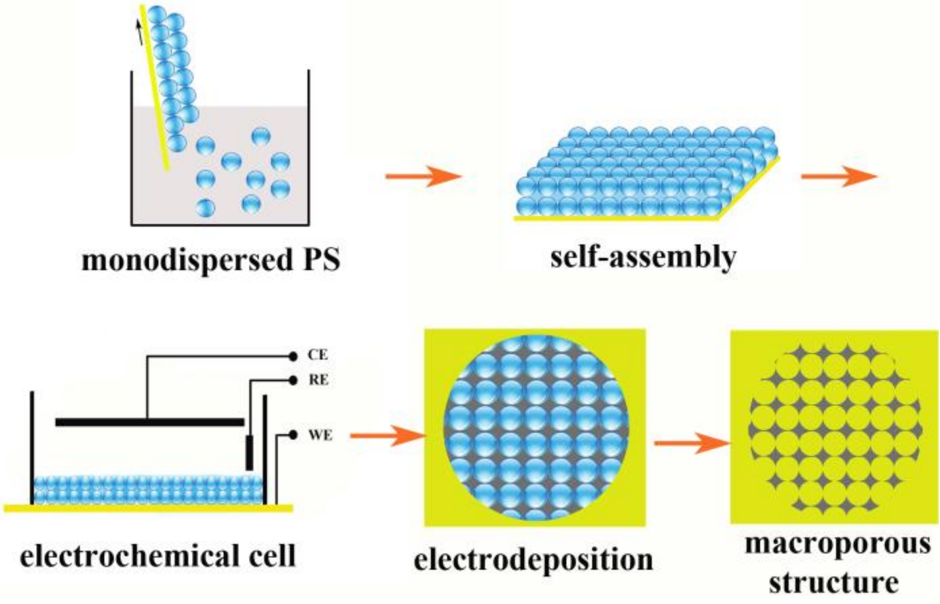

Fig. 2.3.1 *Schematic preparation of the polystyrene sphere template for zinc macroporous structure.*

2.4 Track-etched polycarbonate (PC) membrane template for zinc nanowires

Track-etched polycarbonate (PC) membranes with a nominal thickness of 21 µm, an average pore diameter of 90 nm and pore densities of 10^9 cm^{-2} (Ion Track Technology for Innovative Products, IT4IP, Belgium) were used as templates (Fig. 2.4.1). A thin layer of Au or of Cu (~100 nm thick) was sputtered on the reverse side of the templates serving as the working electrode. A platinum wire (Alfa, 99.99%) and a zinc wire (Alfa, 99.99%) were used as a counter and quasi reference electrode, respectively, for zinc deposition. The reference and counter electrodes were directly immersed in the solutions without using a separate compartment. A thick supporting zinc or copper layer is deposited on the sputtered side of the membranes. Copper wires were used both as counter and reference electrodes for copper deposition. A 10 mL glass beaker was employed as an electrochemical cell for the supporting layer deposition.

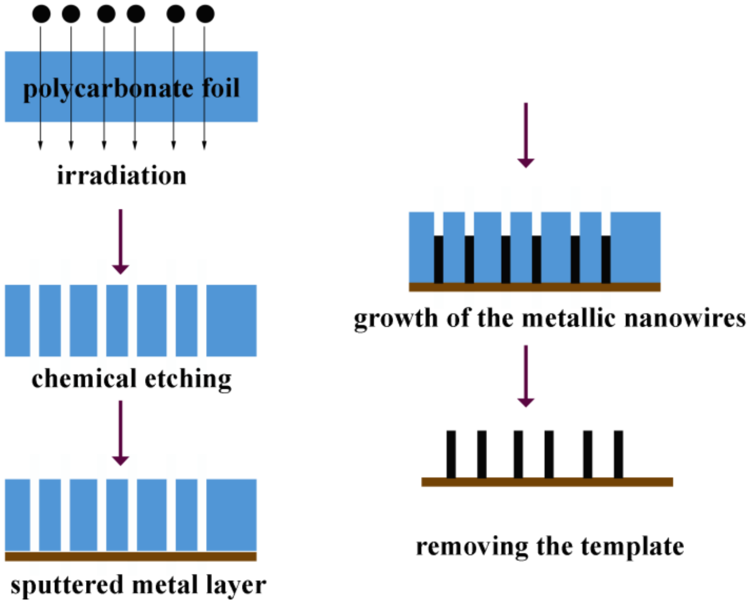

***Fig. 2.4.1** Track-etched polycarbonate (PC) membranes as template for zinc nanowires.*

2.5 Polymer gel electrolytes

Poly(vinylidenefluoride-hexafluoropropylene) (PVdF-HFP) was purchased from Sigma-Aldrich and used as received. The polymer gel electrolyte was prepared by mixing the polymer with the ionic liquid. The ionic liquid electrolyte was prepared by dissolving 0.2 M $Zn(TfO)_2$ in $[Py_{1,4}]TfO$. The polymer PVdF-HFP was dissolved in acetone with the polymer weight of 7.5 wt%. Subsequently, the ionic liquid electrolyte was mixed with the PVdF-HFP/acetone solution and stirred magnetically for 4-5 h. The weight ratio of the ionic liquid electrolyte to PVdF-HFP was at 7:3. Thereafter, the solution was poured into a small evaporation pan and dried at 60 ℃ for 4 h to allow acetone to evaporate. The resulting gel film was then dried in vacuum overnight to remove the acetone completely. Finally, a transparent polymer gel electrolyte film with a thickness of about 300–400 µm, as shown in Fig. 2.5.1 (b), was obtained and used in the following experiments. The ionic conductivity of the polymer gel electrolyte was determined by ac impedance spectroscopy in the frequency range from 500 kHz to 0.1 Hz with an amplitude of 10 mV. The conductivity cell was set up by sandwiching the polymer gel electrolyte membrane (1 cm × 1 cm) between two copper sheets. The real part of the impedance Z', at Z'' = 0, was used to calculate ionic conductivity of the ionic liquid polymer gel electrolyte according to $\sigma = h/AZ'$, where h and A are thickness and area of the electrolyte between the two electrodes, respectively. The experiment was performed in an inert gas glove box.

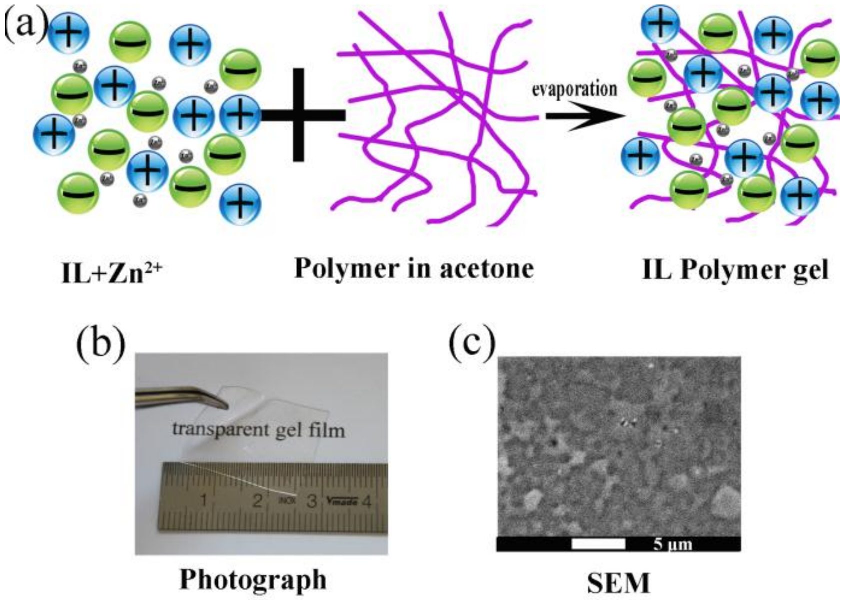

Fig. 2.5.1 ***(a)*** *Schematic preparation of IL polymer gel electrolyte,* ***(b)*** *photograph of gel polymer electrolyte and* ***(c)*** *SEM images of the gel polymer electrolyte.*

2.6 Characterization

The electrochemical measurements were carried out using a PARSTAT 2263 potentiostat/galvanostat controlled by PowerCV and PowerStep software. High resolution SEM with EDX (Carl Zeiss DSM 982 Gemini) was used to characterize the surface morphology and the composition of the deposited films (made by Silvia Löffelholz). X-ray diffraction patterns were recorded using a Siemens D-5000 diffractometer with Co Kα radiation or a Panalytical Empyrean diffractometer with Cu Kα radiation. Contact angle measurements were taken using a Krüss DSA100S system for sessile droplet analysis (Krüss GmbH, Hamburg, Germany). The contact angle is measured immediately after applying the droplet, in order to reduce the effect of moisture absorption or water evaporation. Each contact angle measurement was repeated at least three times.

The IR measurements were performed using a Bruker VERTEX 70 FTIR spectrometer (measured by Karin Bode). The instrument is equipped with an extension for measurements in the far infrared region. This equipment consists of a multilayer mylar beam splitter, a room temperature DLATGS detector with preamplifier and polyethylene (PE) windows for the internal optical path. The accessible spectral regime for this configuration is between 30 and 680 cm^{-1}.

The Raman measurements were carried out with a Raman module FRA 106 (Nd:YAG laser, 1064 nm) attached to a Bruker IFS 66v interferometer (measured by Karin Bode). The samples were sealed under an argon atmosphere in glass capillaries, and data were recorded at room temperature.

The STM experiments were performed with in-house designed STM heads and scanners under inert gas conditions with a Molecular Imaging PicoScan 2500 STM controller in feedback mode. The STM scanner and the electrochemical cell were assembled in the glove box; subsequently, the STM head was placed inside of an argon-filled stainless steel cylinder, thus ensuring inert gas conditions during the STM experiment. Then, the cylinder was transferred to the air conditioned laboratory with a constant temperature of 23 ± 1 °C and placed onto a vibration-damped table from IDE, Germany. To reduce thermal drift and hysteresis of the piezo to a minimum, the retracted STM scanner was kept scanning overnight. STM tips were prepared by electrochemical etching of 0.25 mm 90:10 % Pt/Ir wires in 4 M NaCN solution followed by coating with an electropaint from BASF (ZQ 84-3225 0201). During the STM experiments, the potential of the working electrode was controlled by the PicoStat from Molecular Imaging. In all experiments, the STM images were obtained by scanning from the bottom to the top with a scan rate of 2 Hz and a resolution of 512 pixels per line. The potential was held constant for each image and changed at the bottom of each new image in 0.1 V steps. Correspondingly, the tip bias was changed by 0.1 V steps to keep its electrode potential constant.

3 Results and discussion

3.1 Electrodeposition of zinc films from ionic liquids and ionic liquid+water mixtures

3.1.1 Electrodeposition from pure ionic liquids

The cyclic voltammograms of 0.2 M Zn(TfO)$_2$ in [EMIm]TfO and in [Py$_{1,4}$]TfO recorded on gold at different temperatures are presented in Figs. 3.1.1 and 3.1.2. The electrode potential was ramped down in both cases from the open circuit potential (OCP) to −2 V in the forward scan and then up to +2 V in the reverse scan with a scan rate of 10 mV/s. At room temperature, the cathodic wave observed at about −0.8 V (c1) in Fig. 3.1.1 is ascribed to the bulk reduction of Zn^{2+} to the metal. The cathodic wave at about −1.5 V (c2) corresponds to the reduction of the imidazolium cation. The electrodeposition of zinc at room temperature requires a considerable overpotential of about 700 mV to drive the nucleation process. With increasing temperature the overpotential is decreased and is less than 100 mV at 125 ℃. On the reverse scan, the deposited zinc is anodically stripped, indicated by two anodic peaks. The first peak (a1) is due to the stripping of Zn, whereas the second peak (a2), becoming more obvious at higher temperature, is associated with the dissolution of Zn-Au alloys. The formation of Zn-Au alloy was also confirmed by XRD studies.

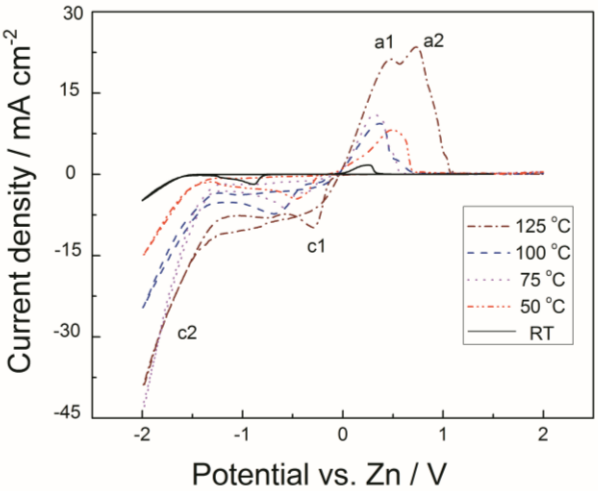

Fig. 3.1.1 *CVs of 0.2 M Zn(TfO)$_2$ in [EMIm]TfO on gold at different temperatures. Scan rate: 10 mV/s.*

As expected, the peak currents of both deposition and stripping significantly rise with increasing temperature. This is mainly the result of decreasing viscosity with increasing temperature. A comparison of Figs. 3.1.1 and 3.1.2 shows that the overall electrochemical behavior of both liquids is similar, but not identical. With [$Py_{1,4}$]TfO the currents are a bit lower and the nucleation of Zn requires higher overpotentials.

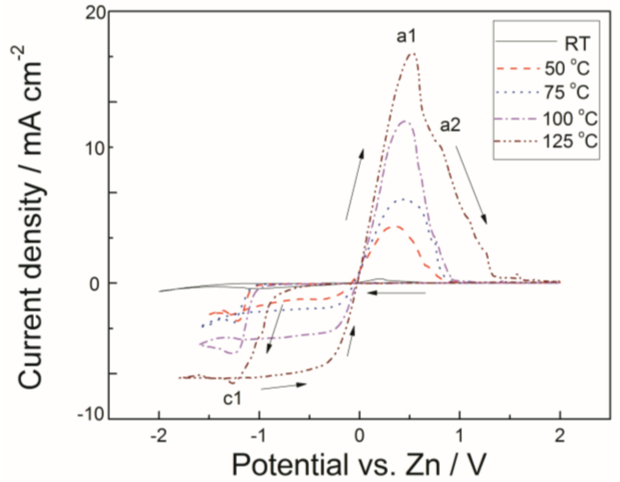

Fig. 3.1.2 *CVs of 0.2 M Zn(TfO)$_2$ in [$Py_{1,4}$]TfO on gold at different temperatures. Scan rate: 10 mV/s.*

The potentiostatic electrodeposition of zinc at different temperatures was performed on gold substrates at the corresponding cathodic peak potentials, as shown by the CVs, for 2 h in [EMIm]TfO and [$Py_{1,4}$]TfO containing 0.2 M Zn(TfO)$_2$. In each case the minimum potential to ensure Zn growth was applied. The overpotentials are thus not identical. It should be mentioned here, that nucleation studies by potentiostatic polarization experiments are not always reproducible in ionic liquids, as most likely nucleation is influenced by IL solvation layers which themselves might be influenced by nucleation. As this field of surface electrochemistry in ionic liquids is still at its infancy it is recommended to refrain from overinterpreting nucleation data. Subsequently, the deposits were washed thoroughly with isopropanol to remove the residual ionic liquids. The electrodeposited zinc layers were then characterized by SEM-EDX and XRD, respectively. A silvery uniform zinc deposit with a good adherence to the substrate was obtained from [EMIm]TfO. In contrast, a dark gray deposit with poor adherence to the substrate was obtained from [$Py_{1,4}$]TfO. An EDX analysis of the electrodeposited layers reveals in both cases that around 98% of the deposit was zinc together with oxidized zinc, a consequence of *ex situ* handling for the SEM experiments. Furthermore there might be some adsorbed ionic liquids.

The morphology of the Zn deposits obtained from [EMIm]TfO and from [$Py_{1,4}$]TfO at different temperatures is shown in Figs. 3.1.3 and 3.1.4, respectively. As shown in Fig. 3.1.3

(a), Zn electrodeposits obtained in [EMIm]TfO at room temperature appear to have a plate-like morphology, with the plates perpendicular to the substrate surface. The inset of Fig. 3.1.3 (a) gives hints that a layer-by-layer growth pattern structure seems to exist inside each grain where further nucleation seems to occur along an existing plate-shaped crystal. It is an open question to which extent such morphology might be caused by solvation layers adsorbed at the growing Zn surface. An influence of ionic liquid solvation layers on electrochemical processes is likely as discussed in [98]. Furthermore, it is likely that these solvation layers are dependent on temperature and I expect a reduced structure at elevated temperature. As shown in Fig. 3.1.3 (b)-(d) the zinc deposits obtained at higher temperatures contain coarse, hexagonally-shaped grains. The size of the zinc grains increases with increasing temperature.

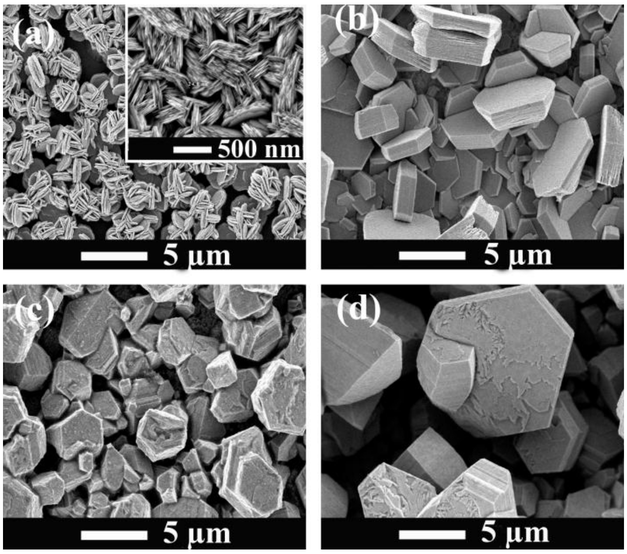

Fig. 3.1.3 *SEM images of zinc deposits made from 0.2 M Zn(TfO)$_2$ in [EMIm]TfO on gold at different temperatures: (a) room temperature at E = −0.82 V, (b) 50 ℃ at E = −0.46 V, (c) 75 ℃ at E = −0.57 V, (d) 100 ℃ at E = −0.68 V.*

In Fig. 3.1.4 (a)-(d) the morphology of Zn deposits obtained in [Py$_{1,4}$]TfO at room temperature and elevated temperatures is presented. The morphology is considerably different to the one obtained in [EMIm]TfO, furthermore, compared to Fig. 3.1.3, the size of the zinc grains in Fig. 3.1.4 is much smaller than in the case before, indicating a grain refining effect of [Py$_{1,4}$]$^+$. In [99] it was reported that the interaction of [Py$_{1,4}$]$^+$ with the Au(1 1 1) surface is stronger than the one of [EMIm]$^+$ with Au(1 1 1), which can lead to a difference in the microstructure of the obtained deposits. The stronger adsorption of [Py$_{1,4}$]$^+$ to the surface of the growing nuclei might lead to a nanocrystalline deposition. It should be repeated at this point that considerably strongly adsorbed solvation layers exist on electrode surfaces, and they depend on the applied electrode potential. However, it is currently totally unclear how these solvation layers are influenced by solutes. This field will be a future topic in the fundamental electrochemistry of ionic liquids. Quite recent results show that even tiny amount of LiCl disturb these layers [100].

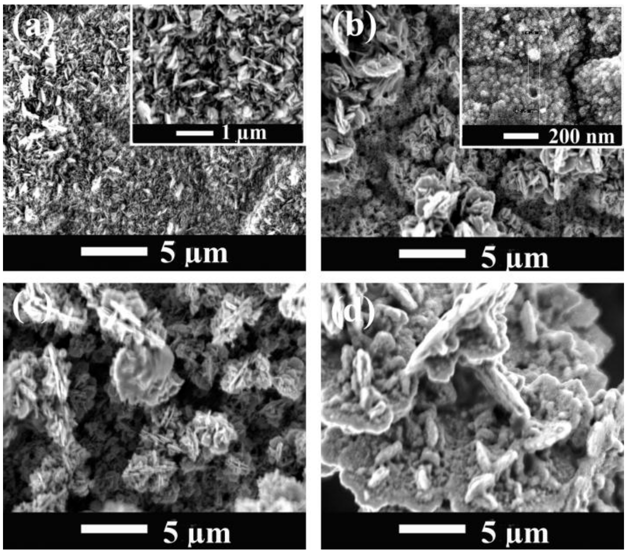

Fig. 3.1.4 *SEM images of zinc deposits made from 0.2 M $Zn(TfO)_2$ in $[Py_{1,4}]TfO$ on gold at different temperature: (a) room temperature at E = −1.0, (b) 50 ℃ at E = −1.21 V, (c) 75 ℃ at E = −1.27 V and (d) 100 ℃ at E = −1.272 V.*

The XRD patterns of zinc deposits obtained in [EMIm]TfO and in $[Py_{1,4}]TfO$ at room temperature and at 50 ℃ are shown in Fig. 3.1.5. The characteristic diffraction peaks of Zn (JCPDS File No. 04-0831) and of $AuZn_3$ (JCPDS File No.50-1336) have also been added in the pattern for comparison. All XRD pattern exhibit in common three pronounced diffraction peaks at 2 θ = 36.3°, 39.0° and 43.2°, which well agree with the (0 0 2), (1 0 0), and (1 0 1) diffractions peaks of hexagonal zinc. With increasing temperature a preferential growth of a particular facet can occur. For the deposit made at 50 ℃, in both cases a stronger orientation along the (1 0 1) plane was observed. It is also shown that the zinc coating is not a mono-phase and contains a mixture of zinc and a zinc gold alloy, namely $AuZn_3$, with several distinct diffraction peaks at 2 θ = 22.5°, 25.2°, 27.6°, 41.2°, 42.8°, and 45.9°, which agree well with the (2 0 0), (2 1 0), (2 1 1), (3 2 0), (3 2 1) and (0 0 4) diffractions of cubic $AuZn_3$. Similar results were also found by Borissov *et al.* [101]. These peaks become stronger at 50 ℃ for [EMIm]TfO while these peaks almost disappeared for $[Py_{1,4}]TfO$ at 50 ℃, compared to the deposit obtained at room temperature. There are also some tiny peaks at 2 θ = 31.8° and 34.4°, which might be correlated to hexagonal (0 0 2) and (1 0 0) ZnO facets. The peak found at 2 θ = 40.5 °(marked with asterisk in the Fig. 3.1.5) can be attributed to the (1 1 0) face of a AuZn alloy (JCPDS File No.65-5430). This peak at 2 θ = 40.5 °is much stronger for the deposit obtained from [Py$_{1,4}$]TfO. At a minimum these results reveal that a difference in the surface interaction of [Py$_{1,4}$]$^+$ and [EMIm]$^+$ with the Au(1 1 1) surface not only affects the morphology but also has a significant influence on the phase formation. It is surprising that the alloy formation is suppressed at elevated temperature, although all deposits were similarly thick. The average crystallite size of zinc was estimated according to Scherrer's equation [102]. The full-width at half maximum (FWHM) of the zinc XRD patterns made in [Py$_{1,4}$]TfO are wider than those from [EMIm]TfO. With increasing temperature the FWHM narrows, indicating a smaller crystal size of the electrodeposited zinc film at lower temperature. The average size of the deposit obtained from [Py$_{1,4}$]TfO was found to be ~16 nm at room temperature and ~48 nm at 50 ℃, and these results are consistent with the SEM result as shown in the inset of Fig. 3.1.4 (b). In all cases, the deposits obtained from [EMIm]TfO were microcrystalline. These results support again the assumption that pyrrolidinium ions rather lead to nanocrystalline deposits, whereas imidazolium ions rather lead to microcrystalline deposits.

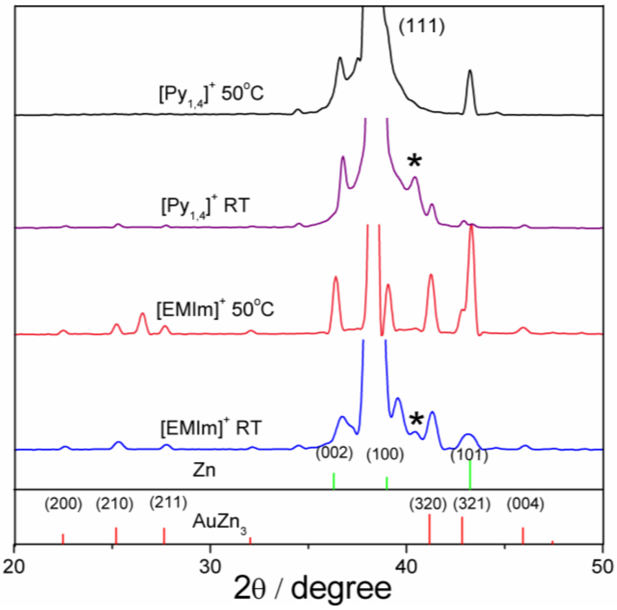

Fig. 3.1.5 *XRD patterns of zinc layers on gold deposited from [EMIm]TfO and [Py$_{1,4}$]TfO at room temperature and at 50 ℃, respectively.*

3.1.2 Electrodeposition from ionic liquid+water mixtures

The advantage of adding water to the ionic liquid is a decrease in viscosity and a subsequent increase in conductivity. Furthermore, zinc ions can be solvated by water to form $[Zn(H_2O)_6]^{2+}$ rather than being complexed with $[TfO]^-$ [103]. Compared to the $Zn(TfO)_2$ molecule, the smaller size of $[Zn(H_2O)_6]^{2+}$ ion facilitates diffusion. However, an increase in water content also results in a reduction in the electrochemical window of the ionic liquid. This is demonstrated in Figs. 3.1.6 and 3.1.7, where the electrochemical window is decreased when the water content in the ionic liquids is increased.

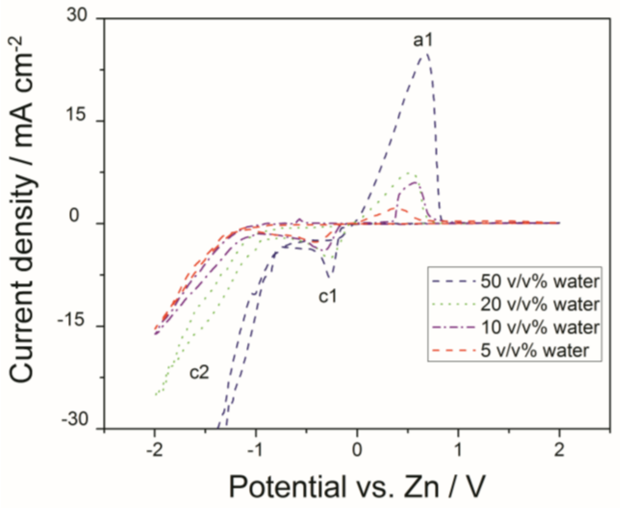

Fig. 3.1.6 *CVs of 0.2 M* $Zn(TfO)_2$ *in [EMIm]TfO on gold with different water contents. Scan rate: 10 mV/s, room temperature.*

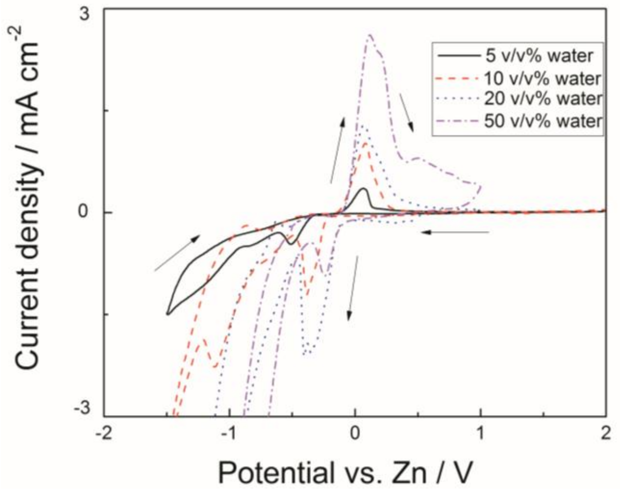

Fig. 3.1.7 *CVs of 0.2 M* $Zn(TfO)_2$ *in* $[Py_{1,4}]$*TfO on gold with different water contents. Scan rate: 10 mV/s, room temperature.*

Similar results were also observed by Compton *et al.* It was reported that the electrochemical window decreases in the following order: vacuum-dried > atmospheric > wet at 298 K > 318 K > 338 K [104]. Furthermore, the CVs shown in Figs. 3.1.6 and 3.1.7 reveal higher current densities for zinc deposition/dissolution with increasing water content. As in the case of the pure ionic liquids the CVs look similar, but the currents for [$Py_{1,4}$]TfO are almost ×10 lower than those of [EMIm]TfO. Obviously, water has a different effect on both liquids where only the cation is different.

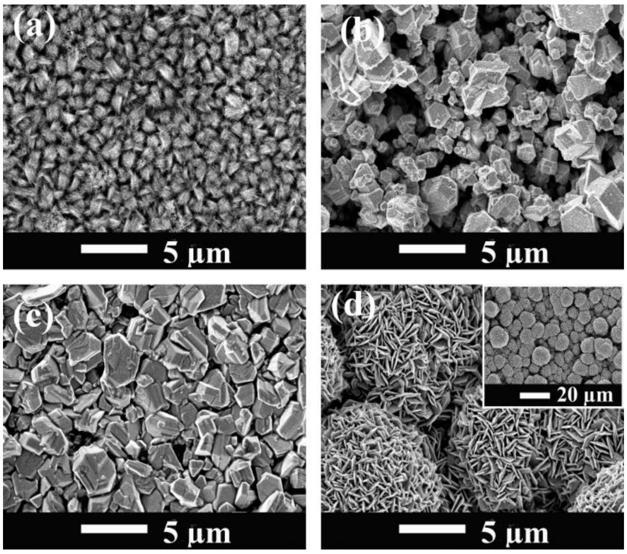

Fig. 3.1.8 *SEM images of zinc deposits made from 0.2 M $Zn(TfO)_2$ in [EMIm]TfO on gold with different water contents: (a) 5% (v/v) water at E = −0.42 V, (b) 10% (v/v) water at E = −0.33 V, (c) 20% (v/v) water at E = −0.27 V and (d) 50% (v/v) water at E = −0.26 V.*

The effect of water on the morphology of the Zn deposits was investigated and the results are shown in Figs. 3.1.8 and 3.1.9. The Zn deposit formed in [EMIm]TfO has a granular morphology with similar grain sizes. With increasing water concentration up to 50% (v/v) water, the morphology of the deposits is significantly altered (Fig. 3.1.8 (d)). A higher magnification shows that each grain comprises hundreds of small platelets. The addition of water decreases the solution viscosity and accordingly increases the mass transfer rate of the zinc(II) species as well as the growth rate of the electrodeposits. For the current density of Zn deposition/stripping 50% of water have the same effect as a temperature of 125 ℃ in the dry ionic liquid. A significantly different Zn morphology has been observed for zinc made in [$Py_{1,4}$]TfO. As shown in Fig. 3.1.9, a series of discrete thin platelets, perpendicular to the electrode surface, is obtained. The addition of water affects the morphology in terms of grain size and preferential grain orientation, as revealed by XRD results. The influence of temperature on the electrochemical behavior of mixtures of 0.2 M $Zn(TfO)_2$ in ionic liquids with 10% (v/v) water was also investigated.

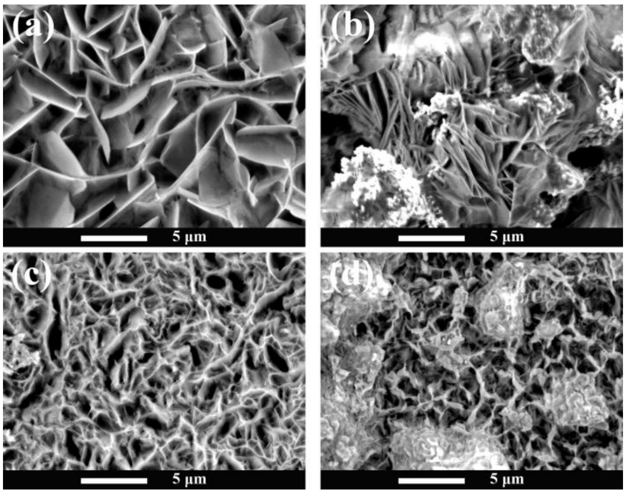

Fig. 3.1.9 *SEM images of zinc deposits obtained from 0.2 M* $Zn(TfO)_2$ *in* $[Py_{1,4}]TfO$ *on gold with different water contents: (a) 5% (v/v) water at E = −0.51 V, (b) 10% (v/v) water at E = −0.38 V, (c) 20% (v/v) water at E = −0.45 V and (d) 50% (v/v) water at E = −0.34 V.*

As will be shown below this water content leads to a minimum contact angle, lower even than the one of the pure ionic liquid. Therefore it was decided to do temperature dependent deposition experiments with this water content. The respective CVs are shown in Figs. 3.1.10 and 3.1.11.

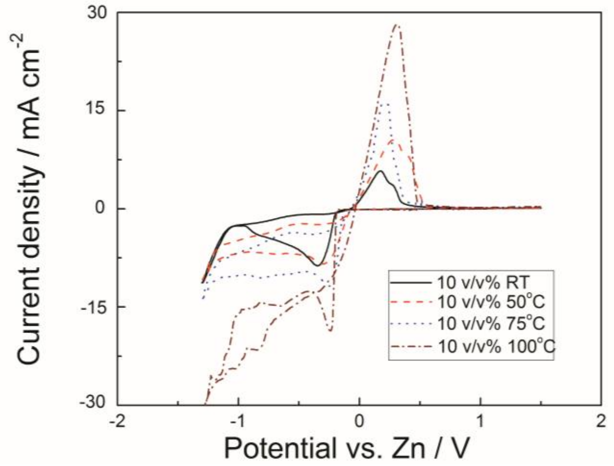

Fig. 3.1.10 *CVs of 0.2 M* $Zn(TfO)_2$ *in [EMIm]TfO with 10% (v/v) water on gold at different temperatures. Scan rate: 10 mV/s.*

The electrochemical window of the mixtures is slightly decreased as the temperature is increased. The voltammograms in both liquids look similar, but not identical. A detailed analysis of the CVs was not within the scope of the paper. The minimum information is that the nucleation must be different and that the currents in $[Py_{1,4}]TfO$+10% H_2O are at 100 ℃

only 2/3 of the ones in [EMIm]TfO+10% H_2O. The surface morphologies of the zinc deposits produced from mixtures of 0.2 M $Zn(TfO)_2$/ionic liquids with 10% (v/v) water at different temperatures are shown in Figs. 3.1.12 and 3.1.13. The zinc grains obtained at higher temperatures are larger than those ones obtained at lower temperatures. This change in morphology could be due to differences in mass transport, IL+water structure, speciation, hydrogen evolution or double layer structure in the two liquids. At higher temperatures, the deposits became less uniform in the case of $[Py_{1,4}]TfO$ (Fig. 3.1.13 (d)). This can be ascribed to the increased nucleation rate and growth at high temperatures.

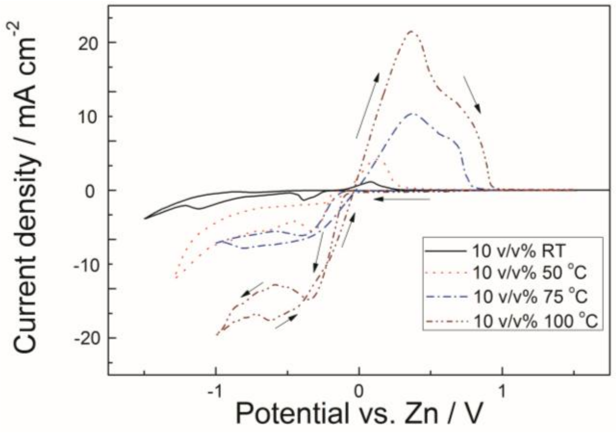

Fig. 3.1.11 *CVs of 0.2 M $Zn(TfO)_2$ in $[Py_{1,4}]TfO$ with 10% (v/v) water on gold at different temperatures. Scan rate: 10 mV/s.*

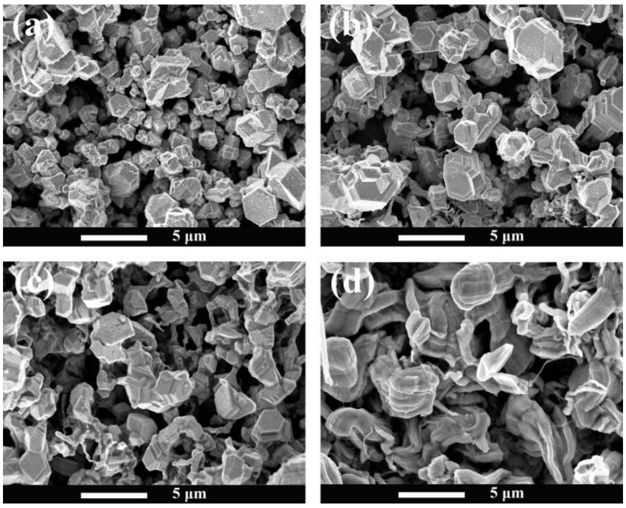

Fig. 3.1.12 *SEM images of zinc deposits obtained from 0.2 M $Zn(TfO)_2$ in [EMIm]TfO with 10% (v/v) water on gold at different temperatures, (a) room temperature at $E = -0.35$ V, (b) 50 ℃ at $E = -0.3$ V, (c) 75 ℃ at $E = -0.25$ V and (d) 100 ℃ at $E = -0.24$ V.*

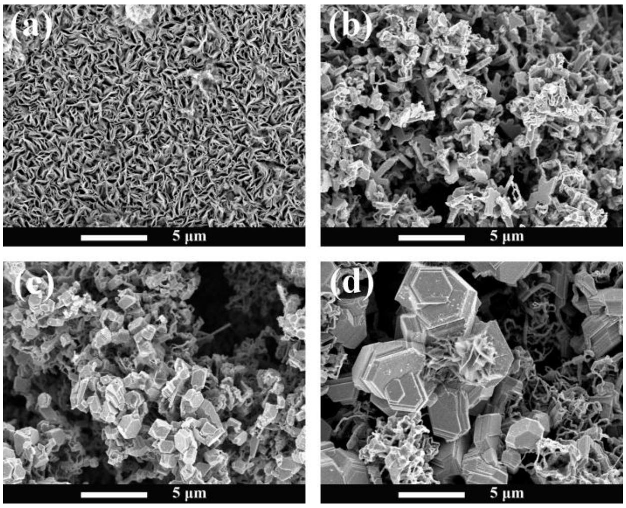

Fig. 3.1.13 *SEM images of zinc deposits obtained from 0.2 M* $Zn(TfO)_2$ *in* $[Py_{1,4}]TfO$ *with 10% (v/v) water on gold at different temperature, (a) room temperature at E = −0.41 V, (b) 50 ℃ at E = −0.33 V, (c) 75 ℃ at E = −0.4 V and (d) 100 ℃ at E = −0.35 V.*

Unlike in pure ionic liquids, the XRD results indicate the formation of pure zinc without any hint for the formation of zinc-gold alloys (Fig. 3.1.14). Obviously water changes the interaction of the ions with the electrode surface. In order to get more insight into the interfacial processes contact angle measurements were performed.

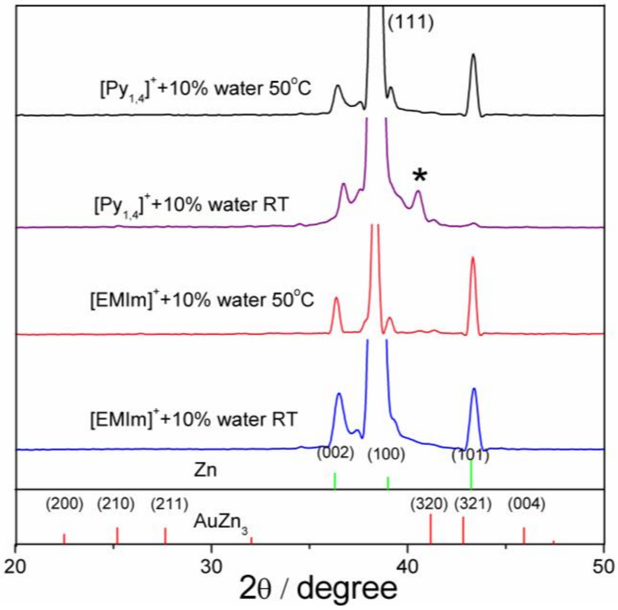

Fig. 3.1.14 *XRD patterns of zinc layers on gold deposited from [EMIm]TfO+10% (v/v) water and* $[Py_{1,4}]TfO$*+10% (v/v) water at room temperature and 50 ℃, respectively.*

The contact angle at the solid-liquid interface is of great importance as it can be used to determine the interfacial surface energy, the wettability and the electrochemical properties of the interfaces [105]. Therefore, contact angle experiments of 0.2 M Zn(TfO)$_2$ in both ionic liquids with varying water content on gold were performed and the results are shown in Figs. 3.1.15 and 3.1.16. Because of device limitations I had to restrict here to a maximum temperature of 50 ℃. The contact angles of pure ionic liquids and water on gold were also determined for comparison. The contact angles of [EMIm]TfO and of [Py$_{1,4}$]TfO on gold are about 30 ° and 36 °, respectively, at room temperature. In the presence of 0.2 M Zn(TfO)$_2$, the contact angles are slightly increased at room temperature. Surprisingly, the addition of water, even up to 50 v/v %, does not significantly change the contact angle of the ionic liquids+water mixtures. This is a bit surprising as water has a contact angle of 69 ° at room temperature, which is much larger than in the case of the ionic liquids. Though, the contact angle does not considerably increase with increasing water concentration. The results show a more subdued change of the contact angle with increasing of water content. The contact angles are decreased in both ionic liquids and in the mixtures of ionic liquid+water containing 0.2 M Zn(TfO)$_2$ with increasing temperature, indicating a better wettability of the surface at higher temperature. An increase in temperature could decrease interactions between cations and anions of ionic liquids, and between these and water. At this point an open question has to be left and the influence of water on ionic liquid electrochemistry might deserve more attention.

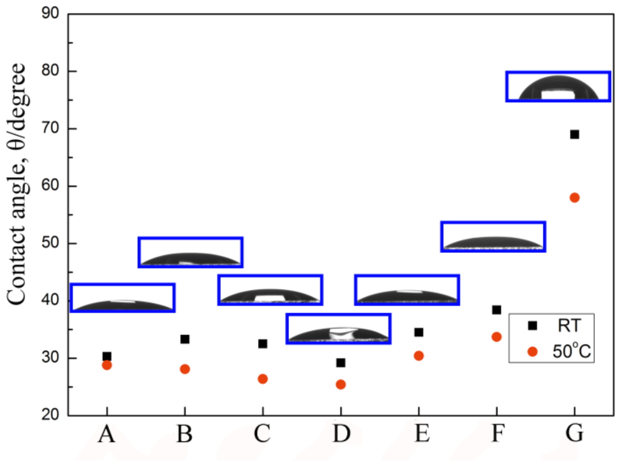

Fig. 3.1.15 Contact angles of [EMIm]TfO (A), 0.2 M Zn(TfO)$_2$ in [EMIm]TfO (B) together with different percent of water (5% (v/v) (C), 10% (v/v) (D), 20% (v/v) (E), 50% (v/v) (F)) and water (G) on gold at room temperature (inset pictures) and at 50 ℃.

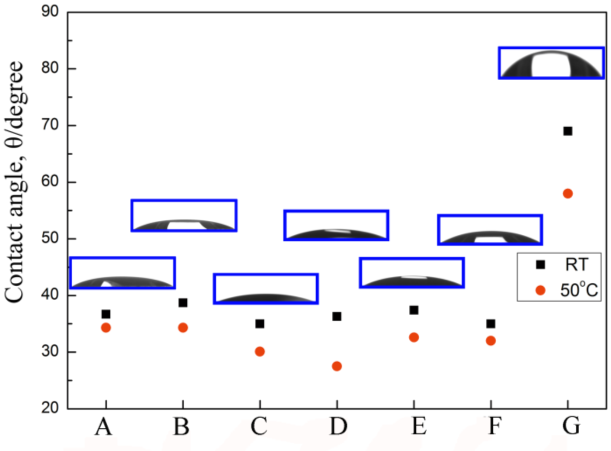

Fig. 3.1.16 *Contact angles of [Py$_{1,4}$]TfO (A), 0.2 M Zn(TfO)$_2$ in [Py$_{1,4}$]TfO (B) together with different percent of water (5% (v/v) (C), 10% (v/v) (D), 20% (v/v) (E), 50% (v/v) (F)) and water (G) on gold at room temperature and at 50 ℃ (inset pictures).*

3.1.3. Conclusions

The results show that zinc films with different morphologies can be successfully deposited from air and water stable ionic liquids, namely 1-butyl-1-methylpyrrolidinium trifluoromethylsulfonate ([Py$_{1,4}$]TfO), and 1-ethyl-3-methylimidazolium trifluoromethylsulfonate ([EMIm]TfO), as well as from mixtures of these ionic liquids with water. The cyclic voltammograms measured on gold exhibit a typical redox couple associated with deposition/stripping of zinc in the employed electrolyte. A silvery zinc deposit with good adherence was obtained from [EMIm]TfO, while dark gray zinc deposits with poor adherence were obtained from [Py$_{1,4}$]TfO. Both temperature and water have a significant effect on the morphology of the deposits and on the electrochemical window of both ionic liquids. In the presence of water pure Zn was formed, whereas, in the pure ionic liquids, both Zn and Zn-Au alloys were observed. Furthermore, the temperature significantly influences the deposits in terms of grain size and preferred grain orientation, and pyrrolidinium ions rather lead to nanocrystalline deposits in the water free liquids.

3.2 Template-assisted electrodeposition of highly ordered macroporous zinc structures from an ionic liquid

3.2.1 Cyclic voltammogram

The PS spheres have been self-assembled into three dimensional close-packed arrays on the gold surface. The structure is well ordered all over the surface without significant disordered regions as shown in a previous work [106]. Fig. 3.2.1 a) shows the cyclic voltammogram of 0.2 M $Zn(TfO)_2/[Py_{1,4}]TfO$ on a PS sphere-covered gold surface at a scan rate of 10 mV s^{-1} at room temperature. The potential was scanned in the negative direction from the open circuit potential to −1.5 V (vs. Zn) then back to +1.0 V in the reverse scan. The recorded redox process is associated with Zn deposition/stripping. A current loop was observed when the scan was reversed indicating a nucleation process.

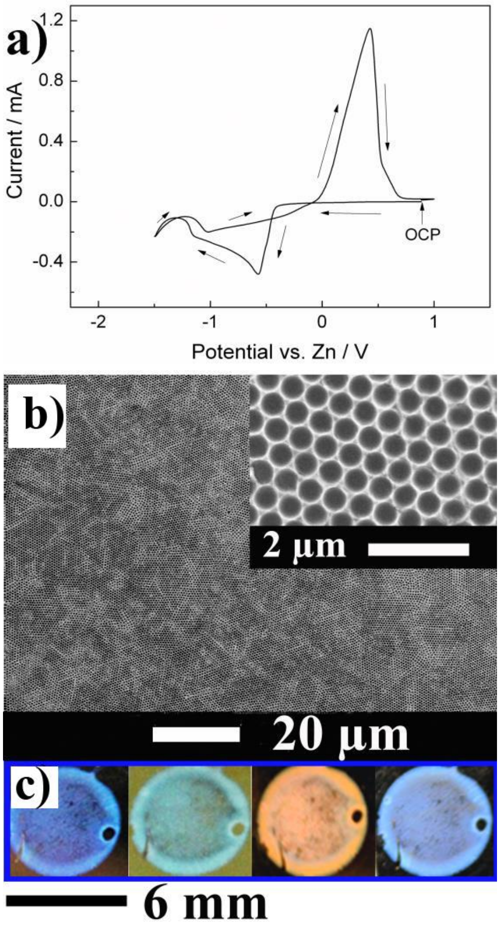

Fig. 3.2.1 a) *Cyclic voltammogram of 0.2 M $Zn(TfO)_2/[Py_{1,4}]TfO$ recorded on a PS-covered gold surface at a scan rate of 10 mV s^{-1} at room temperature.* ***b)*** *SEM images of two-dimensional macroporous zinc films.* ***c)*** *Photographs of the macroporous zinc films illuminated with white light.*

3.2.2 Potentiostatic electrodeposition

Potentiostatic electrodeposition was carried out to prepare the macroporous zinc structure. The PS template became almost transparent after immersion in the employed ionic liquid electrolyte for about 20 min, indicating a complete infiltration into the voids of the PS spheres. When the potentiostat is switched on, the nucleation takes place instantaneously all over the surface, and within a few minutes, a uniform zinc film is formed. As mentioned in a previous paper, the deposition potential, the concentration, and the deposition time have a great effect on the homogeneity of the macroporous structure [106]. Therefore, the experimental parameters must be precisely controlled. It should be noted that the electrodeposition of highly ordered macroporous zinc films is a surprisingly difficult process. Alloying of zinc with gold makes it difficult to get an ordered macroporous structure especially at a low growth rate. A prolonged deposition time even up to 2 h at −400 mV did not produce a macroporous structure; only a thin zinc layer was found underneath the PS template. Similar difficulties were found in the fabrication of macroporous lithium on copper [107]. Therefore, one has to select appropriate deposition parameters in order to get a macroporous structure. A successful fabrication of macroporous zinc from 0.2 M $Zn(TfO)_2/[Py_{1,4}]TfO$ was found to occur at an electrode potential of −0.45 V vs. $Zn|\ Zn^{2+}$ for 400 s.

3.2.3 Macroporous zinc structure

The SEM micrographs of Fig. 3.2.1 b) show a two-dimensional macroporous zinc structure with interconnected pores. A higher-magnification SEM image (inset of Fig. 3.2.1 b)) reveals a well-ordered macroporous zinc structure with a uniform periodicity. The macroporous Zn film shows also some disordered areas, which might be the result of the defects in the PS template or due to a not fully avoidable inhomogeneous current density. The obtained inverse opal zinc films exhibit–qualitatively–diffractive colors when illuminated with white light. It appears blue, green, and orange, respectively, by varying the angle of the incident light (Fig. 3.2.1 c)). If oxidized without damage to ZnO, such substrates are potentially interesting for dye-sensitized solar cells in which the photonic crystal might trap light and thus increase the efficiency of a solar cell.

A prolonged electrodeposition time at the same potential (−0.45 V) or even at different applied potentials does not–unfortunately–lead to a three-dimensional macroporous structure. The PS spheres can be pushed away, or the deposit even grows randomly above the PS sphere template. Therefore, galvanostatic electrodeposition was applied for the fabrication of three-dimensional macroporous zinc films which indeed lead to a homogenous deposit. Fig. 3.2.2

shows SEM micrographs of well-ordered three-dimensional Zn films obtained galvanostatically at a current density of 265 µA/cm^2 for 300 s. As seen, an ordered multilayered macroporous structure was obtained, indicated by several layers seen in the SEM of Fig. 3.2.2 b).

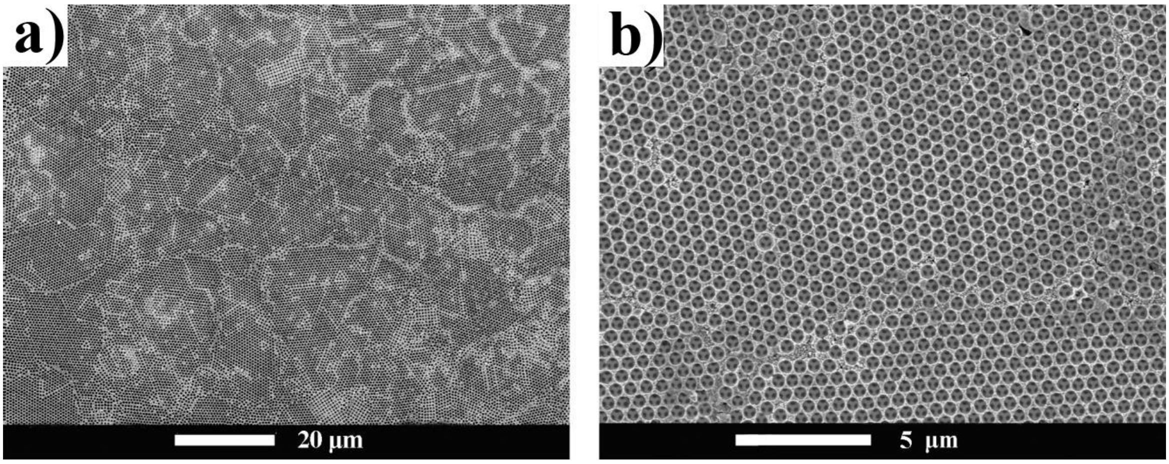

***Fig. 3.2.2** SEM images of a three-dimensional macroporous zinc structure at low **a)** and high magnification **b)** obtained from 0.2 M $Zn(TfO)_2/[Py_{1,4}]TfO$.*

The wettability of the ionic liquid on the PS template allows a sufficient infiltrating process and, consequently, the electrochemical formation of ordered structures. A good wettability eliminates the need for a hydrophilic modification of the PS surfaces as it is mandatory for aqueous solutions [108]. Furthermore, it is easier and faster to obtain macroporous structures in ionic liquid electrolytes than in aqueous solutions. It was reported by López *et al.* [109] that the deposition time was varied between 2 and 48 h in aqueous solutions for the preparation of macroporous zinc films, while in ionic liquid electrolytes, it takes only several minutes. The wettability of the pure ionic liquid $[Py_{1,4}]TfO$, of 0.2 M $Zn(TfO)_2/[Py_{1,4}]TfO$ and of water on gold and on PS-covered gold was investigated by measuring the contact angle of a droplet on the surface. Representative photographs of the contact angles are shown in Fig. 3.2.3. The contact angle, θ, of a water droplet on gold and on the PS-covered gold surface was found to change significantly (Fig. 3.2.3 C, F). The contact angle of water on gold ($\theta = 66°$, wetting) changes to $\theta = 110°$ on PS-covered gold, which means weak wetting. Both the pure ionic liquid and the $Zn(TfO)_2$ containing ionic liquid better wet the PS-covered electrode than the gold surface alone. The obvious difference in the contact angles between water and the ionic liquids suggests that the infiltration of the aqueous electrolytes into the voids of the template is very difficult, which might lead to an inhomogeneous growth of the macroporous films and to a need of more time and energy to drive the nucleation process. In contrast, ionic liquids easily infiltrate the interstitial channels of the PS spheres substrate.

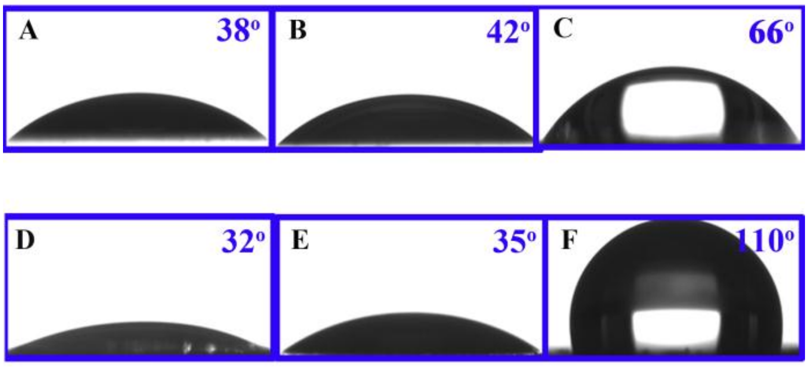

Fig. 3.2.3 *Contact angles of the ionic liquid [Py$_{1,4}$]TfO* ***A****, 0.2 M Zn(TfO)$_2$/[Py$_{1,4}$]TfO* ***B****, and water* ***C*** *on gold and of the ionic liquid [Py$_{1,4}$]TfO* ***D****, 0.2 M Zn(TfO)$_2$/[Py$_{1,4}$]TfO* ***E****, and water* ***F*** *on PS sphere covered gold.*

3.2.4 Conclusions

The electrochemical fabrication of zinc films with a two- and three-dimensional macroporous structure from the ionic liquid [Py$_{1,4}$]TfO using polystyrene templates, respectively, was reported. The structure was prepared by electrodeposition of zinc into the interstitial voids of PS templates formed on gold. The employed ionic liquid well wets the PS-covered gold surface. Highly ordered two- and three dimensional macroporous zinc films were reproducibly obtained. The fabricated films show light diffraction when illuminated by white light. The obtained ordered macroporous films would have a potential as anodes in batteries, but potentially also for dye-sensitized solar cells.

3.3 Electrochemical synthesis of vertically aligned zinc nanowires using track-etched polycarbonate membranes as templates

3.3.1 SEM micrograph of the track-etched PC membranes

Fig. 3.3.1 a) shows a top view SEM micrograph of the track-etched PC membranes. The membranes have rather a low porosity which is usually less than 15% and the pores are randomly distributed in the membranes. In our experiment, the membranes have a nominal pore diameter of 90 nm and a pore density of 10^9 cm^{-2}. Furthermore, Fig. 3.3.1 shows that double or triple pores are present, too. A contact angle measurement, as shown in the inset of Fig. 3.3.1 a), reveals that the ionic liquid well wets the membrane, which is quite important for the homogeneous growth of the nanowires inside of the membrane.

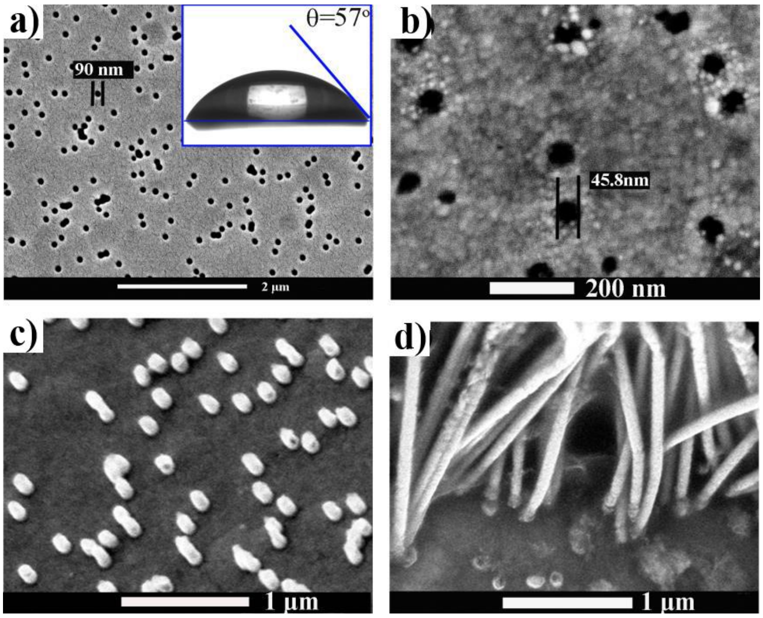

Fig. 3.3.1 *SEM images of* ***a)*** *the polycarbonate membrane and contact angle of 0.2 M* $Zn(TfO)_2$*–[EMIm]TfO solutions on the membrane (inset picture),* ***b)*** *the back side of the membrane after sputtering with gold,* ***c)*** *back side of the sputtered gold after removing the membrane and* ***d)*** *interface of the sputtered gold and zinc nanowire.*

Prior to deposition, a thin layer of Au or of Cu was sputtered on the reverse side of the templates to act as a supporting electrode. The thickness of the sputtered Au or Cu was roughly 100 nm and importantly the pores are not sealed by this process, only the diameter is decreased to 46 nm (Fig. 3.3.1 b) with sputtered Au). However, after dissolving of the membranes with dichloromethane, small Au islands or even wires can be found as shown in Fig. 3.3.1 c) (with sputtered Au). Similar results were also found with the sputtered copper surface. These results show that to some extent the Au or Cu particles from sputtering went inside the pore during the sputtering process and formed small islands or wires in the pore walls near the pore's surface. These small islands or even wires will serve as a special kind of nanoelectrodes for the growth of nanowires. The SEM image in Fig. 3.3.1 d) shows the interface between the gold substrate and the base of the nanowires. The nanowires shown in Fig 3.3.1 d) were obtained at a potential of −0.5 V versus a quasi Zn reference electrode for 2 h. The Zn nanowires will grow on these islands or wires, therefore the connection will depend on the interaction between the sputtered metal layer and the deposited metal itself. An alloy between the supporting metal and the deposited metal will improve the mechanical stability of the final electrode material. Once the template is removed, the nanowires should be free-standing. Zn well alloys with both gold and copper and it can be expected that the nanowires are free-standing as will be shown below.

3.3.2 Cyclic voltammograms

The cyclic voltammograms of 0.2 M $Zn(TfO)_2$ in [EMIm]TfO on a sputtered gold surface and inside of the PC membranes are presented in Fig. 3.3.2. In the latter case the sputtered side of the membrane was pressed on a gold electrode and deposition of Zn occurred through the membrane. The electrode potential was scanned from the open circuit potential (OCP) to −1 V, then up to +1 V in the reverse scan and finally back to the former OCP with a scan rate of 10 mV s^{-1}. Cathodic waves are observed at about −0.5 V (c1) in both cases, corresponding to the reduction of Zn^{2+} to Zn. The anodic peaks at about +0.4 V (a1) are ascribed to the stripping of Zn. In both cases, a current loop was found in the deposition regime indicating a nucleation process. The CVs show that the deposited zinc is electrochemically active and the wires exist in the form of the actual reactive metal with the IL probably protecting it from self-corrosion. The cyclic voltammograms recorded under the same conditions but on the sputtered copper surface and inside of the Cu sputtered PC membranes are shown in Fig. 3.3.3. The CVs show the typical zinc deposition (c1) and stripping peaks (a1) as well. Compared to Fig. 3.3.2, the potential for Zn deposition is more negative in both cases on copper than on gold under the same experimental conditions. Furthermore, a current loop in the deposition regime was only found on the sputtered copper layers indicating a nucleation process, while such a loop was not found for deposition inside of the membranes.

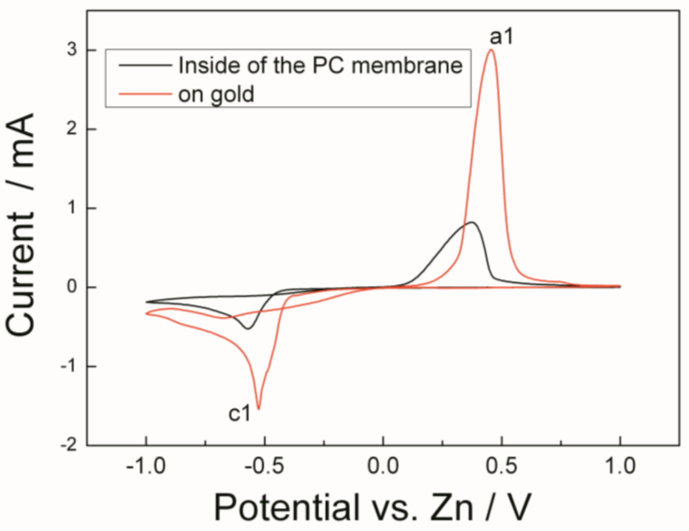

***Fig. 3.3.2** CVs of 0.2 M Zn(TfO)$_2$ in [EMIm]TfO on gold and inside of the PC membrane at room temperature. Scan rate: 10 mV s^{-1}.*

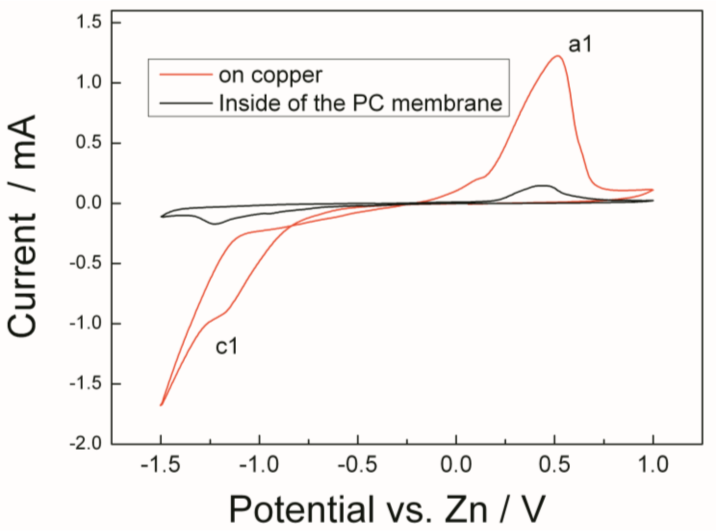

***Fig. 3.3.3** CVs of 0.2 M Zn(TfO)$_2$ in [EMIm]TfO on copper and inside of the PC membrane at room temperature. Scan rate: 10 mV s^{-1}.*

In both experiments the current on the sputtered side was almost 4 times higher than the one inside of the PC membranes. Such a ratio of currents is not in direct agreement with the one calculated from the porosity. Similar results were also reported for Co and Ni nanowires made in aqueous solutions [110]. In any case this result shows that the mass transport in the confined space of the nanochannels may have an effect on the growth of the nanowires.

3.3.3 The growth mechanism of nanowires

The growth mechanism of nanowires in aqueous solutions is known and was studied by several authors [111]. In the present study, chronoamperometry measurements were performed to investigate the growth mechanism of Zn nanowires inside of the membranes at a constant deposition potential of E = −0.5 V versus a Zn quasi reference electrode on the Au-sputtered membrane. The current vs. time curve depicted in Fig. 3.3.4 can be divided into three phases.

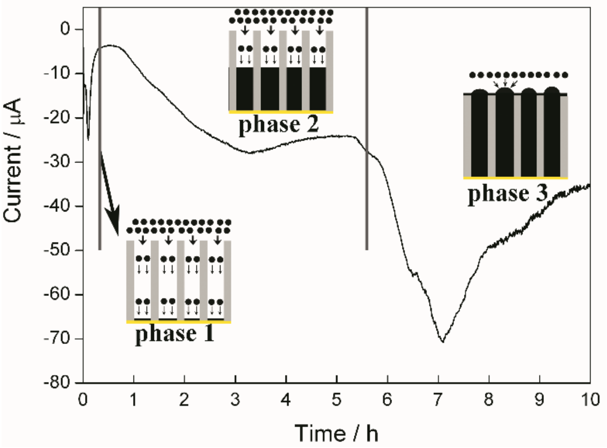

Fig. 3.3.4 *Cathodic current as a function of time for the potentiostatic deposition of Zn at a potential of –0.5 V versus Zn inside of the Au-sputtered polycarbonate membrane from 0.2 M* $Zn(TfO)_2$*/[EMIm]TfO.*

In phase 1, once the potential was applied, the nucleation occurs at the electrode-electrolyte interface forming a thin zinc layer at the bottom of the pores. The current increases first and decreases subsequently due to diffusion control. The diffusion processes are surely different from the conditions of a planar substrate due to the confined space inside of the templates. Subsequently, in phase 2, the current increases which is attributed to the proceeding growth in the pores towards the surface of the membranes. Growth proceeds until the pores are filled. Beyond this in phase 3, the deposit will now grow out of the templates by firstly forming hemispherical caps on top of the wires and then a more or less planar layer forms over the whole of the template surface. Correspondingly, the current increases first rapidly followed by a decrease due to the diffusion control. I refrain here from an overinterpretation of the chronoamperogram as also varying solvation layer effects might occur possibly influencing the deposition process. The potentiostatic current vs. time curve recorded on a Cu-sputtered template was similar to that of the Au-sputtered template (the results are not shown).

3.3.4 Supporting zinc or copper layer

Although the feasibility has been shown, the sputtered layer alone is not thick enough to allow an array of free standing nanowires. Once the template is removed in dichloromethane, the sputtered layer will break into pieces or enroll. Consequently, it is quite difficult to collect the nanowires. Therefore, a thick supporting layer is needed on the sputtered side to support the nanowires. For this purpose, firstly, a layer of Zn was deposited on the sputtered Au or Cu surface, while the other side of the membrane was insulated from the electrolyte using a Teflon tape. Top and cross-section views of such Zn deposits made on the Au or Cu surface are shown in Fig. 3.3.5.

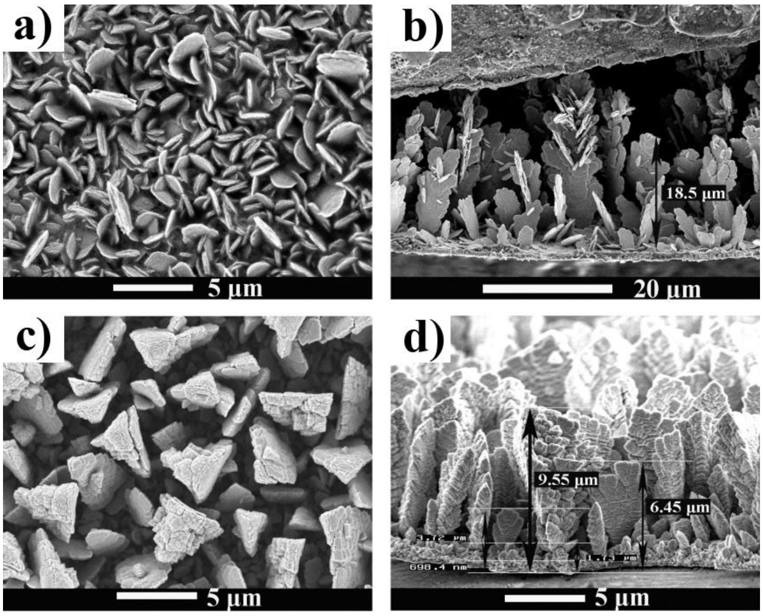

Fig. 3.3.5 *Top-view SEM images of Zn deposits formed in 0.2 M $Zn(TfO)_2$ in [EMIm]TfO at a potential of −0.5 V versus Zn for 2 h on sputtered gold* ***a)*** *and on sputtered copper* ***c)****. Cross-section of the samples is shown in* ***b)*** *and* ***d)*** *on gold and on copper, respectively.*

The Zn deposits obtained on the sputtered gold surface appear to have a platelike morphology, with the plate rather perpendicular to the surface. This growth is comparable to the one on a planar gold substrate. Furthermore, the particle size of the Zn deposit on copper is larger than the one on gold. The thickness of zinc on gold and on copper was 18.5 µm and 9.5 µm, respectively. In both cases a dendritic structure formed which does not make this layer suitable as a supporting layer, it is simply too brittle. Therefore, a thick layer of copper was deposited alternatively on both sputtered Au and Cu layers from 1 M CuCl/[EMIm]DCA solutions. The advantage of depositing a layer of copper is that it can be directly used as a current collector. As shown in Fig. 3.3.6, the thickness of the Cu layer can be more than 25 µm and the surface shows a dense structure. Thus, copper is quite a good candidate material as a supporting layer for zinc nanowires. It should be mentioned here that many factors can influence the morphology of the deposits such as concentration, current density, and temperature.

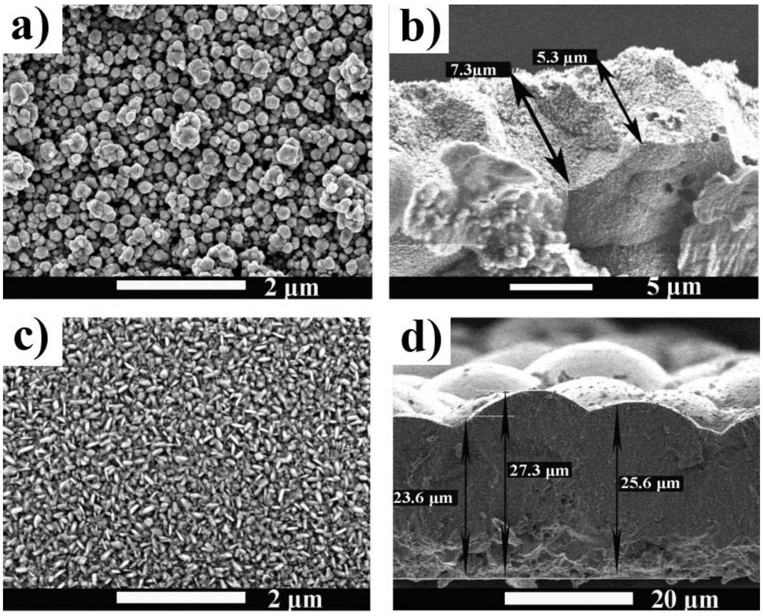

Fig. 3.3.6 *Top-view SEM images of Cu deposits formed in 1 M CuCl/[EMIm]DCA at a potential of −0.6 V versus Zn for 3 h on sputtered gold* ***a)*** *and on sputtered copper* ***c)****. Cross-section of the samples is shown on gold* ***b)*** *and on copper* ***d)****, respectively.*

3.3.5 Free standing nanowires

Zinc nanowire arrays are of interest for applications in nanoelectronic devices; furthermore, vertically aligned zinc nanowire arrays on a conductive substrate are expected to have a good performance in batteries due to their high surface area and their good electron conductivity [112]. However, until now published zinc nanowires are randomly oriented, whereas in the present paper free-standing zinc nanowire arrays are in the focus of my interest. SEM micrographs of Zn nanowires obtained potentiostatically at a potential of −0.5 V for 6 h (on Au-sputtered) and −1.0 V for 4 h (on Cu-sputtered), respectively, are shown in Fig. 3.3.7 and 3.3.8.

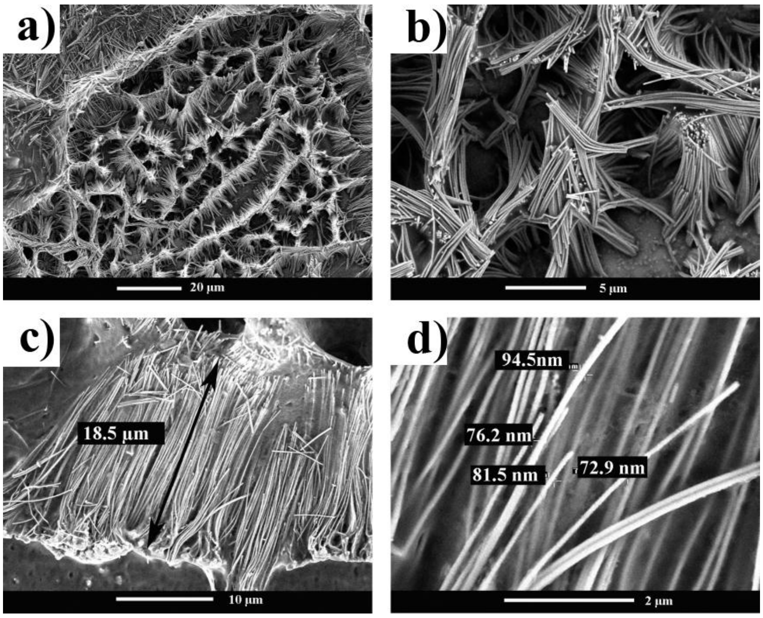

Fig. 3.3.7 a) *Top-view SEM image of Zn nanowires obtained after dissolution of the polycarbonate membrane from 0.2 M* $Zn(TfO)_2$*/[EMIm]TfO on sputtered gold with a copper supporting layer at a potential of −0.5 V versus Zn for 6 h.* ***b)*** *Top view of the Zn nanowires with higher magnification.* ***c)*** *SEM micrograph of the length of the nanowires and* ***d)*** *SEM micrograph of the diameter of the nanowires.*

In both cases Cu was electrochemically deposited on the sputtered membranes as a support structure of the nanowires. Fig. 3.3.7 a) and 3.3.8 a) show a top view of the vertically aligned Zn nanowire arrays. The zinc wires are practically free-standing and perpendicular to the substrate with a high aspect ratio. But, the Zn nanowire arrays are also bunched together as clearly seen from Fig. 3.3.7 b) and 3.3.8 b), and this effect increases with increasing length of the nanowires. Higher magnification SEM micrographs given in Fig. 3.3.7 c) and 3.3.8 c) show that the length of the nanowires is about 19 µm in both cases. The length of the wires, as can be seen from Fig. 3.3.7 a) in the corner and in Fig. 3.3.8 c), is not really uniform. One possible reason is that the pores in the commercial membranes are not aligned perfectly parallel but rather have a certain angular distribution. The SEM images in Fig. 3.3.7 d) and 3.3.8 d) show that the diameters of the zinc nanowires in the middle are almost equal to the ones of the templates. Only at or near the top end of the nanowires the diameter is a little smaller. The diameter is about 75 nm close to the top end and 94 nm in the middle as shown in Fig. 3.3.7 d), more or less in agreement with the nominal pore size.

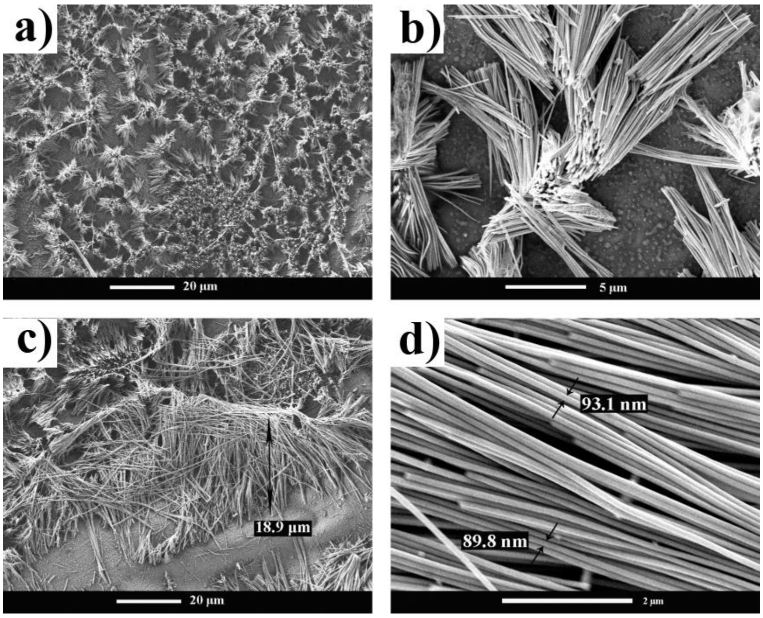

Fig. 3.3.8 a) *Top-view SEM image of Zn nanowires obtained after dissolution of the polycarbonate membrane from 0.2 M* $Zn(TfO)_2$*/[EMIm]TfO on sputtered copper with a copper supporting layer at a potential of −1.0 V versus Zn for 4 h.* ***b)*** *Top view of the Zn nanowires with higher magnification.* ***c)*** *SEM micrograph of the length of the nanowires and* ***d****) SEM micrograph of the diameter of the nanowires.*

The length of the nanowires can be well controlled by the deposition time. Fig. 3.3.9 displays SEM micrographs of freestanding zinc nanowires and of sandwich-like structures obtained at a potential of −1.0 V for 2 h and 8 h, respectively, on the copper sputtered membranes with an electrodeposited copper supporting layer. Vertically aligned zinc nanowire arrays with a length of less than 5 µm are obtained in the first case as shown in Fig. 3.3.9 a). The bottoms of the wires are well separated from each other, while the tops are stuck together forming bunch-like structures. By prolonging the deposition time to 8 h (Fig. 3.3.8 b)) the pores are completely filled up with electrodeposited zinc and finally a thick film is grown over the surface of the template, consistent with the qualitative description of the chronoamperometry measurements. Both the short nanowires and the sandwich-like structure with nanowires in the middle might be of some interest in the field of supercapacitors or catalysis, especially as they can be fully modified in a chemical process.

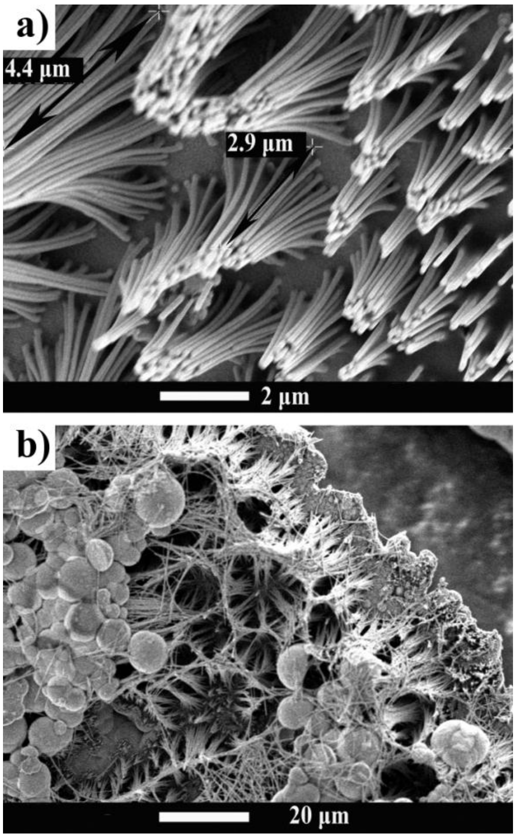

Fig. 3.3.9 *SEM images of free-standing Zn nanowires* ***a)*** *and a sandwich-like structure* ***b)*** *obtained from 0.2 M* $Zn(TfO)_2$*/[EMIm]TfO solutions by electrodeposition at a potential of −1.0 V versus Zn for 2 h and 8 h, respectively, on the copper sputtered membranes with a copper supporting layer.*

3.3.6 Conclusions

In summary, a comparably simple and effective approach to produce vertically aligned Zn nanowires from 1-ethyl-3-methylimidazolium trifluoromethylsulfonate/zinc triflate electrolytes by electrochemical deposition into ion track-etched polycarbonate membranes has been demonstrated. Both the cyclic voltammograms and chronoamperometry measurements show the complicated diffusion and transport process of the Zn^{2+} inside the nanochannels. A supporting zinc or copper layer was deposited on the sputtered side from ionic liquids in order to make the wires free standing. The SEM results show that the diameter of the obtained zinc nanowires is about 90 nm, which is the same as the nominal diameter of the pores, and wire lengths of up to 18 µm could be obtained by controlling the deposition time. Furthermore, short nanowires with lengths of less than 5 µm and sandwich-like structures with nanowires in the middle are also synthesized.

3.4 Electrodeposition of zinc-copper films and free-standing nanowire arrays from ionic liquids

3.4.1. Zn, Cu, and Zn-Cu alloy films from [EMIm]TfO

Fig. 3.4.1 shows the cyclic voltammograms of 0.1 M $Zn(TfO)_2$, 0.1 M $Cu(TfO)_2$ and 0.1 M $Zn(TfO)_2$+0.1 M $Cu(TfO)_2$ in [EMIm]TfO recorded on gold, respectively. The electrode potential was ramped down from the open circuit potential (OCP) to –2.5 V in the forward scan and then up to +1.0 V in the reverse scan with a scan rate of 10 mV s^{-1}. The CV of 0.1 M $Zn(TfO)_2$ in [EMIm]TfO is shown in Fig. 3.4.1 (a). A typical deposition and stripping zinc peak was found at the potential about –2.0 V vs. Pt (c1) and –0.6 V vs. Pt (a1), respectively. A detailed study of zinc deposition from [EMIm]TfO and the morphologies of the deposits can be found in my previous results [113]. Fig. 3.4.1 (b) reveals the electrochemical behavior of 0.1 M $Cu(TfO)_2$ /[EMIm]TfO. In the cathodic range, two reduction processes (c1 and c2) are observed. The first cathodic step at the potential of about –0.2V (c1) might correspond to the reduction of Cu(II) to Cu(I) and the second step (c2) is attributed to the reduction of Cu(I) to Cu. Correspondingly, in the anodic range, two oxidation peaks (a1 and a2) are observed, which are attributed to the oxidation of Cu to Cu(I) and Cu(I) to Cu(II), respectively. Similar behaviors were also reported for the deposition of Cu from ionic liquids [114].

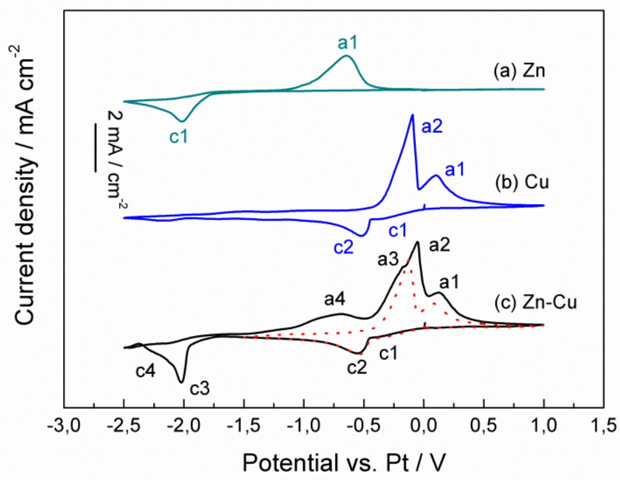

Fig. 3.4.1 *Cyclic voltammograms of 0.1 M* $Zn(TfO)_2$ ***(a)****, 0.1 M* $Cu(TfO)_2$ ***(b)*** *and 0.1 M* $Zn(TfO)_2$*-0.1 M* $Cu(TfO)_2$ *in [EMIm]TfO* ***(c)*** *recorded on gold at room temperature. Scan rate of 10 mV* s^{-1}.

The CV of 0.1 M $Zn(TfO)_2$+0.1 M $Cu(TfO)_2$ in [EMIm]TfO (black line in Fig. 3.4.1 (c)) exhibits four reduction peaks in the cathodic range and four oxidation peaks in the anodic range. The peaks c1 and c2 and their corresponding counterparts a1 and a2 are associated with the reduction and oxidation of Cu(II)/Cu(I) and Cu(I)/Cu, respectively. The reduction peak c3 and its corresponding oxidation peak a3 are related to deposition and stripping of Zn-Cu alloy, respectively. While the peak c4 might be associated with the reduction of Zn and a4 is associated with the oxidation of Zn.

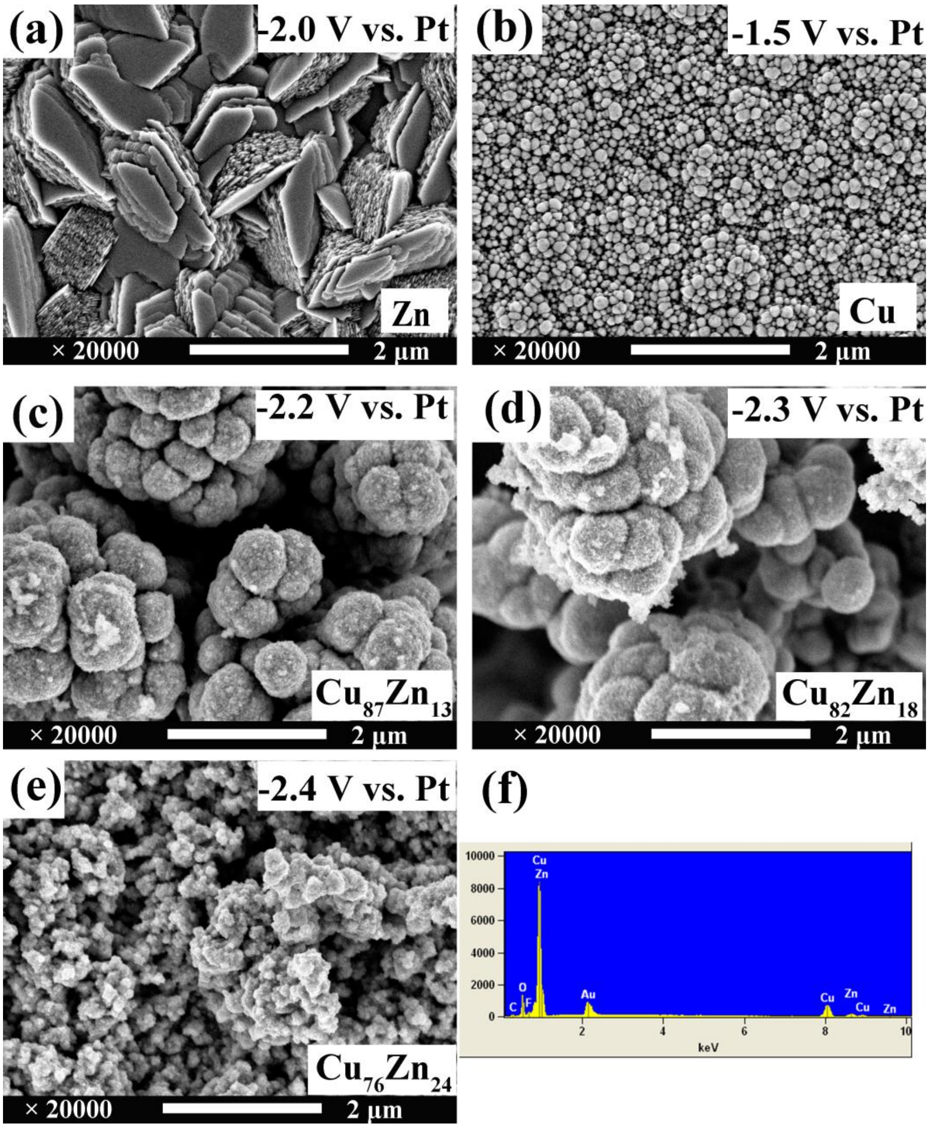

***Fig. 3.4.2** The morphologies of the Zn, Cu and Zn-Cu alloys films obtained by potentiostatic electrodeposition at different potentials and EDX analysis of Cu-Zn alloy obtained at the potential of −2.4 V vs. Pt.*

The potentiostatic electrodeposition of Zn, Cu and Zn-Cu alloys was performed on gold substrates at different potentials for 2 h and the morphologies of the deposits are shown in Fig. 3.4.2. Dense and uniform silver colored zinc deposits with plate like morphology were obtained from 0.1 M Zn(TfO)$_2$/[EMIm]TfO at −2.0 V vs. Pt (Fig. 3.4.2 (a)), while reddish-orange colored Cu deposits with well-adherence to the gold substrate were obtained from 0.1 M Cu(TfO)$_2$/[EMIm]TfO at −1.5 V vs. Pt (Fig. 3.4.2 (b)). Electrodeposition was carried out at −2.2 V, −2.3 V, and −2.4 V, respectively, to synthesize Cu-Zn alloys on gold from 0.1 M Zn(TfO)$_2$+0.1 M Cu(TfO)$_2$/[EMIm]TfO. Spherically shaped structures (Fig. 3.4.2 (c) and (d)) are obtained at potentials of −2.2 V and −2.3 V vs. Pt. The EDX results show the deposits contain 13 and 18 mol % of Zn, respectively, in Fig. 3.4.2 (c) and Fig. 3.4.2 (d). However, the surface morphology is dramatically changed when the deposition potential is set at −2.4 V (Fig. 3.4.2 (e)). The morphology appears nodular with very fine crystallite sizes in the nanometer regime. The EDX results (Fig. 3.4.2 (f)) show that the deposits contain 24 mol % of Zn. As expected, the Zn content in the deposits is increasing as the applied potential shifts to more negative values.

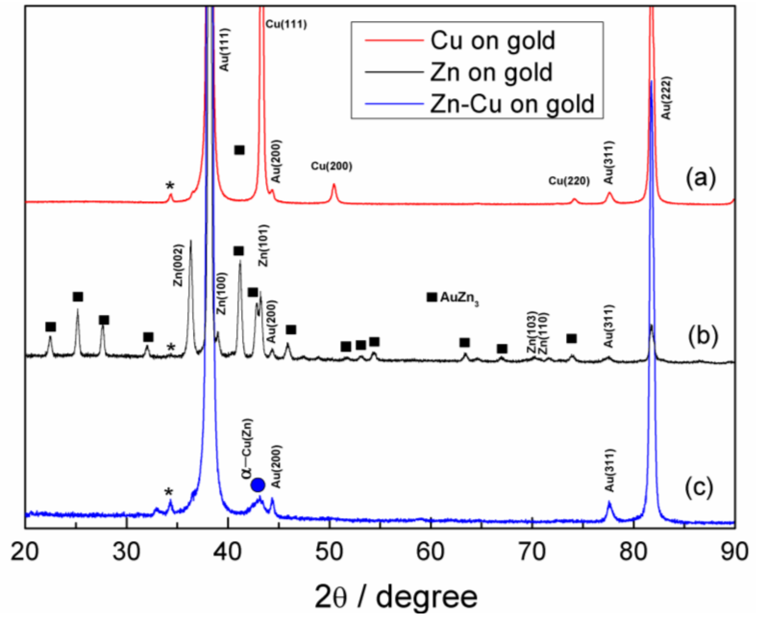

Fig. 3.4.3 *XRD patterns of the electrodeposited Cu, Zn, and Zn-Cu alloys films.*

The XRD patterns of the electrodeposited Zn, Cu, and Cu-Zn alloys on gold are shown in Fig. 3.4.3. Fig. 3.4.3 (a) shows the XRD pattern of Cu films obtained potentiostatically from 0.1 M Cu(TfO)$_2$/[EMIm]TfO at −1.5 V vs. Pt. The XRD pattern of the Cu deposits contained, in addition to the gold diffraction peaks as marked in the Fig. 3.4.3 (a), three diffraction peaks at 2θ = 43.3°, 50.5° and 74.1°, which corresponded to the (1 1 1), (2 0 0), and (2 2 0) crystalline planes of the Cu (JCPDS No. 04-0831), respectively. The peak at ~ 35° marked by an asterisk marked is from gold substrate. In Fig. 3.4.3 (b) (zinc on gold obtained potentiostatically from 0.1 M $Zn(TfO)_2$/[EMIm]TfO at the potential of −2.0 V vs. Pt), the characteristic diffraction peaks at 2θ = 36.3°, 39.0° and 43.2° well agree with the (0 0 2), (1 0 0), and (1 0 1) diffractions peaks of hexagonal zinc (JCPDS File No. 04-0831) and the diffraction peaks marked as black rectangle correspond to $AuZn_3$ (JCPDS File No.50-1336), respectively. Fig. 3.4.3 (c) shows the XRD pattern of Cu-Zn alloys on gold obtained potentiostatically from 0.1 M $Zn(TfO)_2$+0.1 M $Cu(TfO)_2$/[EMIm]TfO at −2.4 V vs. Pt. According to the Cu-Zn equilibrium phase diagram, the electrodeposited copper-rich Cu-Zn alloy with the composition of 24 mol % Zn (Fig. 3.4.2 (f)) at room temperature exhibits the α–Cu(Zn) phase. As can be seen only a small broad peak at 2θ = 41° was observed (marked by a blue circle), which can be attributed to the diffraction of α–Cu(Zn) and no other diffraction peaks due to Cu or Zn were present in the XRD pattern. The diffraction peak at 2θ = 34.2° marked as a star in the pattern is from the gold substrate. This strongly indicates that Zn forms good alloys with Cu. The formation of α–Cu(Zn) phase with a Zn content of less than 35 mol % was also reported in the deposition of Cu-Zn from ionic liquid solutions [115, 116]. However, the peak is broad and the intensity is low. It was reported in literature [117] that the Cu-Zn alloy signals can be observed at –1.6 V vs. Ag and it becomes amorphous when the potential shifts to –2.5 V vs. Ag, indicating the transition of Cu–Zn alloy from crystallized to amorphous as the potential shift to more negative direction. The low intensity might be due to the α–Cu(Zn) alloy being a mixture of crystallized and amorphous phase. Furthermore, according to Scherrer's equation [102], broad peaks indicate a small crystal size of the deposits. This is consistent with the SEM results where the crystal size is in the nanometer regime (Fig. 3.4.2 (e)).

3.4.2 Free-standing Cu-Zn alloy nanowires

Vertically aligned Cu-Zn alloy nanowires were obtained from the solution of 0.1 M $Zn(TfO)_2$+0.1 M $Cu(TfO)_2$/[EMIm]TfO by electrochemical deposition into gold sputtered polycarbonate membranes. Fig. 3.4.4 (a) shows a low magnification image of the free standing Cu-Zn alloy nanowires deposited at −2.4 V vs. Pt for 3 h. With higher magnification (Fig. 3.4.4 (b)), the SEM results show that the nominal diameter of the obtained Cu-Zn alloys nanowires is about 100 nm, which is more or less consistent with the pore diameter of the membrane, and wire lengths of about 5 µm. The length of the wires can be controlled by deposition time. As reported for zinc nanowires, the length of the wires can reach up to 18 µm by deposition for 6 h and less than 5 µm by deposition for 2 h [119]. From the cross section view of the nanowires as depicted in Fig. 3.4.4 (c), it is clear that the wires are free standing.

Zinc nanowires are easily bunched together even if the length of the wire is less than 3 µm [119]. However, the Cu-Zn alloys nanowires are free standing and no bunched structure was observed with lengths of more than 5 µm (Fig. 3.4.4 (a)). The EDX results (Fig. 3.4.4 (d)) show that the alloys contain 25 mol % of Zn. The large amount of Cu in the alloys is responsible for the non-bunched structure, which makes Cu-Zn alloy nanowires more suitable as cathode material than zinc alone in a battery. The XRD pattern of the Cu-Zn alloy nanowires is shown in Fig. 3.4.4 (e). A diffraction peak at 2θ = 41° was observed which is due to the diffraction of α–Cu(Zn) alloy.

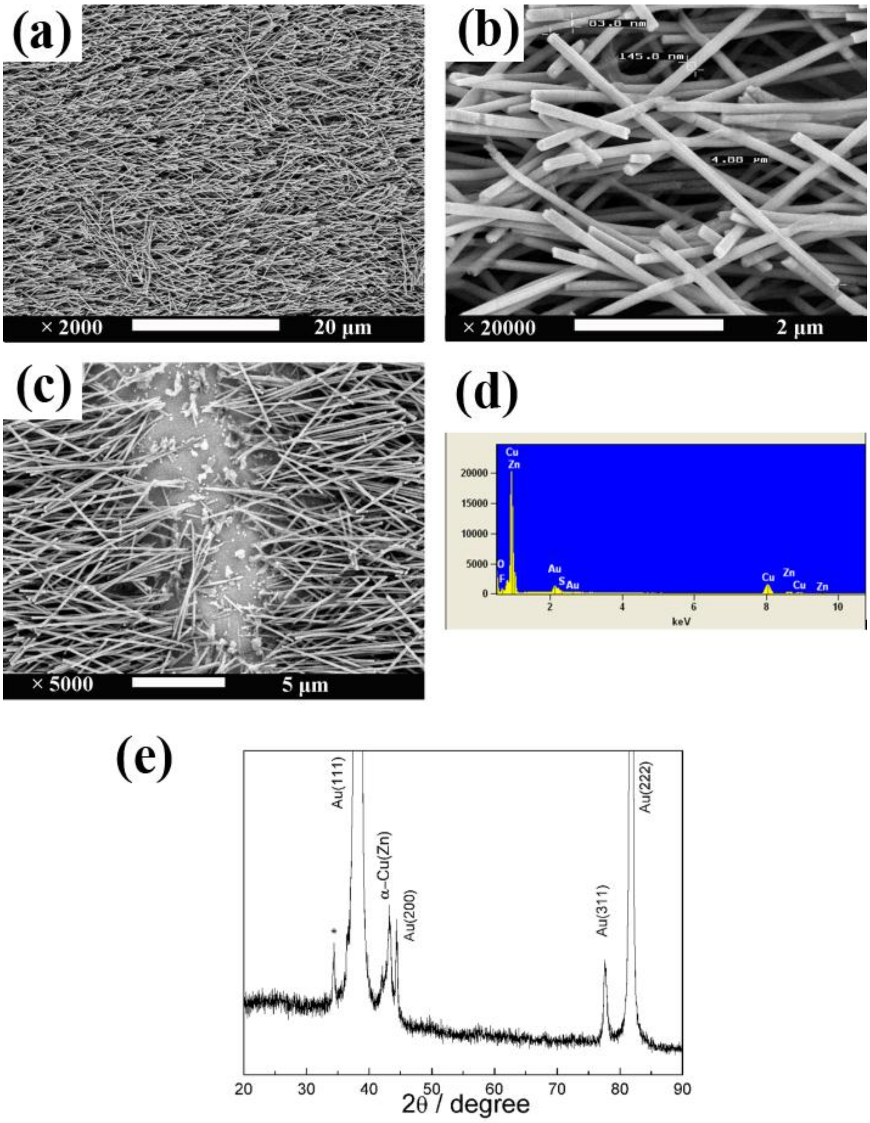

Fig. 3.4.4 (a) *Top-view of Cu-Zn nanowires obtained by deposition at −2.4 V vs. Pt for 3 h from 0.1 M* $Zn(TfO)_2$*+0.1 M* $Zn(TfO)_2$ *in [EMIm]TfO solutions on sputtered gold.* ***(b)*** *high magnification of the nanowires with lengths about 5 µm and diameter of about 100 nm.* ***(c)*** *The interactions of the nanowires with the gold substrate. It is clearly shown that the nanowires are free standing.* ***(d)*** *EDX of the nanowires and* ***(e)*** *XRD pattern of the nanowires.*

3.4.3 Conclusions

It was shown that the electrochemical deposition of Cu-Zn films and nanowires from room temperature ionic liquids is possible. The ionic liquid [EMIm]TfO was used as electrolyte for the electrodeposition of Cu, Zn and Cu-Zn alloy films on a gold substrate. The Cu deposition takes place through two one electron transfer processes from Cu(II) to Cu(I) and Cu(I) to Cu, while zinc is directly reduced by a two electron transfer. The deposits range in Zn composition from 13 to 24 mol % in the obtained Cu-Zn alloys and can be varied by changing the deposition potential. The XRD results revealed that α–Cu(Zn) alloy was formed. The morphology of the Cu-Zn alloy deposits changes from spherical shaped crystallites to nodular shapes crystallites as the potential changes towards more negative values. Free standing Cu-Zn alloys nanowires with average diameters of about 100 nm and lengths of about 5 µm were prepared.

3.5 Influence of an additive on zinc electrodeposition in the ionic liquid 1-ethyl-3-methylimidazolium trifluoromethylsulfonate

3.5.1 CVs of neat [EMIm]TfO and of [EMIm]TfO containing 0.2 M additive

CVs of [EMIm]TfO containing 0.2 M additive (1,2-dimethyl-3-(trifluoromethyl)-1H-pyrazol-2-ium trifluoromethylsulfonate, was obtained from SOLVAY FLUOR, Germany) on gold at different reversal potentials are shown in Fig. 3.5.1. The potential was initially scanned from the open circuit potential (OCP +0.8 V) towards negative direction with a scan rate of 10 mV s^{-1}. The electrochemical behavior of [EMIm]TfO is shown in the inset of Fig. 3.5.1. [EMIm]TfO exhibits an electrochemical window of more than 3 V limited by the irreversible reduction of the organic cation (c3 in the inset of Fig. 3.5.1) and Au oxidation and/or anodic decomposition of the anion (at the electrode potentials above +2.0 V). In the presence of the additive, prior to the reduction of the organic ionic liquid cation (c3), two more peaks (c1 and c2) are observed (black curve), which are correlated with the reduction of the additive. On the reverse scan, the anodic peak a1 might be correlated to the oxidation of the decomposed imidazolium cations at c3, which is only found when the potential was set more negative than –1.8 V. The peak a2 in the blue curve (where the cathodic potential was reversed at –1.2 V) and the peaks a3 and a4 in the red curve (where the cathodic potential was reversed at –1.5 V) are correlated with the oxidation of the reduction products of the additive.

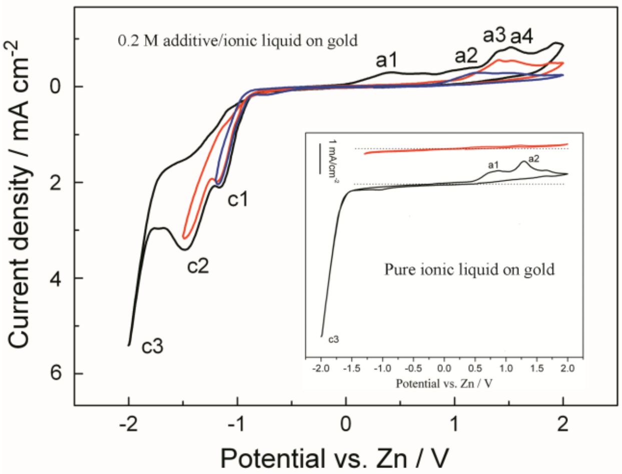

Fig. 3.5.1 *CVs of [EMIm]TfO (inset) and of 0.2 M additive in [EMIm]TfO with different reversal potentials, respectively, on gold at 25 ℃. Scan rate 10 mV/s.*

3.5.2 0.2 M $Zn(TfO)_2$+0.2 M additive in [EMIm]TfO

The CVs of 0.2 M $Zn(TfO)_2$/[EMIm]TfO in the presence and absence of 0.2 M additive on gold electrode with different reversal potentials are shown in Fig. 3.5.2. The cathodic reversal potential in Fig. 3.5.2 black curve was set to –0.8 V before the onset of the cathodic decomposition of the additive. The peaks c1 at –0.7 V and a1 at +0.5 V are attributed to the electrodeposition and stripping of zinc, respectively. As seen, the additive does not alter both Zn deposition and stripping processes when cathodic potential was reversed at –0.8 V. When the potential was reversed at –1.5 V (Fig. 3.5.2 blue curve) the reduction peak (c1) remains unchanged, however the anodic peak (a1) shifts slightly to the more positive direction and the peak current density decreases, suggesting that the anodic stripping process is suppressed by adsorption of the additive and/or its reduction products on the surface of the zinc deposit. By further shift of the cathodic reversal potential to –2.0 V (Fig. 3.5.2 red curve), the anodic peak a1 shifts towards more positive direction and the stripping current density is three times lower compared with the solution of 0.2 M $Zn(TfO)_2$/[EMIm]TfO without additive (Fig. 3.5.2 dotted line), although the shape and the position of zinc reduction peak are identical in both cases. These results suggest that the addition of the additive to $Zn(TfO)_2$/[EMIm]TfO does not influence the overpotential of Zn deposition, but gives a pronounced hindering effect on the stripping process due to the adsorption of the additive on the electrode.

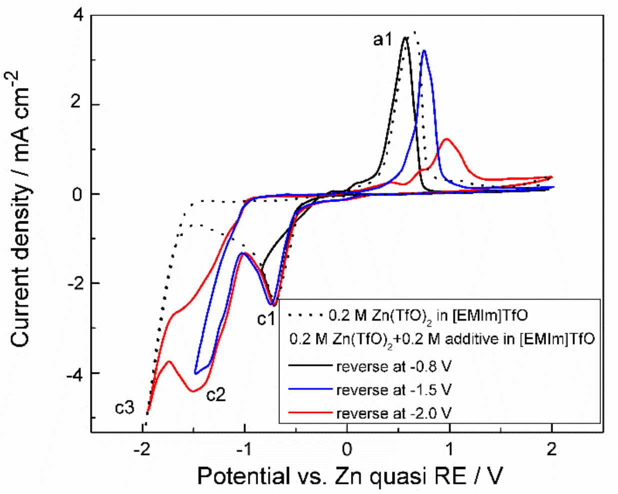

Fig. 3.5.2 *CVs of 0.2 M $Zn(TfO)_2$/[EMIm]TfO without (dotted line) and with 0.2 M additive on gold electrode with different reversal potentials (solid lines). Scan rate 10 mV/s.*

In order to demonstrate the influence of the additive on electrochemical processes, four successive CVs were performed at the same switching potentials, Fig. 3.5.3. Surprisingly, in the following three cycles, the peak at c1 attributed to Zn deposition was strongly influenced and the stripping peak almost disappeared. The results indicate that the adsorption of the additive on the surface inhibits the Zn nucleation in the following cycles.

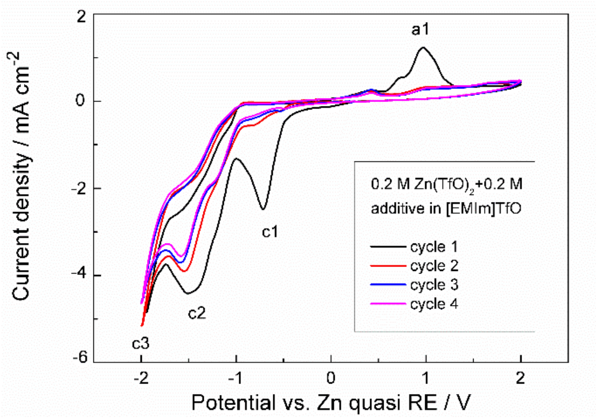

Fig. 3.5.3 *Four successive CVs of 0.2 M Zn(TfO)$_2$+0.2 M additive/[EMIm]TfO on gold electrode at room temperature. Scan rate 10 mV/s.*

The cyclic voltammetry experiments were also performed at 100 ℃, Fig. 3.5.4. In the first cycle, the onset of zinc deposition occurs (c1) at –0.3 V both in the presence and absence of the additive and the stripping occurs at about +0.2 V. However, in the following cycles, the zinc deposition peak potential in the presence of the additive shifts to –0.4 V (Fig. 3.5.4 peak c1) and the current density slightly decreases. The additive has a slight effect on the CVs in the following cycles and almost a reversible Zn deposition/stripping process is obtained at 100 ℃.

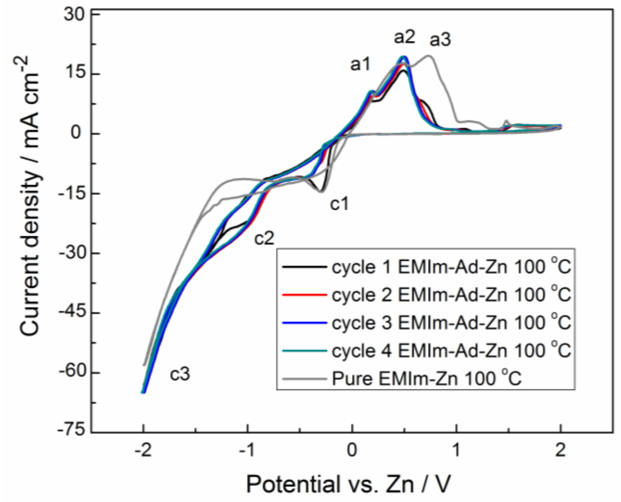

Fig. 3.5.4 *Four successive CVs of 0.2 M Zn(TfO)$_2$+0.2 M additive/[EMIm]TfO on gold electrode at 100 ℃. Scan rate 10 mV/s.*

As the adsorption of the additive on the surface is potential dependent, the change in deposition potential should influence the deposition process, affecting the morphology of the deposits. Therefore, the Zn deposits were prepared by potentiostatic deposition at different potentials from Zn(TfO)$_2$/[EMIm]TfO with 0.2 M additive. For better comparison, the Zn deposits obtained from Zn(TfO)$_2$/[EMIm]TfO without additive at the same potentials were also investigated. In the absence of the additive, Zn electrodeposits obtained at –0.7 V vs. Zn appear to have a plate-like hexagonal microstructure, perpendicular to the substrate. As the potential changed to more negative values (–0.8 V, –1.0 V and –1.2V, respectively, in Fig. 3.5.5 (b)-(d)), the morphologies of the structure still have a plate-like hexagonal structure but with smaller sizes. Visually, the deposits are silvery and uniform with good adherence in all cases.

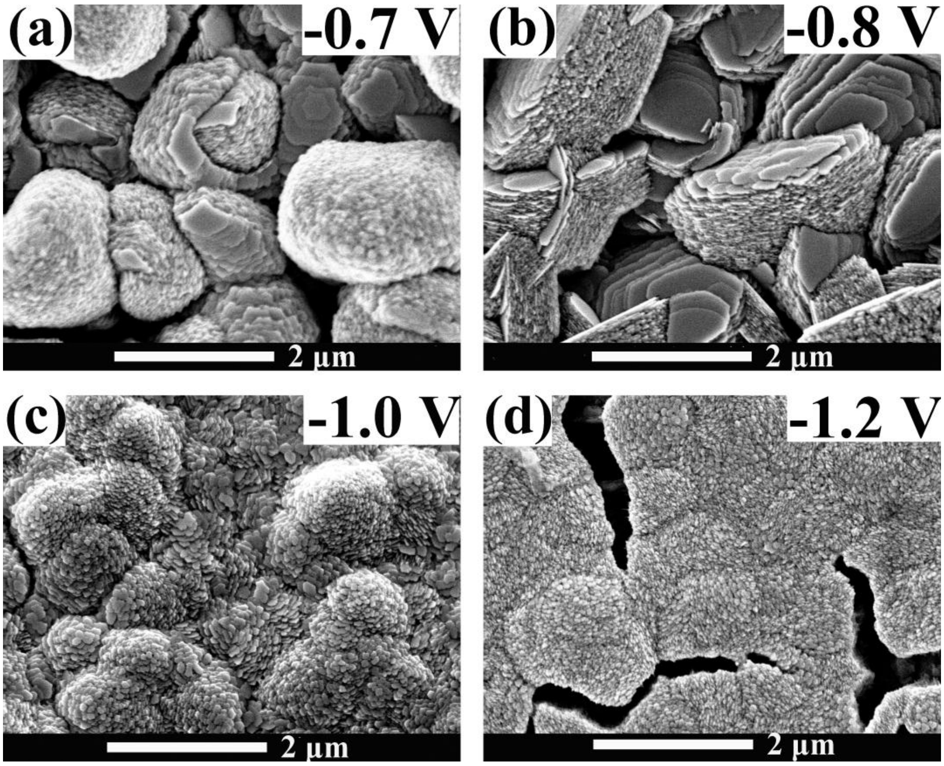

Fig. 3.5.5 *The morphology of the Zn deposit obtained from Zn(TfO)$_2$/[EMIm]TfO in the absence of the additive at –0.7 V, –0.8 V, –1.0 V and –1.2V, respectively.*

In the presence of the additive dark-gray deposits were obtained at –0.7 V and –0.8 V while black deposits were obtained at –1.0 V. The morphologies of the deposits obtained at different potentials reveal the change of the structure from micro-crystalline at –0.7 V to nano-crystalline structure at –1.0 V in the presence of the additive (Fig. 3.5.6 (a)-(c)). The adsorption of the additive on the electrode leads to the observed refining effect at –1.0 V.

However, no deposit was found on the surface by electrodeposition at –1.2 V for 2 h. The results suggest that the strongly adsorbed additive and/or the decomposition products of the additive on the surface inhibit the formation of nuclei by blocking the electrode surface.

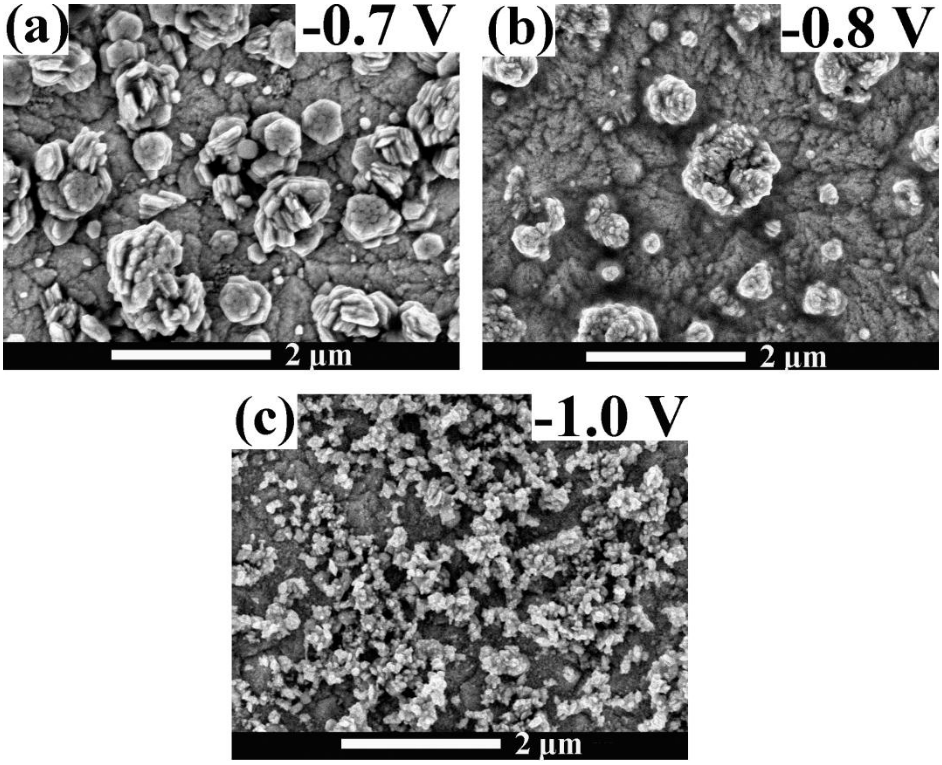

Fig. 3.5.6 *The morphology of the Zn deposit obtained from Zn(TfO)$_2$/[EMIm]TfO in the presence of the additive at –0.7 V, –0.8 V and –1.0 V, respectively.*

The XRD patterns of the Zn deposits obtained at different potentials in the presence of the additive are presented in Fig. 3.5.7. At –0.7 V and –0.8 V, both the XRD patterns exhibit diffraction peaks of Zn (JCPDS File No. 04-0831) with 2θ = 36.3°, 39.0° and 43.2°, which well agree with the (0 0 2), (1 0 0), and (1 0 1) diffraction peaks of hexagonal zinc and of AuZn$_3$ (JCPDS File No. 50-1336) with several distinct diffraction peaks at 2θ = 22.5°, 25.2°, 27.6°, 41.2°, 42.8°, and 45.9°, which agree well with the (2 0 0), (2 1 0), (2 1 1), (3 2 0), (3 2 1) and (0 0 4) diffractions of cubic AuZn$_3$. The two XRD patterns are the same as the pattern of the deposits obtained in Zn(TfO)$_2$/[EMIm]TfO without additive (results are not shown here). However, both the diffraction peaks of Zn and of AuZn$_3$ are less pronounced at –1.0 V in the presence of the additive. Instead, a strong diffraction peak at 2θ = 40.5° is obtained along with the other characteristic diffraction peaks as indicated with dotted lines in Fig. 3.5.7, which are attributed to the diffractions of AuZn alloy (JCPDS File No. 65-5430). Furthermore, the peaks are broad at –1.0 V, indicating a smaller crystal size of the electrodeposited zinc film. The average crystallite size of zinc obtained at –1.0 V was estimated by Scherrer's equation [102] and it was found to be ~32 nm. The adsorption of the additive on the surface influences the preferred orientation and phase formation.

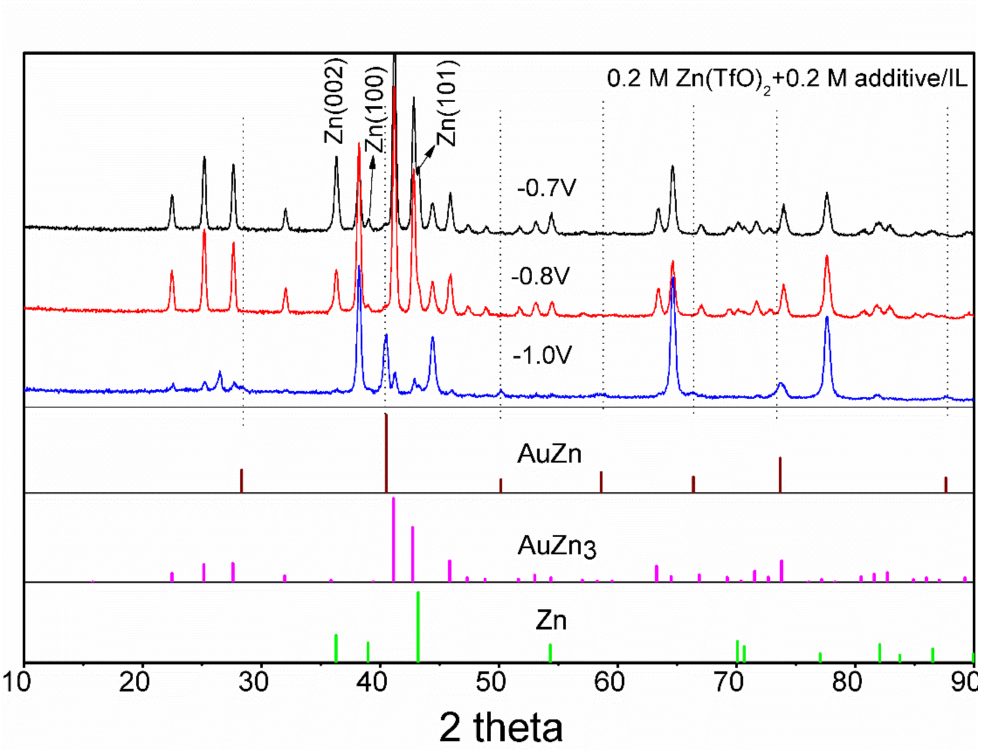

Fig. 3.5.7 The XRD patterns of the Zn deposit obtained in the presence of the additive at –0.7 V, –0.8 V and –1.0 V, respectively.

3.5.3 0.2 M $Zn(TfO)_2$/[EMIm]TfO with different concentrations of additive

Fig. 3.5.8 compares the CVs of 0.2 M $Zn(TfO)_2$/[EMIm]TfO without and with different concentrations of the additive on gold. In the cathodic regime, the peak c1 is assigned to the deposition of zinc and it is clear that in all cases the peak c1 was unchanged both in shape and in the position. The peak c2 is attributed to the reduction of the additive and the current density decreases as the concentration decreases. When the concentration of the additive is reduced to 0.01 M, the peak (c2) has almost disappeared and the curve has the same features as that obtained in the absence of the additive (CV is not shown in the Figure). In the anodic regime, in all cases the stripping peak is due to the oxidation of zinc. However, the stripping peak potential is shifted to more positive values and the peak current density decreases as the concentration of the additive increases. The results reveal that the concentration of the additive also has a distinct effect on the deposition and stripping process of Zn.

The morphology of the Zn deposits obtained by potentiostatic deposition for 2h from $Zn(TfO)_2$/[EMIm]TfO with 0.2 M (a), 0.1 M (b), 0.05 M (c) and 0.01 M (d) additive at –1.0 V are shown in Fig. 3.5.9. Nanocrystalline Zn deposits were obtained with the additive concentration of more than 0.05 M. However, the Zn deposit obtained from $Zn(TfO)_2$/[EMIm]TfO with 0.01 M additive has a micro-structure (Fig. 3.5.9 (d)), analogous to that obtained in the absence of the additive.

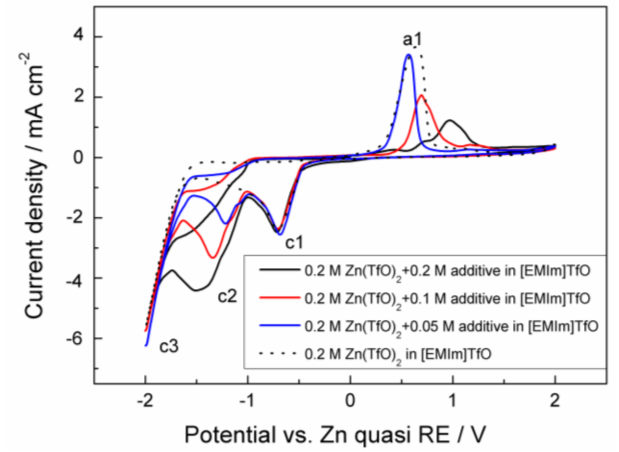

Fig. 3.5.8. *CVs of 0.2 M* $Zn(TfO)_2$*/[EMIm]TfO without (dotted line) and in the presence of 0.2 M, 0.1 M and 0.05 M additive on gold surface (solid lines). Scan rate 10 mV/s.*

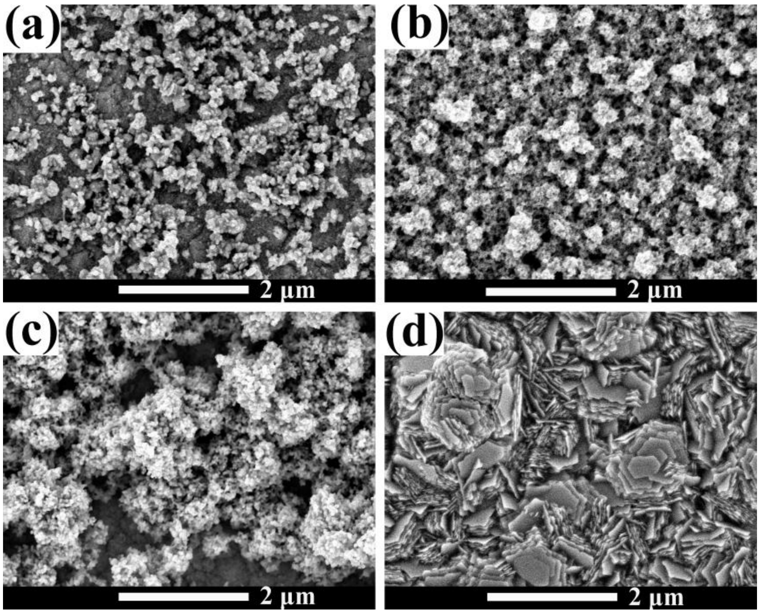

Fig. 3.5.9. *The SEM images of the Zn deposits obtained by deposition at –1.0 V for 2 h from* $Zn(TfO)_2$*/[EMIm]TfO with 0.2 M **(a)**, 0.1 M **(b)**, 0.05 M **(c)** and 0.01 M **(d)** additive.*

The XRD patterns for the deposits obtained from 0.2 M $Zn(TfO)_2$/[EMIm]TfO with different concentrations of the additive (0.01-0.2 M) are presented in Fig. 3.5.10. The electrodeposited layers contain fine crystallites in the nanometer regime with average grain sizes of 32 nm, 48 nm and 26 nm in the presence of 0.2 M, 0.1 M and 0.05 M additive, respectively, calculated using the Scherrer equation, while the Zn deposit obtained with 0.01 M additive shows micro-sized structure.

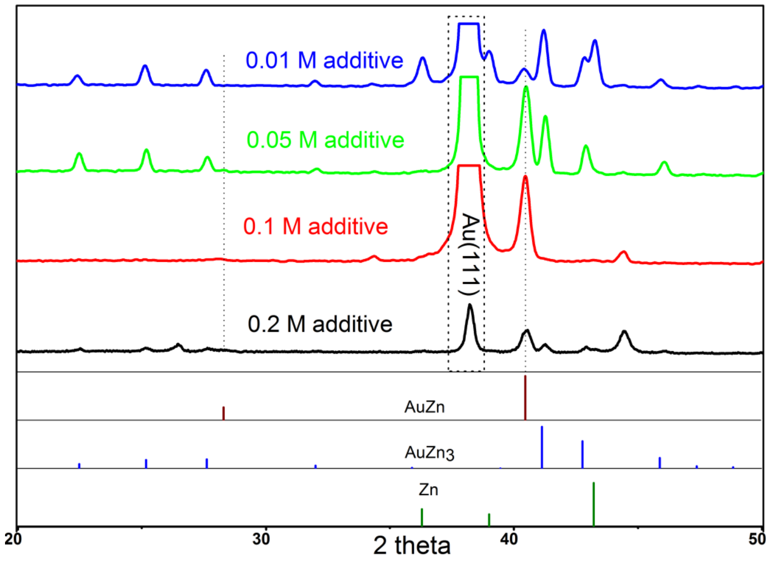

Fig. 3.5.10. XRD patterns of the Zn deposits obtained by deposition at –1.0 V for 2 h from Zn(TfO)$_2$/[EMIm]TfO with 0.2 M, 0.1 M, 0.05 M and 0.01 M additive.

3.5.4 Conclusions

The electrochemical behavior of Zn deposition from 0.2 M Zn(TfO)$_2$/[EMIm]TfO on gold in the presence and absence of an additive has been investigated by CV, SEM and XRD. In the presence of the additive, more than two peaks are observed in the CV, which can be ascribed to the deposition of zinc and decomposition of the additive, respectively. The additive has no effect on the reduction peak of zinc, but the stripping peak is significantly influenced. Nanocrystalline zinc deposits were obtained in the presence of the additive. The effect of the additive becomes more pronounced as the concentration increases. Adsorption of the additive on the surface retards the zinc nucleation and affects the deposit morphology.

3.6 Electrodeposition and stripping of zinc from an ionic liquid polymer gel electrolyte for rechargeable zinc-based batteries

3.6.1 The gel electrolyte

The ionic liquid 1-butyl-1-methylpyrrolidinium trifluoromethylsulfonate ($[Py_{1,4}]TfO$) was selected for the gel polymer electrolyte, due to its large electrochemical window of ~5.8 V. The amount of PVdF-HFP in the ionic liquid gel electrolyte is varied by a gradual increase of the PVdF-HFP amount from 10 to 40 wt%. The conductivity of the gel electrolyte was calculated as described in experimental section 2.5. The conductivity of the gel electrolyte as a function of the PVdF-HFP concentration is shown in Fig. 3.6.1.

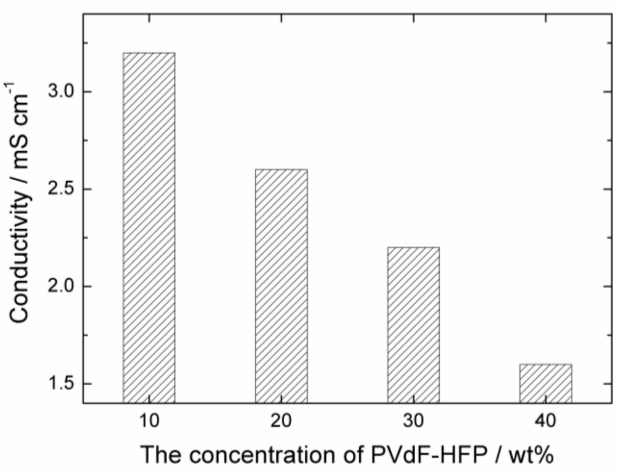

Fig. 3.6.1 *Conductivity of the gel electrolyte as a function of PVdF-HFP concentration.*

An increase of the PVdF-HFP concentration leads to a decrease of the conductivity and an increase of the viscosity and a better mechanical strength of the gel electrolyte. Visually, the gel electrolyte is too sticky and has a glue-like appearance, which will result in the leakage of the IL, at a PVdF-HFP concentration below 20 wt%. The gel electrolyte is too stiff and has a hard plastic-like appearance, which reduces the conductivity too much, at a PVdF-HFP concentration of more than 40 wt%. However, the gel electrolyte is transparent, flexible, and extensible and has a soft rubber appearance, exhibiting a good conductivity of 2.2 mS cm^{-1} at room temperature, with a PVdF-HFP concentration of 30 wt%. As the ion mobility is dependent on the prior swelling of the polymer, in the following experiments, the gel electrolyte was prepared by controlling the weight ratio of the ionic liquid containing 0.2 M $Zn(TfO)_2$ electrolyte to PVdF-HFP at 7:3. These were the optimal conditions for the gel electrolyte made here.

3.6.2 Zinc deposition/stripping on gold from the gel electrolyte

Fig. 3.6.2 shows the cyclic voltammogram of 0.2 M $Zn(TfO)_2$ in the $[Py_{1,4}]TfO$-PVdF-HFP gel electrolyte at room temperature at a scan rate of 10 mV s^{-1}. The electrode potential was scanned from the open circuit potential (OCP) in the negative direction as indicated in Fig. 3.6.2. In the cathodic regime, the peak at c1 is attributed to the bulk deposition of zinc. In the reverse scan, a loop was found, indicating nucleation. In the anodic regime, the peak a1 observed at a potential of about +0.5 V is attributed to the stripping of the electrodeposited zinc. The Zn deposition/stripping process clearly indicates that Zn^{2+} ions are mobile in the polymer electrolyte, and Zn can be deposited and stripped in this gel electrolyte.

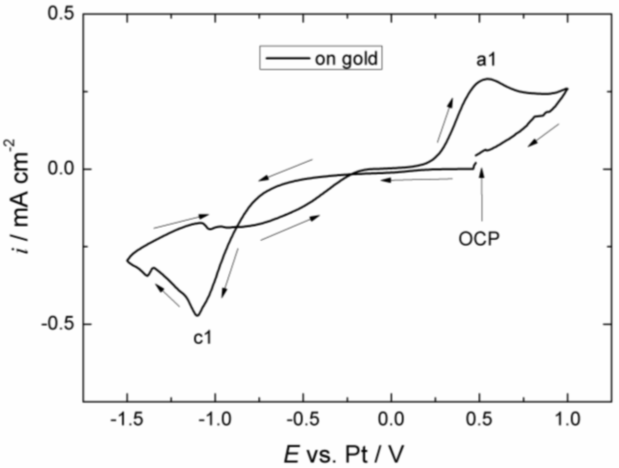

Fig. 3.6.2 *Cyclic voltammogram of 0.2 M* $Zn(TfO)_2$ *in* $[Py_{1,4}]TfO$*-PVdF-HFP gel electrolyte on gold substrate at room temperature at a scan rate of 10 mV/s.*

For a rechargeable zinc-based battery, it is necessary to investigate a series of cycles of zinc deposition/stripping and the morphology of the zinc deposits after several cycles. Therefore, 10 cycles of potentiostatic zinc deposition/stripping were performed first: the potential is kept at $E_{red} = -0.7$ V for 0.5 h, then changed abruptly to $E_{ox} = +1.0$ V for 0.5 h, set back to −0.7 V for 0.5 h. These steps were repeated for 10 times. The viewgraphs of current density versus time after 10 cycles is plotted in Fig. 3.6.3 (a). The current response is mainly due to the Faraday current of Zn deposition or stripping. In the initial state of the potentiostatic deposition, the current density increased rapidly when the potential was applied. This rapid increase in current density may be due to the interfacial layer charging during which cations assemble in front of the cathode or due to an activation polarization of the cathode. Subsequently, the current density dropped which can be attributed to the formation of the initial nuclei on the electrode, consuming the majority of the ions accumulated in front of the cathode. The current density decreased with time and became almost constant after 15 min, suggesting a lower deposition rate under diffusion control (the diffusion coefficient obtained from the Cottrell equation was $4.2 \pm 0.3 \times 10^{-10}$ cm^2 s^{-1}). The current density vs. time curves of the 10 deposition processes in subsequent cycling look similar, which indicates that the Zn^{2+} ion can well migrate in the gel and the gel electrolyte has a good contact with the gold substrate after the stripping processes.

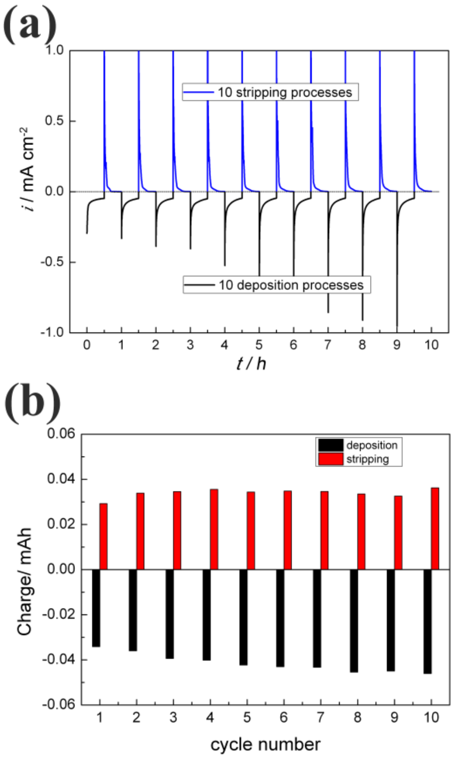

Fig. 3.6.3 (a) *Current density versus time curves of potentiostatic deposition and stripping of zinc on gold substrates at* $E_{red} = -0.7$ *V for 0.5 h and at* $E_{ox} = +1.0$ *V for 0.5 h in the IL polymer gel electrolyte containing 0.2 M* $Zn(TfO)_2$ *for 10 cycles on gold.* ***(b)*** *Charge-cycle number plots of the 10 cycles of Zn deposition/stripping in the polymer gel electrolyte on gold*.

Figure 3.6.3 (b) represents the charge vs. number of cycles of zinc deposition/stripping in the polymer gel electrolyte. The charge passed during deposition did not change much after the fifth cycle. This indicates that the gel electrolyte is quite stable. The Coulombic efficiency decreases gradually in the initial cycles (~85 % in the first cycle) and reaches a stable efficiency after the sixth cycle (~75 %). This means that not all deposited zinc is reoxidized. We found that some zinc remains in the membrane which is no longer available for reoxidation. After 10 deposition/stripping cycles, a slightly black layer was found on the gel electrolyte, i.e., unstripped zinc. In the beginning, I applied a deposition potential of −0.5 V and a stripping potential of +0.5 V, as a result a dark black layer was found on the gel electrolyte. By changing the deposition potential to −0.7 V and the stripping potential to +1.0 V, the black layer can be effectively reduced. Thus, this just seems to be a conditioning problem.

The galvanostatic Zn deposition/stripping on the gold electrode with different given current densities was also investigated. A cathodic current density of 60 μA cm^{-2} is the limiting value, giving an electrode potential of ~ −0.3 V vs. Zn. A current density of 80 μA cm^{-2} leads to a potential of −2 V vs. Zn, revealing that side reactions (IL decomposition) occur.

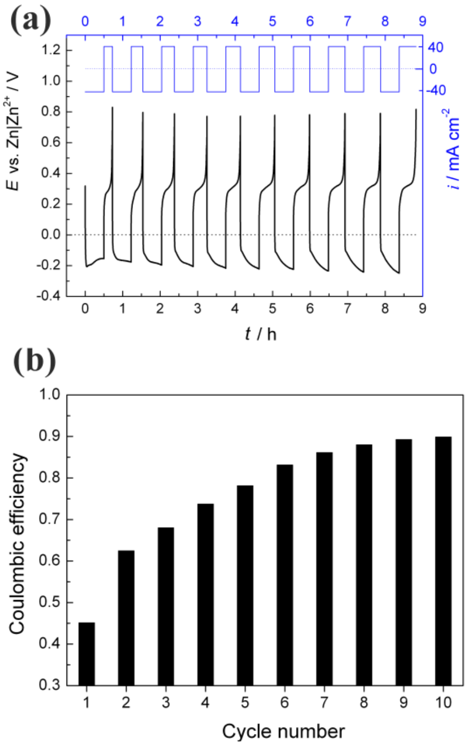

***Fig. 3.6.4 (a)** Voltage-time curves of galvanostatic Zn deposition/stripping on gold electrode for 10 cycles at the current density of −40 μA cm^{-2} for 0.5 h and of 40 μA cm^{-2} for 0.5 h with a cutoff potential of +0.8 V. **(b)** Coulombic efficiency-cycle number plots of the 10 cycles of Zn deposition/stripping in the polymer gel electrolyte on gold.*

The applied anodic current densities of up to 60 μA cm^{-2} lead to oxidation potentials of ~ +0.3 V vs. Zn, followed by a steep increase to ~ +2.5 V vs. Zn when all Zn was consumed. At +2.5 V vs. Zn, a side reaction occurs. Fig. 3.6.4 shows the result of galvanostatic Zn deposition/stripping cycles on gold with a deposition current density of 40 μA cm^{-2} for 0.5 h, and an anodic current density of 40 μA cm^{-2} for 0.5 h at a cutoff potential of +0.8 V, over 10 deposition/stripping cycles. The Zn deposition voltage was located at around −0.2 V and the corresponding stripping voltage was between +0.2 and + 0.4 V. The process was reversed when the potential was more than +0.8 V; otherwise, the potential would increase rapidly to about +2.5 V where side reactions (IL decomposition, Au oxidation) may start. The deposition/stripping efficiency is calculated based on the charge/discharge curves. In the first cycle, the efficiency was only 45 %, which means only half of the deposited zinc was stripped. The observed loss of efficiency may be associated with the formation of the passivation layer on the electrodes surface in the first cycle. However, the efficiency increases as the cycle number increases and an efficiency of more than 85 % was obtained after the seventh cycle. A quasi-reversible Zn deposition/stripping process can be observed.

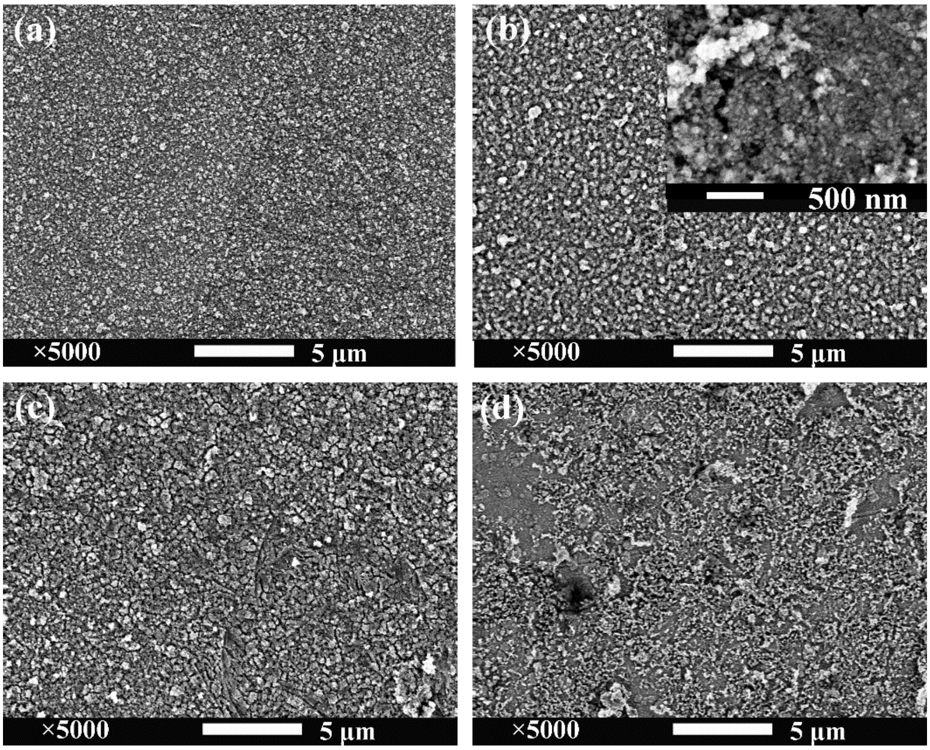

***Fig. 3.6.5** SEM images of the zinc deposits obtained by potentiostatic deposition and stripping of zinc on gold substrates at E_{red} = −1.0 V for 1 h and at E_{ox} = +0.5 V for 1 h with different cycles in the IL polymer gel electrolyte containing 0.2 M $Zn(TfO)_2$.*

In order to find out how the cyclic zinc deposition/stripping process affects the morphology of Zn, we investigated the deposits after different cycles with a high-resolution scanning electron microscope (SEM). Fig. 3.6.5 presents images of the zinc deposits after 1, 2, 5, and 10 deposition and 0, 1, 4, and 9 stripping processes at −1 and +0.5 V, respectively, from the gel electrolyte. Visually, the deposits appear to be thin, dark gray, and well-adhering to the gold substrate. The electrodeposited layers contain fine crystallites in the nanometer regime (with average grain sizes of 40 nm calculated using Scherrer equation [102] from XRD data) as shown in the inset of Fig. 3.6.5 (b). Although nanocrystal deposits can also be obtained from neat [$Py_{1,4}$]TfO as reported in a previously published paper [120], the morphology of the deposits obtained from the gel electrolyte is even smoother without any hint for dendrites. With an increasing number of cycles, the grain size and the morphology of the deposits only slightly change and there is no hint for a dendritic growth.

3.6.3 Zinc deposition on copper from the gel electrolyte

Copper is a candidate as current collector in batteries. One problem is that in contact with organic solutions the Cu current collector can be subjected to corrosion during the electrochemical oxidation/reduction processes, forming surface layers [121, 122]. The compatibility of the IL polymer gel electrolyte with the Cu substrate is thus of fundamental interest. Therefore, zinc electrodeposition/stripping experiments from the IL polymer gel electrolyte were also carried out on a Cu substrate.

The cyclic voltammogram of 0.2 M $Zn(TfO)_2$ in [$Py_{1,4}$]TfO-PVdF-HFP gel electrolyte on a copper substrate is shown in Fig. 3.6.6. Similar to the gold substrate, a typical zinc deposition/stripping process was observed. The zinc deposition and stripping start at potentials of about −0.5 V (vs. Zn) and +0.1 V (vs. Zn), respectively, as indicated by the reduction peak observed in the forward scan and the oxidation peak observed in the backward scan. However, the deposition potential slightly shifts to less negative values on copper compared with gold. Furthermore, the stripping current density was almost twice on copper than on gold, whereas in both cases the deposition current density is almost the same. This suggests a better stripping of zinc from copper.

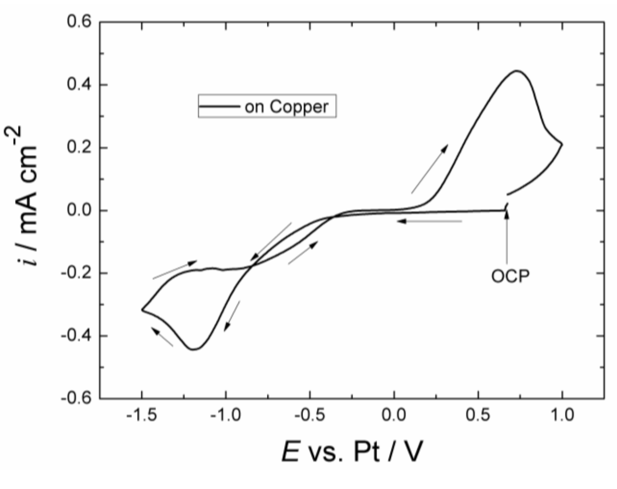

Fig. 3.6.6 *Cyclic voltammogram of 0.2 M* $Zn(TfO)_2$ *in [*$Py_{1,4}$*]TfO-PVd-FHFP gel electrolyte on copper substrate at room temperature at a scan rate of 10 mV/s.*

Fig. 3.6.7 (a) shows the current density/time curves resulting from potentiostatic deposition at −0.7 V for 0.5 h and stripping at +1.0 V for 0.5 h for 10 cycles on a copper substrate. The current densities of the deposition processes recorded on copper are similar to each other in each cycle, suggesting a good electrochemical stability of the copper electrodes with the ionic liquid polymer gel electrolyte. The amount of charge passed during the deposition is a little bit more than that during the stripping as shown in Fig. 3.6.7 (b), indicating an incomplete stripping of zinc. Like on gold substrate, the Coulombic efficiency decreases gradually in the initial cycles (~95% in the first cycle) and reaches a stable efficiency after the sixth cycle (~80%).

The galvanostatic Zn deposition/stripping on the copper electrode was first studied by applying different current densities. The results show that a current density of 40 μA cm^{-2} leads to a safe potential of ~ −0.1 V whereas higher values lead to side reactions. For the stripping process, a current density of 40 μA cm^{-2} leads to a safe potential of 0 ~ +0.3 V before a steep increase occurs due to side reactions once the available Zn is consumed. Therefore, the ionic liquid polymer electrolytes have been evaluated for cyclability property under a current density of 40 μA cm^{-2}.

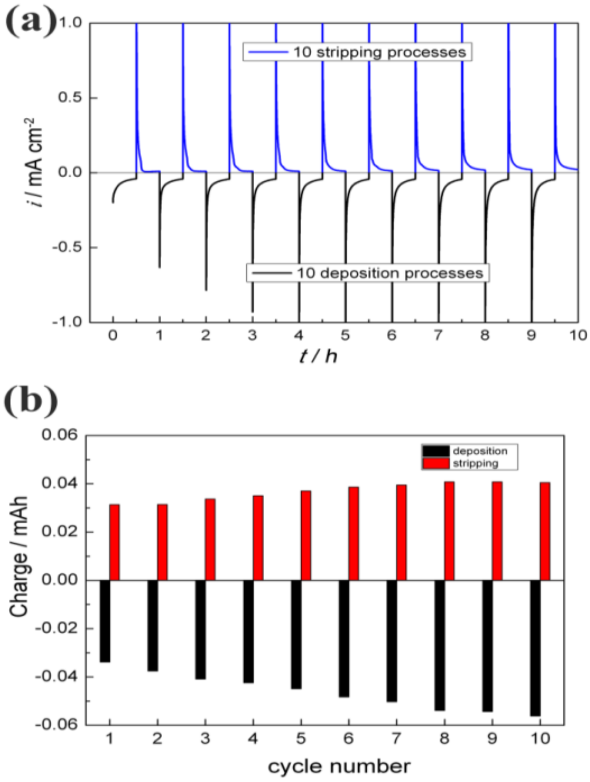

Fig. 3.6.7 (a) *Current density versus time curves of potentiostatic deposition and stripping of zinc on gold substrates at* E_{red} *= −0.7 V for 0.5 h and at* E_{ox} *= +1.0 V for 0.5 h in the IL polymer gel electrolyte containing 0.2 M* $Zn(TfO)_2$ *for 10 cycles on copper.* ***(b)*** *Charge-cycle number plots of the 10 cycles of Zn deposition/stripping in the polymer gel electrolyte on copper.*

Fig. 3.6.8 (a) shows the results of galvanostatic Zn deposition/stripping cycles on copper electrode with the current density kept at 40 μA cm^{-2} for 0.5 h, and changed to 40 μA cm^{-2} for 0.5 h with a cutoff potential of +0.8 V, over 10 deposition/stripping processes. The initial Coulombic efficiency (Fig. 3.6.8 (b)), determined by the ratio between the discharge and charge curves, is only 50%. The observed loss of efficiency may be associated with the formation of the passivation layer on the electrode surface in the first cycle. However, it quickly increases to more than 90% in the subsequent cycles. In particular, the efficiency value is over 95 % after the eighth cycle, which indicates that the cell has quite a good cycling reversibility. This behavior can be explained as follows: in the first cycle Zn can form Zn-Au or Zn-Cu alloys which might be difficult to be stripped; furthermore, some zinc may be deposited in pits of the surface which may not be available for stripping, while in the following cycles more zinc is accumulated on the surface and the available zinc for stripping increases, the efficiency is increased with subsequent cycling.

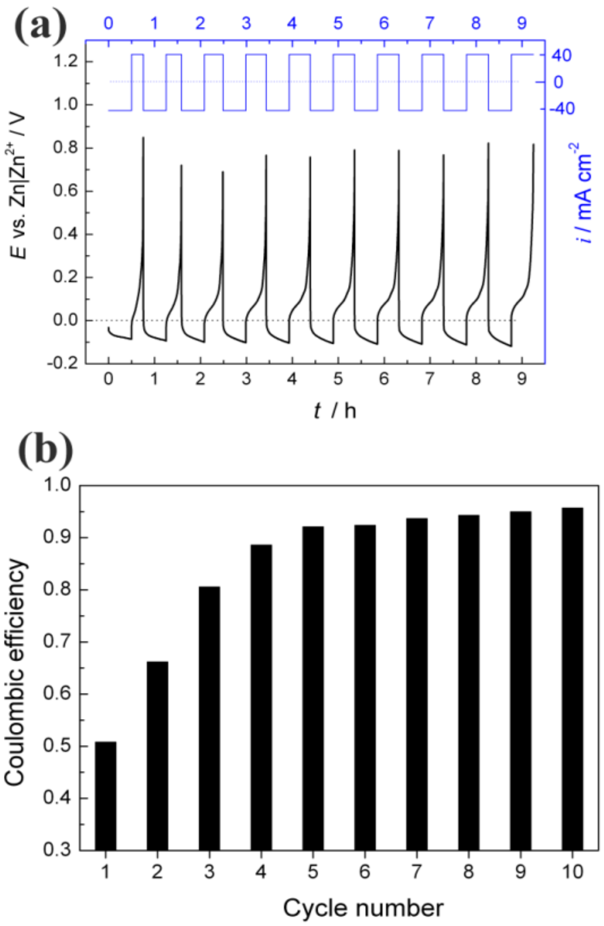

Fig. 3.6.8 (a) *Voltage–time curves of galvanostatic Zn deposition/stripping on copper electrode for 10 cycles at the current density of −40 μA cm^{-2} for 0.5 h and of 40 μA cm^{-2} for 0.5 h with a cutoff potential of +0.8 V.* ***(b)*** *Coulombic efficiency-cycle number plots of the 10 cycles of Zn deposition/stripping in the polymer gel electrolyte on copper.*

Fig. 3.6.9 shows the Coulombic charge/discharge profiles of the polymer gel electrolytes and Coulombic efficiency resulting from potentiostatic deposition at −0.7 V for 0.5 h and stripping at +1.0 V for 0.5 h over 100 cycles on a copper substrate. The cell delivers a Coulombic charge capacity of 0.41 mAh and a Coulombic discharge capacity of 0.38 mAh in the initial cycle. With an increase of the cycle number, the Coulombic charge/discharge increases first and then reaches stability in the 40th cycle. The Coulombic efficiency is 92% in the initial cycle and decreases slightly in the first 5 cycles, then increases again to more than 90% in the initial 20 cycles. The charge and discharge efficiency improves to ~85% in the 40th cycle and gets stable at >80% in the subsequent cycles. Additives and improved deposition/stripping potentials might help to achieve a Coulombic efficiency close to 100%.

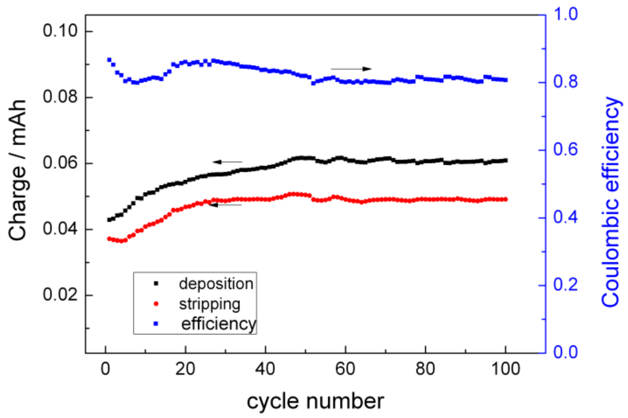

Fig. 3.6.9 Coulombic charge/discharge profiles of the polymer gel electrolytes and Coulombic efficiency resulting from potentiostatic deposition at −0.7 V for 0.5 h and stripping at +1.0 V for 0.5 h over 100 cycles on a copper substrate

Fig. 3.6.10 shows SEM images of zinc deposits on copper, after 1, 2, 5, and 10 deposition processes at –1.0 V and correspondingly 0, 1, 4, and 9 stripping processes at +0.5 V, respectively, from the gel electrolyte containing 0.2 M $Zn(TfO)_2$. Overall, the deposits were relatively rough with some nodules compared with the gold substrate and even after 10 cycles of deposition/stripping there is no dendritic growth, but the different particles are obviously a bit larger than on gold. This seems to be mainly due to the roughness of the copper substrate. Our results show that this polymer gel electrolyte allows the quasi-reversible electrodeposition of Zn on Cu. It is of interest to investigate how the gel electrolyte behaves if 100-1000 cycles are performed and how the deposition/stripping potentials and times influence the cathodic behavior.

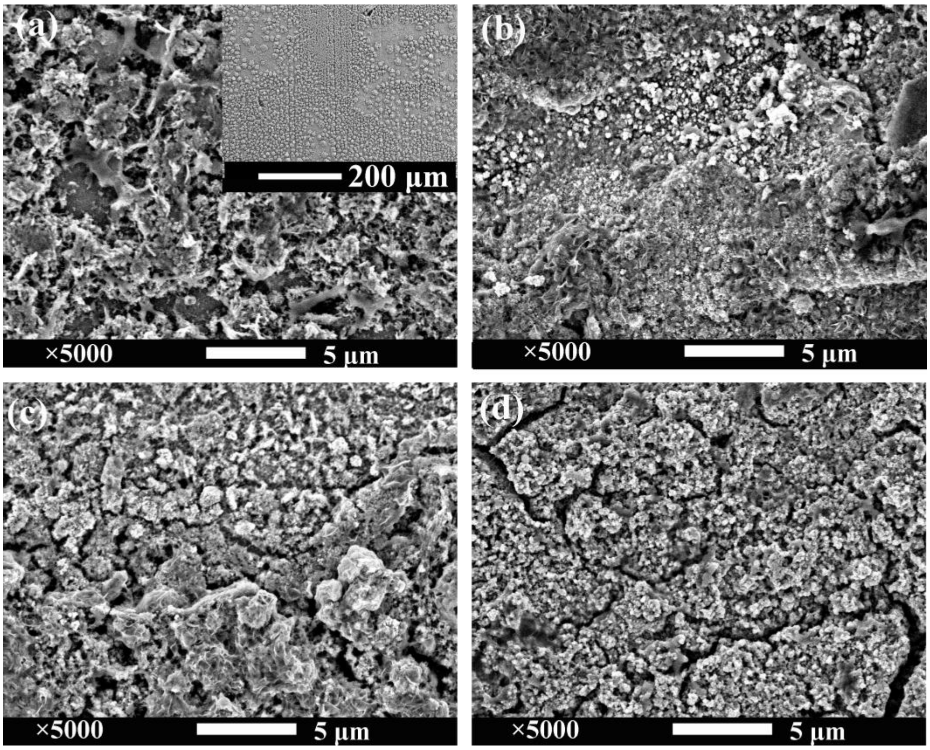

Fig. 3.6.10 *SEM images of the zinc deposits obtained by potentiostatic deposition and stripping of zinc on copper substrate at* $E_{red} = -1.0$ *V for 1 h and at* $E_{ox} = +0.5$ *V for 1 h with different cycles in the IL polymer gel electrolyte containing 0.2 M* $Zn(TfO)_2$*.*

3.6.4 Conclusions

An ionic liquid polymer gel electrolyte made of $[Py_{1,4}]TfO$, 0.2 M $Zn(TfO)_2$, and PVdF-HFP exhibits good conductivity and mechanical properties with 30 wt% of the polymer. The CV, potentiostatic, and galvanostatic deposition and stripping of Zn reveal the quasi-reversibility of zinc deposition/stripping in the gel electrolyte. A relatively smooth zinc film was obtained after 10 deposition/stripping cycles on both gold and copper, which indicates that the gel electrolyte well suppresses dendritic growth. Thus, it can be concluded that $[Py_{1,4}]TfO$-PVdF-HFP polymer gel containing 0.2 M $Zn(TfO)_2$ can be regarded as a promising electrolyte for rechargeable zinc-based batteries.

3.7 *In situ* STM study of zinc electrodeposition on Au(1 1 1) from the ionic liquid 1-ethyl-3-methylimidazolium trifluoromethylsulfonate

3.7.1 Pure [EMIm]TfO

Cyclic voltammograms of the pure [EMIm]TfO on Au(1 1 1) with two different reversal potentials are presented in Fig. 3.7.1. Scans were initially swept cathodically from the open circuit potential (OCP, +0.8 V) with a scan rate of 10 mV s^{-1}. [EMIm]TfO exhibits an electrochemical window of about 4 V limited by the irreversible reduction of the organic cation (c3 in Fig. 3.7.1) and Au oxidation (at the electrode potentials above +2.0 V). By zooming in, two small processes (c1 and c2) can be identified as indicated in the inset of Fig. 3.7.1. As will be discussed later in the *in situ* STM section, the processes are presumably correlated with adsorption of the ionic liquid ions on the Au(1 1 1) surface. The broad anodic processes in the reverse scan (a1 and a2) are mainly correlated with the oxidation of the cation decomposition products as they are only observed when the potential is set below −1.8 V.

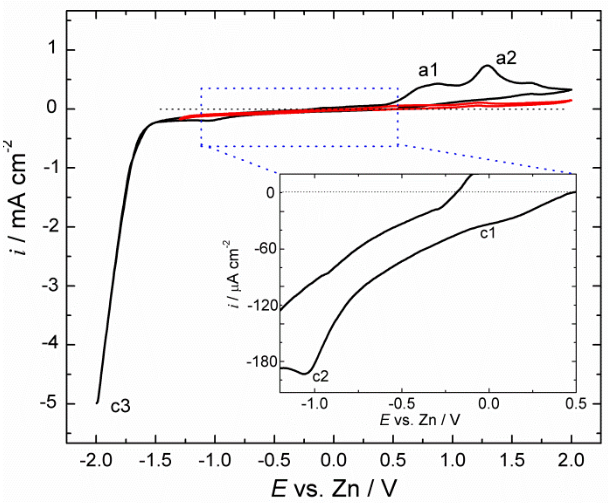

Fig. 3.7.1 *Cyclic voltammograms of [EMIm]TfO on Au(1 1 1) at 25 ℃. Scan rate 10 mV* s^{-1}.

Fig. 3.7.2 shows *in situ* STM images of Au(1 1 1) in [EMIm]TfO ionic liquid during cathodic polarization. At OCP (+0.8 V vs. Zn), the Au(1 1 1) surface is rather rough (Fig. 3.7.2 (a)), the steps are “decorated,” and zooming shows that a “layer” is present at the electrode surface (Fig. 3.7.2 (b)). Between OCP and +0.3 V, the structure of this “layer” remains more or less stable. However, by further decreasing of the electrode potential (the potential regime of c1 in Fig. 3.7.1), the image quality deteriorates as the surface gets mobile and varies from scan to scan (Fig. 3.7.2 (c), (d)). At 0.0 V vs. Zn, the image quality improves again (Fig. 3.7.2 (e))) and a higher magnification shows that tiny holes can be found over the surface (Fig. 3.7.2 (f)). The observed structure can be explained with an interaction of the adsorbed $[EMIm]^+$ ion with the Au(1 1 1) surface. The holes slowly disappear with decreasing of the electrode potential, and at −0.7 V, a relatively smooth Au(1 1 1) surface can be probed (Fig. 3.7.3 (a)). By further reducing the electrode potential (the potential regime of c2 in Fig. 3.7.1), the surface changes again and a "layer" forms on the gold surface (Fig. 3.7.3 (b)). This "layer" grows with time and with decreasing potential (Fig. 3.7.3 (c)). At potentials more negative than −1.5 V vs. Zn, STM images cannot be obtained.

Recently published *in situ* STM and AFM results reveal that interfaces between ionic liquids and electrodes are rather complicated as solvation layers can form which interact with electrode surfaces [123]. It was suggested in [124-126] that the adsorption of cations on the Au(1 1 1) surface leads to the formation of pits and to worm-like structures [125, 126]. The extent and strength of the adsorption of the ionic liquid species are dependent on the applied potential [127] and on the respective ionic liquid. I cannot exclude that the interfaces observed here are also influenced by traces of HSO_3CF_3, as it is difficult to completely remove HSO_3CF_3 from this liquid.

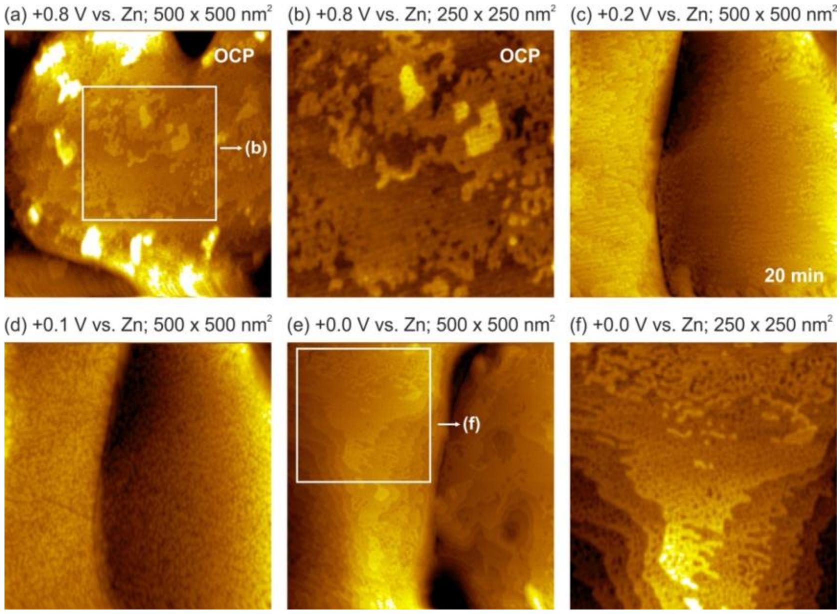

Fig. 3.7.2 In situ *STM images of Au(1 1 1) in [EMIm]TfO between OCP and 0.0 V vs. Zn: (a) +0.8 V vs. Zn; (b) +0.8 V vs. Zn; (c) +0.2 V vs. Zn; (d) +0.1 V vs. Zn; (e) +0.0 V vs. Zn; and (f) + 0.0 V vs. Zn.*

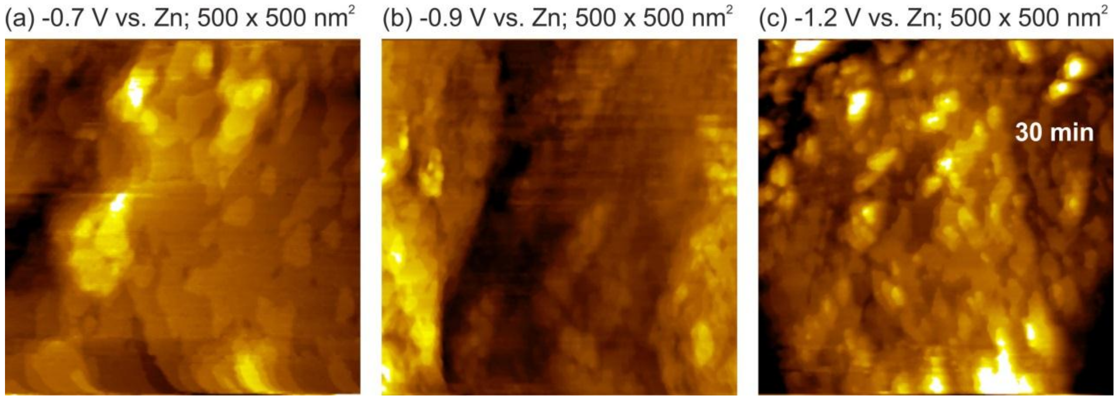

(a) -0.7 V vs. Zn; 500 x 500 nm^2 (b) -0.9 V vs. Zn; 500 x 500 nm^2 (c) -1.2 V vs. Zn; 500 x 500 nm^2

Fig. 3.7.3 In situ *STM images of Au(1 1 1) in [EMIm]TfO at more negative electrode potentials: (a) −0.7 V vs. Zn; (b) −0.9 V vs. Zn; and (c) −1.2 V vs. Zn.*

3.7.2 0.2 M Zn(TfO)$_2$ in [EMIm]TfO

The cyclic voltammogram of 0.2 M Zn(TfO)$_2$ in [EMIm]TfO on Au(1 1 1) is presented in Fig. 3.7.4. The first reduction process c1 (inset in Fig. 3.7.4) is correlated with the underpotential deposition (UPD) of Zn accompanied by the formation of Zn-Au alloys, as evidenced by *in situ* STM results presented below. At c2, the formation of a black deposit is clearly seen. This process is ascribed to the bulk reduction of Zn^{2+} to the metal. On the reverse scan, the deposited Zn is anodically stripped, indicated by two anodic peaks: a1 is due to the stripping of Zn, whereas a2 is associated with the dissolution of Zn-Au alloys. The Zn deposition and formation of Zn-Au alloys were also confirmed by XRD studies [120].

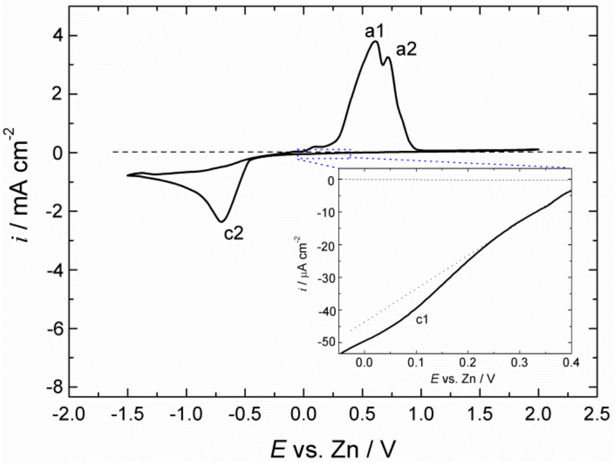

Fig. 3.7.4 *Cyclic voltammograms of 0.2 M Zn(TfO)$_2$ in [EMIm]TfO on Au(1 1 1) at 25 °C. Scan rate 10 mV s^{-1}.*

In situ STM was applied to investigate the initial stages of Zn electrodeposition in the underpotential (UPD) and overpotential (OPD) deposition regimes. Previous *in situ* STM studies have shown that the addition of metal salts to ionic liquids can influence their interfacial behavior [100]. It was reported that the presence of LiCl strongly affects the interactions and the solvation layer structure at the IL/Au(1 1 1) interface. In the case of [EMIm]TfO, the addition of the Zn salt in the ionic liquid has also an influence on the interfacial structure. At the OCP (+0.8 V vs. Zn), instead of the rough surface obtained for pure [EMIm]TfO (Fig. 3.7.2 (a)), a typical terrace-like Au(1 1 1) surface with a step height of 250 pm is probed in the presence of 0.2 M $Zn(TfO)_2$ (Fig. 3.7.5 (b)). Similar to the pure ionic liquid, the image quality gets worse by decreasing the electrode potential, something like a layer is present on the gold surface (Fig. 3.7.5 (b)).When the potential is reduced to +0.3V (potential regime of c1 in Fig. 3.7.4), some islands appear on the surface (Fig. 3.7.5 (c)). There are no such islands at this electrode potential in the pure ionic liquid (Fig. 3.7.2). Between +0.3 and +0.2 V, the size and the height of these islands do not change. However, when the electrode potential is set to +0.1 V, the islands start to grow (Fig. 3.7.5 (d), (e))). This process is very slow, and it takes several hours to get the surface completely covered. At 0.0 V vs. Zn, the islands grow faster; after 40 min, the entire surface is covered, and a rough Zn film starts growing (Fig. 3.7.5 (f)).

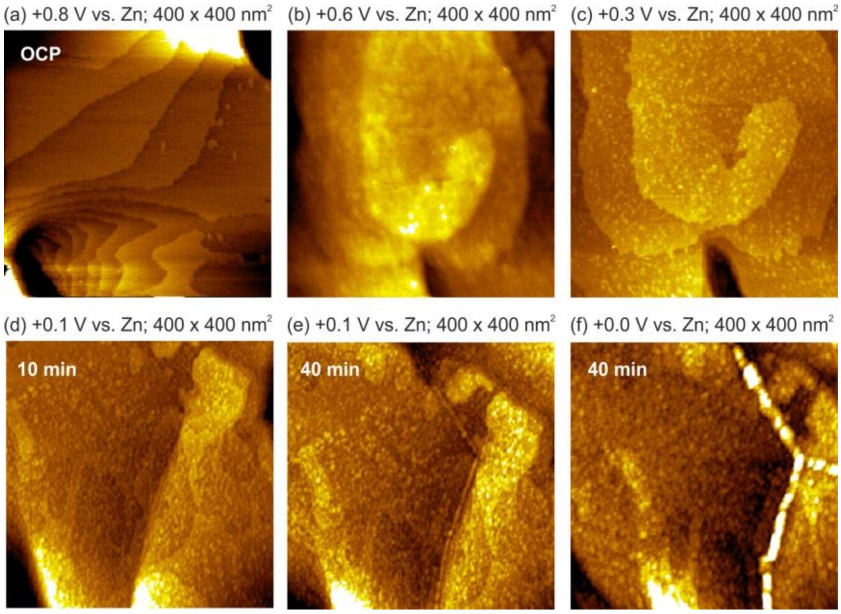

Fig. 3.7.5 In situ *STM images of Au(1 1 1) in 0.2 M $Zn(TfO)_2$/[EMIm]TfO at (a) OCP, (b) +0.6 V, (c) +0.3 V, (d) +0.1 V for 10 min, (e) +0.1 V for 40 min, (f) +0.0 V for 40 min.*

If the electrode potential is set back to +0.7 V, the rapid Zn dissolution is obtained (Fig. 3.7.6 (a)). With time and with increasing the electrode potential, the Au(1 1 1) surface appears rough with 0.3~0.5 nm deep defects as presented in Fig. 3.7.6 (b), which indicates the formation of Zn-Au alloys during the cathodic scan. If the electrode potential is further increased to +1.2 V, gold dissolution starts and the Au(1 1 1) surface becomes porous (Fig. 3.7.6 (c)).

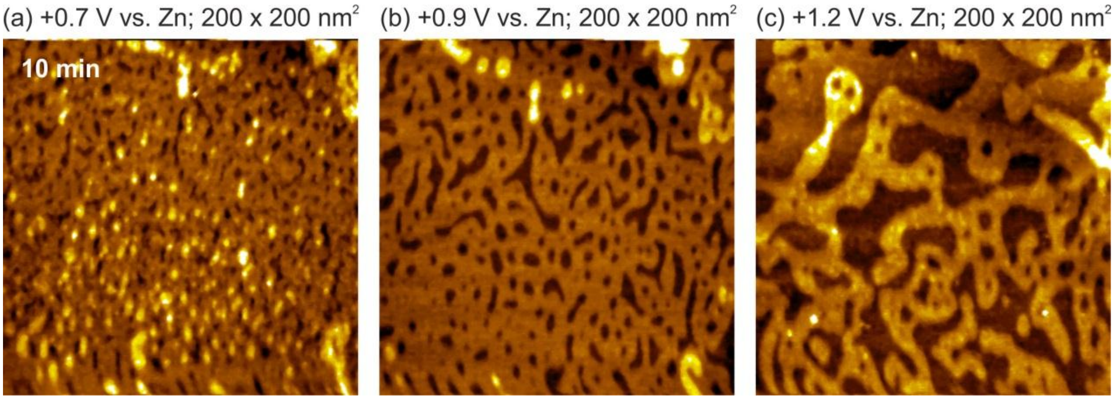

***Fig. 3.7.6** Evidence of the Au-Zn surface alloying: (a)* In situ *STM images of the stripping of the formerly deposited Zn layer; (b) bare Au(1 1 1) surface; and (c) dissolution of the gold surface.*

The appearance of the Au(1 1 1) surface is considerably different if the experiment is repeated without changing the substrate (Fig. 3.7.7). At +0.8 V vs. Zn, some islands form on the "skeleton" of the surface (Fig. 3.7.7 (a)). These islands grow a bit when the potential is reduced to +0.4 V (Fig. 3.7.7 (b)). Between +0.3 and +0.2 V, this surface is more or less stable. However, when the electrode potential is set to +0.1 V, the number of islands significantly increases as shown in Fig. 3.7.7 (c). The islands grow rapidly with time and with decreasing the electrode potential. At 0.0 V vs. Zn, the whole surface is covered by a thin Zn layer (Fig. 3.7.7 (d)).

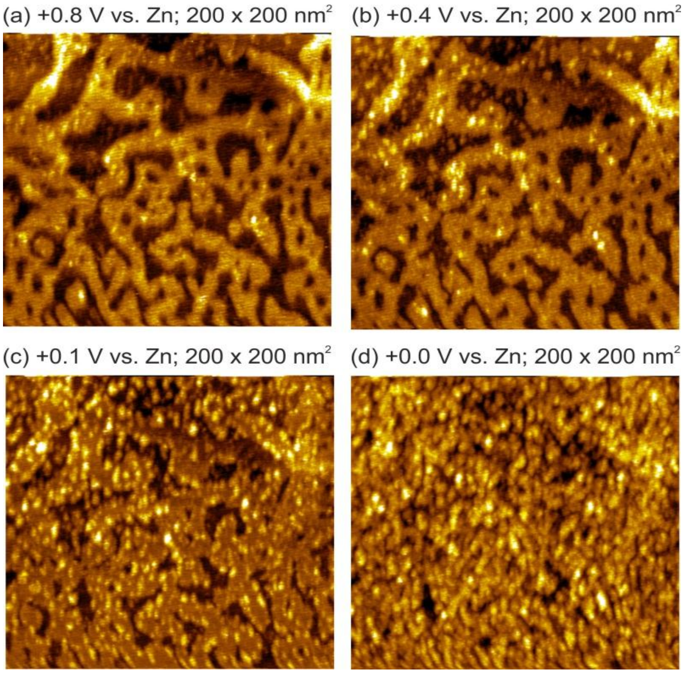

Fig. 3.7.7 In situ *STM images of underpotential deposition of Zn obtained in the cathodic regime during the second STM scan: (a) +0.8 V vs. Zn; (b) +0.4 V vs. Zn; (c) +0.1 V vs. Zn; and (d) 0.0 V vs. Zn.*

Fig. 3.7.8 shows STM images in the OPD regime. If the electrode potential is reduced to −0.1 V, a rough layer of Zn is obtained (Fig. 3.7.8 (a)). The thickness of the deposited Zn layer increases when the potential is further decreased, and at −0.7 V, a relatively thick layer is obtained (Fig. 3.7.8 (b)). The *in situ* STM results can be summarized as follows: first monoatomically high Zn islands grow on the Au(1 1 1) surface to form a thin Zn layer in the UPD regime. Upon further reducing of the potential, bulk Zn deposition sets in and a 3D layer is obtained.

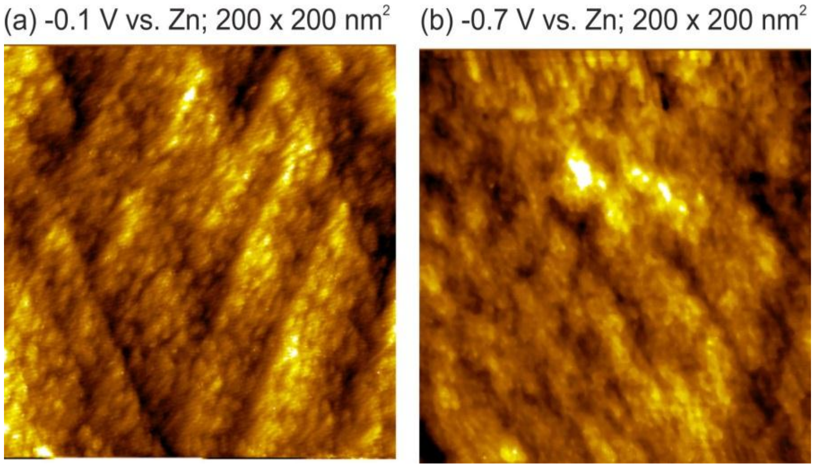

Fig. 3.7.8 In situ *STM images of overpotential deposition of Zn on Au(1 1 1) in 0.2 M $Zn(TfO)_2$/[EMIm]TfO: (a) −0.1 V vs. Zn and (b) −0.7 V vs. Zn.*

3.7.3 Conclusions

An *in situ* STM study of 1-ethyl-3-methylimidazolium trifluoromethylsulfonate ([EMIm]TfO) and of zinc electrodeposition from zinc trifluoromethylsulfonate ($Zn(TfO)_2$) in this ionic liquid on Au(1 1 1) has been presented. *In situ* STM measurements show that the structure of [EMIm]TfO/Au(1 1 1) is complex. At OCP (+0.8 V vs. Zn), the Au(1 1 1) surface is very rough with a “layer” present at the surface. This “layer” changes continuously during cathodic polarization resulting in a porous structure at 0.0 V. The addition of $Zn(TfO)_2$ has a significant influence on the [EMIm]TfO/Au(1 1 1) interface. Instead of a rough surface, rather a typical terrace-like Au(1 1 1) surface is obtained at OCP. The first Zn islands appear at about +0.3 V vs. Zn. These islands grow slowly by decreasing the electrode potential until a thin layer of deposit is formed at 0.0 V. At −0.1 V, a bulk deposition of Zn occurs. Furthermore, *in situ* STM images reveal evidence of Au-Zn surface alloying after dissolution of deposited Zn. The study also shows that the gold surface (and presumably other electrode materials) gets somehow activated by electrodeposition and stripping of zinc.

3.8 Raman and FT-IR spectroscopic studies of 1-ethyl-3-methylimidazolium trifluoromethylsulfonate, its mixtures with water and the solvation of zinc ions

3.8.1. FT-IR of [EMIm]TfO+water mixtures between 2800 and 3800 cm^{-1} (OH stretching vibrations)

Infrared spectroscopy is considered to be a powerful technique for exploring the molecular state of water in different solvents. The OH stretching vibrations are very sensitive to the chemical environment and have been widely used to obtain structural information on interactions of electrolyte-water solutions. FT-IR spectra of neat [EMIm]TfO and with different amounts of water from 5 to 80% (v/v) are shown in Fig. 3.8.1. The mid infrared spectrum of liquid water (Fig. 3.8.1 top, green curve) is composed of a broad band in the range from 2800 to 3800 cm^{-1}.

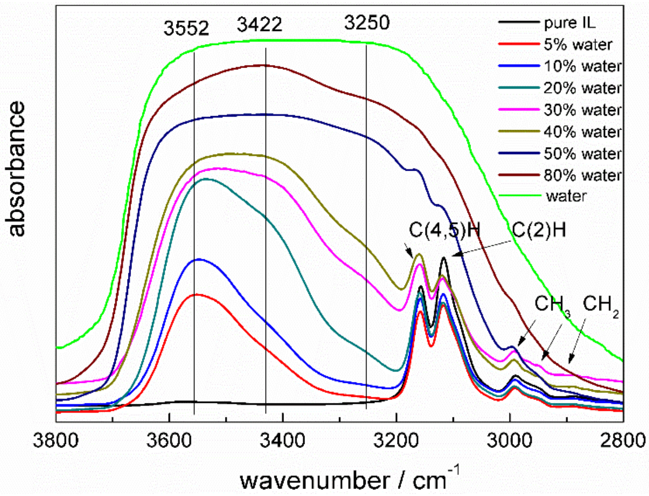

Fig. 3.8.1 *FT-IR spectra of [EMIm]TfO and of [EMIm]TfO+water mixtures between 2800 and 3800 cm*$^{-1}$.

Many attempts were done to explain the OH stretching bands [128-132]. In general, the OH stretching band around 3250 cm^{-1} is assigned to an ice-like component with tetrahedral structure and the band around 3420 cm^{-1} is assigned to an ice-like liquid component. The bands at 3550 and 3620 cm^{-1} are attributed to the OH asymmetric stretching vibrational modes of a liquid like amorphous phase where OH is hydrogen bonded and of free OH group (monomer-like), respectively.

In Fig. 3.8.1, a strong band centered at around 3552 cm^{-1} together with a small peak seen as a shoulder located at around 3422 cm^{-1} was observed for water concentration from 5-20%, indicating that the water molecules are mainly H-bonded to the TfO^- anions. Cammarata *et al.* [133] also reported that water molecules in the ionic liquid rich regime preferentially interact with anions *via* anion···HOH···anion. The intensity of the peak at 3422 cm^{-1} increases with increasing water concentration. A new signal appears at around 3250 cm^{-1}, if the water concentration is increased. The intensity of this signal increases the more water is added and becomes rather broad with a water content of 40-50%. In neat [EMIm]TfO (Fig. 3.8.1 bottom, black curve), the vibration bands are found between 3200 and 2800 cm^{-1}, which are due to CH stretching vibration modes of imidazolium cations as will be further discussed below. Those signals become weaker with increasing water concentration and bulk behavior of water with little [EMIm]TfO signal is observed at water concentration of 50%. The results indicated that large water aggregates are the dominant component at water content of more than 50%, as the spectrum is close to the one of pure water.

3.8.2 Raman spectroscopy of [EMIm]TfO and of 0.2 M $Zn(TfO)_2$/[EMIm]TfO with different amounts of water between 2700 and 3300 cm^{-1} (CH stretching vibration)

Both the OH stretching vibration of water and the CH stretching vibration modes of imidazolium cations are found between 2700 and 3300 cm^{-1}. Unfortunately, they overlap in FT-IR spectroscopy. Therefore Raman spectroscopy was used to investigate the structure change upon addition of water to [EMIm]TfO. The Raman spectra of [EMIm]TfO and of 0.2 M $Zn(TfO)_2$/[EMIm]TfO with different amounts of water in the CH stretching region are shown in Fig. 3.8.2 (a) and 3.8.2 (b), respectively. The peaks at low wavenumbers between 2800 and 3050 cm^{-1} are attributed to CH stretching vibrations of the methyl and ethyl groups of the imidazolium cations. While the peaks at high wavenumbers between 3050 and 3200 cm^{-1} are assigned to the CH stretching vibration of C(2)H, C(4)H, and C(5)H of the imidazolium cation [134, 135]. The Raman spectroscopy of 0.2 M $Zn(TfO)_2$/[EMIm]TfO+water is almost the same both in peak positions and in peak intensities. There are only slightly changes in the CH stretching vibration of C(2)H, C(4)H, and C(5)H of the imidazolium cation, which will be further discussed in the following section. At first glance, the intensities of the peaks are reduced with the addition of water. The intensity of the band at 2970 cm^{-1} as a function of water concentration is plotted in Fig. 3.8.2 (c). Surprisingly, there is a sharp decrease in the intensity when the water concentration is increased from 40 to 50%. A similar behavior was observed by Jeon *et al.* [136] in 1-butyl-3-

methylimidazolium tetrafluoroborate ([BMim]BF_4)+H_2O mixtures at water concentration of 32 ± 2 (~ 55 v/v %) and of 45 ± 2 mol/L (~ 80 v/v %) studied by ATR-IR and Raman spectroscopy. For better comparison with literature, the composition of the mixtures described by different quantities is listed in Table 1.

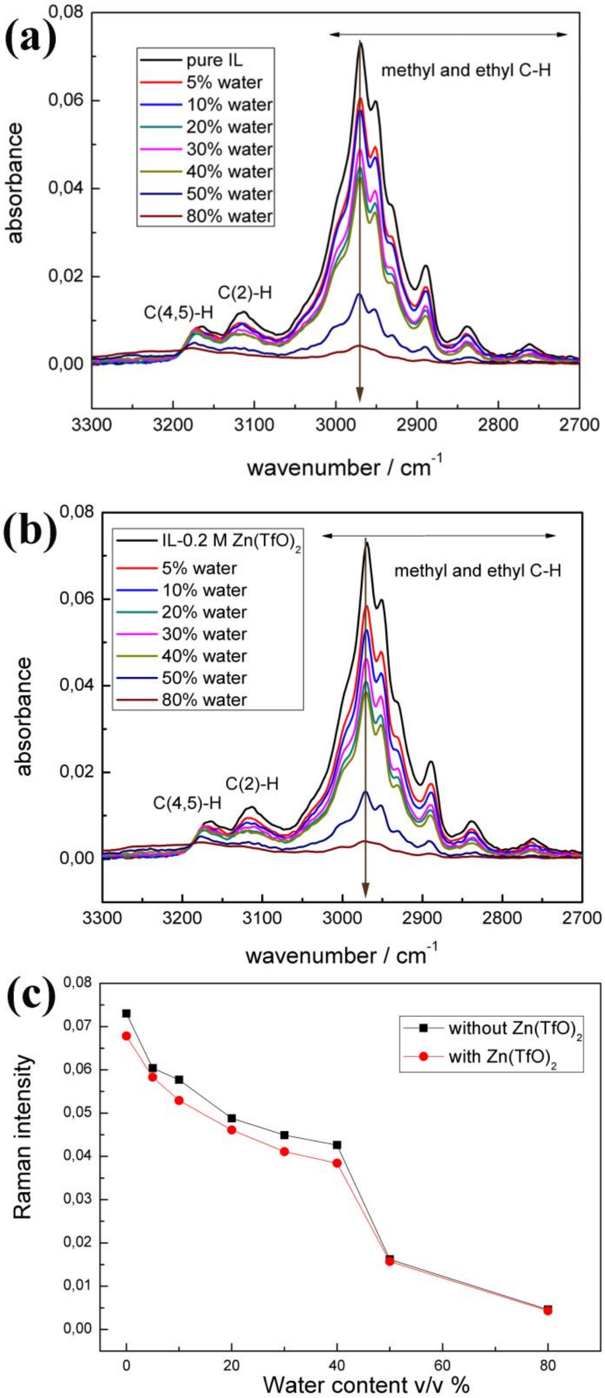

Fig. 3.8.2 *Raman spectra of (a) [EMIm]TfO and of (b) 0.2 M Zn(TfO)$_2$/[EMIm]TfO with different amounts of water in the CH stretching regime. (c) Raman intensity as a function of water concent.*

Table 3.8.1. *The concentration of water in [EMIm]TfO+water mixtures described by volume concentration, mole fraction, molar concentration and mass fraction, respectively.*

concentration	Definition	EMImTfO (IL)+water (w) mixtures						
Volume (%)	V_w/V_{IL+w}	5	10	20	30	40	50	80
Mole (%)	n_w/n_{IL+w}	35	54	72	81	87	91	97
Molar (M)	n_w/V_{IL+w}	2.8	5.5	11	17	22	28	44
Mass (%)	m_w/m_{IL+w}	3.7	7.4	15	23	32	42	74

The observed sharp decrease in the peak intensity in the Raman spectra is a hint for a structural change. It was also reported that the structure of triethylammonium methylsulfonate can change to solvent-separated ion pairs upon addition of four water molecules (80 mol%). The study comprised Far-IR measurements and DFT calculations [137]. Niazi *et al.* revealed that several ionic liquid water mixtures (1-butyl-3-methylimidazolium chloride, 1-ethyl-3-methylimidazolium acetate and 1,3-dimethylimidazolium dimethylphosphate) turned out to be aqueous solutions at water concentrations beyond 75 mol% studied by molecular dynamics simulations [138]. Our experimental results indicated that 40% (v/v) which is equal to 22 mol/L or 87 mol% of water (Table 3.8.1), is needed for such a structural transition. The intrinsic complexity of ionic liquids and their interaction with water molecules could influence the structural transition. When water is added, the interaction between the cations and anions get interrupted by association with water molecules. The anions can interact with water molecules first through H-bonding until they are surrounded by water molecules. Finally, water solvated ions of the former ionic liquid become the dominant species in bulk water. Raman and FT-IR results suggest that the structure transforms from ionic liquid-like to aqueous-like upon addition of water to [EMIm]TfO.

3.8.3 FT-IR of neat [EMIm]TfO and of 0.2 M Zn(TfO)$_2$/[EMIm]TfO between 2800 and 3200 cm^{-1} (CH stretching vibrations)

The FT-IR spectra of neat [EMIm]TfO and of 0.2 M Zn(TfO)$_2$/[EMIm]TfO in the range of 2800 to 3200 cm^{-1} are shown in Fig. 3.8.3. They have been deconvoluted into ten Gaussian bands, respectively. The bands in this range represent the CH stretching vibration modes of imidazolium cations [134, 135]. In neat [EMIm]TfO (Fig. 3.8.3 (a)), the peaks at low wavenumbers between 2800 and 3050 cm^{-1} are attributed to CH modes of the methyl and ethyl groups of the imidazolium cations. The two bands at high wavenumbers (around 3117 and 3157 cm^{-1}) are attributed to the CH stretching modes of C(2)H and of C(4,5)H on the imidazolium ring, respectively. These assignments are consistent with that reported in literature [134, 135].

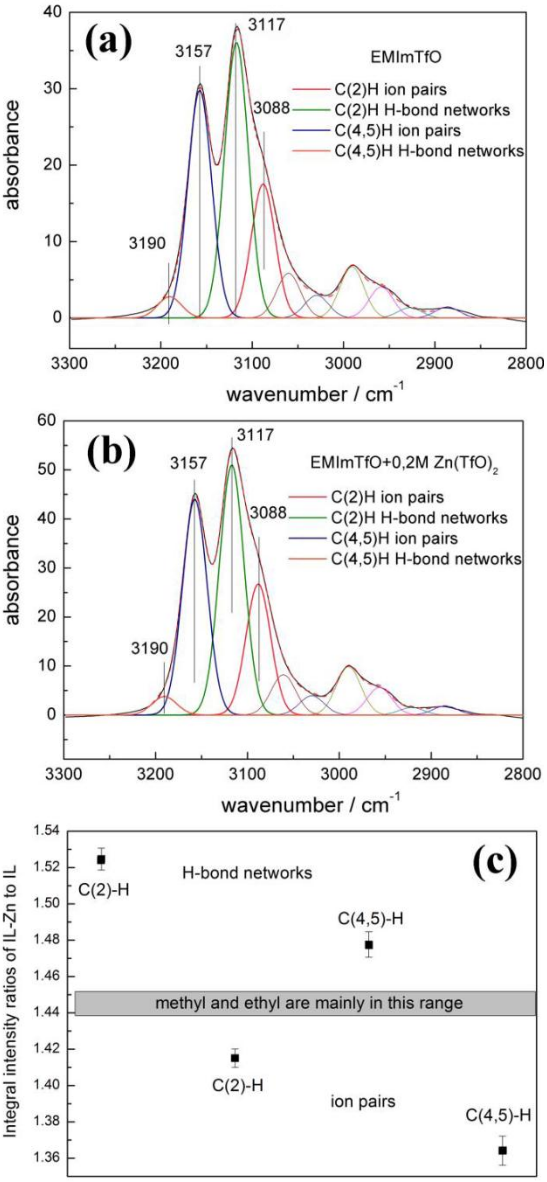

Fig. 3.8.3 *FT-IR spectra of (a) [EMIm]TfO and of (b) 0.2 M Zn(TfO)$_2$/[EMIm]TfO between 2800 and 3200 cm^{-1}, respectively. The spectra are deconvoluted into ten Gaussian bands. (c) The relative ratios of the integral intensities of the deconvoluted peaks.*

The two bands in the imidazolium ring have often been in the focus of research as they can be involved in hydrogen bonding through C(2)H···A or C(4,5)H···A (A: anion). The imidazolium cation can undergo ion clusters and ion pairs. Their corresponding vibrational bands overlap and, therefore, they must be deconvoluted. Deconvoluted bands are found at 3088 (pink peak), 3117 (green peak), 3157 (blue peak) and 3190 cm^{-1} (orange peak), respectively. The two bands at 3088 and 3157 cm^{-1} can be attributed to the C(2)H and

C(4,5)H stretching vibration in ion pairs, respectively while the peaks at 3117 and 3190 cm^{-1} are assigned to C(2)H and C(4,5)H stretching vibration in larger hydrogen-bond networks, respectively. These bands are very sensitive to environmental changes of the ionic liquid. For example, Köddermann *et al.* [134] revealed that the C(2)H and C(4,5)H vibrational bands of hydrogen-bond networks decrease with increasing temperature, whereas those attributed to ion pairs continuously increase. Zheng *et al.* [135] reported that the number of ion clusters decrease and the number of ion pairs increase by addition of acetonitrile to the ionic liquid [BMIm]BF_4. Upon addition of the zinc salt to the ionic liquid in our case, the intensities of these peaks change a bit as shown in Fig. 3.8.3 (b). The relative ratios of the integral intensities of the deconvoluted peaks in 0.2 M $Zn(TfO)_2$/[EMIm]TfO to those in [EMIm]TfO are shown in Fig. 3.8.3 (c). The ratios of the CH stretching vibrations of the methyl and ethyl groups are nearly constant and are located in the range of the gray bar shown in Fig. 3.8.3 (c). However, the relative ratio of the C(2)H and C(4,5)H vibrational modes of hydrogen-bond networks is increased (above the gray bar) while the relative ratio of the C(2)H and C(4,5)H vibrational modes of ion pairs is decreased (below the gray bar). This indicates that the hydrogen-bond network is favored and the contribution of ion pairs decreases upon addition of the zinc salts. This is consistent with the increase in the viscosity and the decrease in the conductivity on addition of metal salts to ionic liquid electrolytes. Upon addition of zinc salts to the ionic liquid, zinc ions are solvated by the anions leading to zinc-ion complexes. The TfO$^-$ anions are less moveable compared to pure [EMIm]TfO, which leads to stronger hydrogen-bonding. The [EMIm]$^+$ cations can also undergo a conformational change that favors hydrogen-bonding. It was reported that the ethyl group of [EMIm]$^+$ cation can rotate along the C-N bond, yielding non-planar and planar conformers [139].

3.8.4 Raman spectroscopy of [EMIm]TfO+water mixtures between 300 and 1300 cm^{-1} (vibration modes of TfO$^-$ anion)

The Raman spectra of [EMIm]TfO+water mixtures between 300 and 1300 cm^{-1} are shown in Fig. 3.8.4. The resulting vibrational bands of TfO$^-$ anions are assigned as follows: the asymmetric stretching $\nu_{as}(SO_3)$, located at 1260 cm^{-1} in neat [EMIm]TfO is gradually red shifted to 1252 cm^{-1} with increasing water concentration. The symmetric stretching $\nu_s(SO_3)$, the asymmetric stretching $\nu_{as}(CF_3)$ and the symmetric stretching $\nu_s(CF_3)$ modes are located at 1034, 1173 and 1230 cm^{-1}, respectively [140, 141]. They do not shift upon increasing water concentration. The symmetric deformation $\delta_s(CF_3)$, the asymmetric deformation $\delta_{as}(CF_3)$ and the symmetric stretching $\nu_s(C-S)$ modes are located at 757 cm^{-1}, 573 cm^{-1} and 315 cm^{-1} , respectively, and are gradually blue shifted to 765 cm^{-1}, 577 cm^{-1} and 319 cm^{-1} with increasing water concentration. It was reported that the oxygen atoms of $CF_3SO_3^-$ have larger negative charges than the fluorine atoms [142].

Therefore, the more negatively charged oxygen atoms preferably associate with H_2O through hydrogen bonding. The increase in the strength of the hydrogen bond $SO_3\cdots H_2O$ resulted in a shortening of the hydrogen bonds $SO_3\cdots H_2O$ and a lengthening of the covalent bonds S−O. The weaker force constants for the S−O bonds lead to lower wavenumbers and thus red shifted vibrational bands. However, due to the Coulomb forces and hydrogen bonding, the deformation mode of CF_3 and stretching mode of C−S are blue shifted upon addition of water. These shifts clearly indicate the change of the coordination environment of the TfO$^-$ anions upon addition of water. The interaction strength between cation and anion upon addition of water is discussed in the following section.

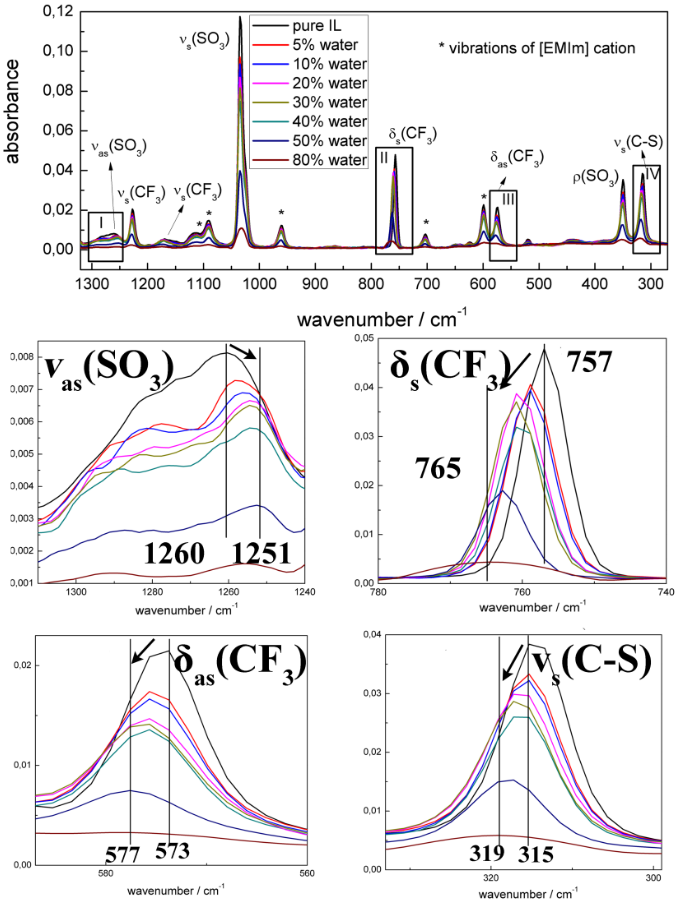

__Fig. 3.8.4__ Raman spectra of [EMIm]TfO and of [EMIm]TfO+water mixtures between 270 and 1300 cm^{-1}.

3.8.5 Cation-anion interaction of [EMIm]TfO+water mixtures between 30 and 300 cm^{-1} investigated by far infrared spectroscopy

The FIR spectra of [EMIm]TfO+water mixtures in the range of 30-300 cm^{-1} are shown in Fig. 3.8.5. The vibrational bands centered at about 210 cm^{-1} are due to the rocking modes of CF_3 (ρCF_3) and they do not shift upon increasing water concentration.

The research group of Ludwig has intensively investigated the cation-anion interaction of ionic liquids by FIR spectroscopy in combination with DFT calculations [137, 143-149]. The low frequency vibrational signals below 200 cm^{-1} are assigned to bending and stretching modes of the $^{+}C{-}H\cdots A$ or $^{+}N{-}H\cdots A$ (A: anion) describing the cation-anion interaction. Therefore, the vibrational band centered at around 88 cm^{-1} in neat [EMIm]TfO is assigned to the interaction between [EMIm]$^{+}$ cations and TfO^{-} anions. The intensities of those vibrational bands are gradually reduced and a red shift of the frequencies is observed for water content from 5-20%, suggesting that the interaction between cations and anions, as a consequence of the association with water molecules, gets weaker. The peak is no longer assignable at a water content of more than 30% as the anions are fully surrounded by water molecules.

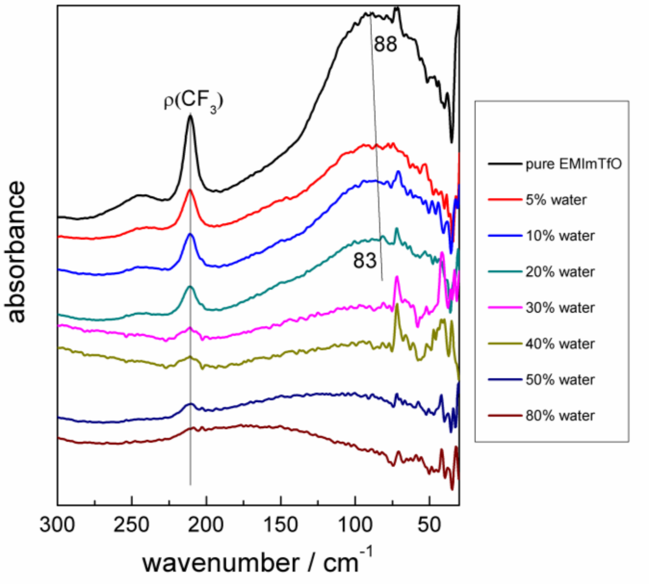

Fig. 3.8.5 *FIR spectra of [EMIm]TfO and of [EMIm]TfO+water mixtures between 30 and 300 cm^{-1}. The bands below 200 cm^{-1} indicate the cation-anion interaction.*

3.8.6 The solvation of Zn ions in neat [EMIm]TfO and in [EMIm]TfO+water mixtures

Some vibrational modes are known to be very sensitive to the coordination environment in ionic liquid solutions, such as bis(trifluoromethylsulfonyl)amide (TFSA) [150-152] and trifluoromethylsulfonate (TfO^-) [140, 153]. It was reported that the frequency of “free” TFSA anions located at about 742 cm^{-1} ($\delta_s(CF_3)$) in Raman spectra shifted to 748 cm^{-1} when it was coordinated with Li^+ [151]. In “free” TfO^- anions, the comparable frequency was located at about 757 cm^{-1} ($\delta_s(CF_3)$) and shifted to 766 cm^{-1} when triflic acid was added to the solution [153]. The Raman spectra of [EMIm]TfO and of 0.2 M $Zn(TfO)_2$/[EMIm]TfO between 740 and 780 cm^{-1} are presented in Fig. 3.8.6 (a). The local environment of the TfO^- anions in [EMIm]TfO and in 0.2 M $Zn(TfO)_2$/[EMIm]TfO electrolytes was investigated by monitoring the CF_3 symmetric deformation, $\delta_s(CF_3)$, of which the vibrational mode was located at 757 cm^{-1}. When zinc salt is added to the solution, a new signal appears between ~762 and 772 cm^{-1} which is associated with Zn^{2+} coordinated TfO^-. The spectrum can be deconvoluted into two peaks and the results are shown in Fig. 3.8.7. The peak for Zn^{2+} coordinated TfO^- is centered at 766 cm^{-1}. The average number of TfO^- coordinated to each Zn^{2+} ions can be calculated according to the Raman peak areas, as described in literature [151].

$$N = \frac{A_{co} / (A_{co} + A_{free})}{n_{Zn} / n_{total\,TfO^-}}$$

where A_{co} and A_{free} are the peak areas of the coordinated and of the free TfO^- at 766 and 757 cm^{-1}, respectively. n_{Zn} is the mole concentration of $Zn(TfO)_2$ (0.2 M) and $n_{total\ TfO^-}$ is the total mole concentration of TfO^-, which is equal to n_{IL} (at room temperature n_{IL} = 5.33 M) + 2 × n_{Zn} (0.4 M).

The calculated average number of TfO^- coordinated to each Zn^{2+} ions is 3.8, which indicates that Zn^{2+} ions coordinates four TfO^- ions. It is likely that $[Zn(TfO)_4]^{2-}$ complexes together with $[Zn(TfO)_3]^-$ complexes are present in the solution. However, in the presence of water, taken 5% water as an example, as shown in Fig. 3.8.6 (b), only one peak at 759 cm^{-1} was observed, which shows in direct comparison the change of the coordination environment of Zn^{2+}. In ionic liquid+water mixtures, Zn^{2+} ions are obviously mainly associated with water forming aqueous complexes of the type $[Zn(H_2O)_n]^{2+}$ with n = 1-6 [103]. The presence of smaller sized complexes $[Zn(H_2O)_n]^{2+}$ is one of the factors that accounts for the increased conductivity and decreased viscosity of water containing ionic liquid electrolytes. Therefore, the electrochemical performance of ionic liquid+water mixtures, as electrolytes for electrodeposition of zinc, was largely improved as shown in a previous report [120].

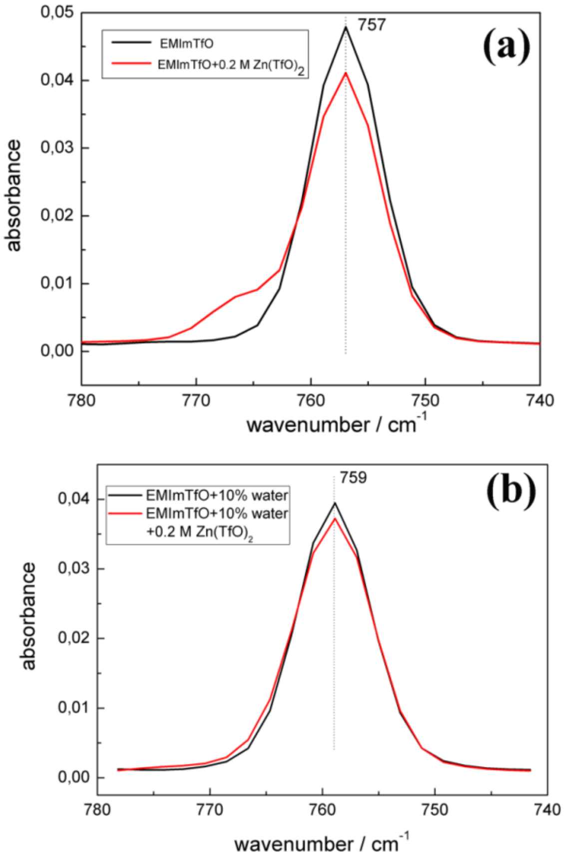

Fig. 3.8.6 *Raman spectra of [EMIm]TfO and of 0.2 M* $Zn(TfO)_2$*/[EMIm]TfO* ***(a)*** *between 740 and 780* cm^{-1} *and their mixtures with 5% water* ***(b)****, respectively.*

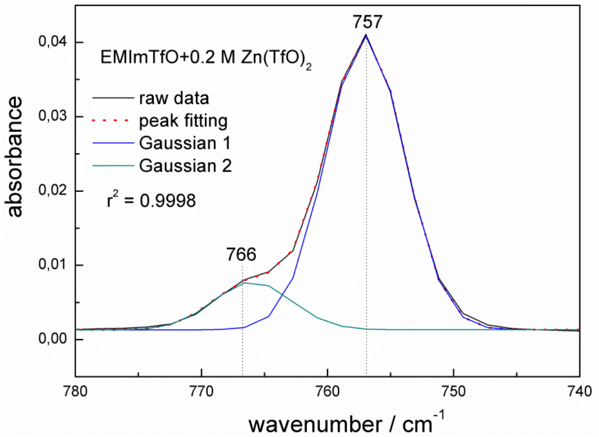

Fig. 3.8.7 *Raman spectra of 0.2 M* $Zn(TfO)_2$*/[EMIm]TfO between 740 and 780* cm^{-1}*. The spectrum was deconvoluted into two bands. The band at 757* cm^{-1} *is attributed to free* TfO^{-} *anions and the band at 766* cm^{-1} *is assigned to coordinated* TfO^{-} *anions.*

3.8.7 Polarities of [EMIm]TfO+water mixtures

Upon addition of 10% water (corresponding to a roughly 1 ([EMIm]TfO) : 1 (H_2O) in molar ratio) to 0.2 M $Zn(TfO)_2$/[EMIm]TfO solutions, a precipitate can be found on the bottom of the beaker. This process is very slow and it can take one week or even more. We found a similar phenomenon upon dissolving copper triflate, tin triflate and nickel triflate (TfO) in [EMIm]TfO, respectively, followed by addition of 10% water. Photos of the precipitates are shown in Fig. 3.8.8. The Zn precipitate was isolated and analyzed by XRD, XPS and EDX. The XRD result gave no peaks, showing that the isolated precipitate is amorphous. Both the XPS and EDX confirmed that the obtained precipitate contains Zn, S, F, and O. The precipitate is hydrated $Zn(TfO)_2$. In neat [EMIm]TfO, the $[EMIm]^+$ cations are hydrogen bonded to the TfO^- anions through C(2)H···A and/or C(4,5)H···A (A: anion). The presence of water disturbs the hydrogen bond network of the ionic liquid, affecting the polarity of the solution. We did not observe this precipitation at water contents below or above 10%. Only in close proximity (10 v/v% - roughly 1: 1 in molar ratio of the ionic liquid to water), the dissolved Zn salts are precipitated. Both the ionic liquid [EMIm]TfO and water are good solvents for $Zn(TfO)_2$. Without a detailed analysis of the precipitate we can not speculate on its composition, but, obviously, with this composition the polarity of the IL+water mixture is disturbed such that the Zn salt precipitates. Such polarizing/depolarizing effects in ionic liquid+water mixtures based on calculations were reported in literature [154-156]. They all reveal that water molecules get depolarized by the ionic liquid in mixtures of 1-ethyl-3-methylimidazolium acetate with water [154], mono-methylammonium nitrate with water [155] and 1-ethyl-3-methylimidazolium chloride with water [156], respectively. The study of interactions between [EMIm]TfO, water and dissolved salts is crucial not only for a fundamental understanding of the structure and physicochemical properties of the mixtures, but also for a practical use of the mixtures.

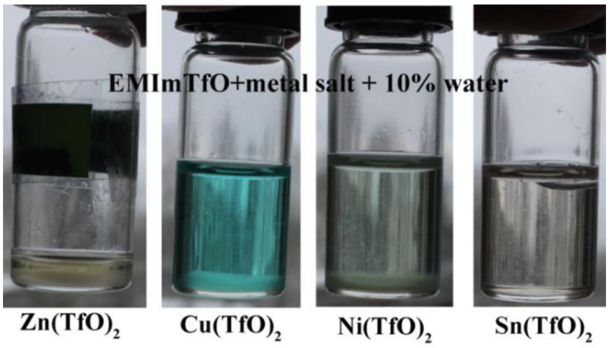

Fig. 3.8.8 *Photos of the solutions of 0.2 M $Zn(TfO)_2$/[EMIm]TfO+10% water, 0.2 M $Cu(TfO)_2$/[EMIm]TfO+10% water, saturated $Ni(TfO)_2$/[EMIm]TfO+10% water and saturated $Sn(TfO)_2$/[EMIm]TfO+10% water.*

3.8.8 The interaction of $[EMIm]^+$ and $[Py_{1,4}]^+$ cations with TfO^- anions in comparison

The FIR spectra of [EMIm]TfO and of $[Py_{1,4}]TfO$ between 30 and 300 cm^{-1} are shown in Fig. 3.8.9. The vibrational bands at about 210 cm^{-1} are due to the rocking modes of CF_3 (ρCF_3) and only slightly shifted by ~ 1 cm^{-1}. The signals around 240-250 cm^{-1}, which only appeared in [EMIm]TfO, can be assigned to the out-of-plane bending mode of the CH_3-(N) methyl group in the imidazolium cation. The low frequency vibrational bands below 200 cm^{-1} are assigned to the cation-anion interaction. The peak is located at around 88 cm^{-1} in [EMIm]TfO and red shifted to 76 cm^{-1} in $[Py_{1,4}]TfO$. The results suggest that $[EMIm]^+$ has stronger hydrogen bonds to TfO^- anions than $[Py_{1,4}]^+$ and the strength of the interaction between $[Py_{1,4}]^+$ and TfO^- is weaker in comparison. The difference in the interaction between cations and anions should also result in a different solvation of zinc ions.

3.8.9 The solvation of zinc ions in $[Py_{1,4}]TfO$

Raman spectra of $[Py_{1,4}]TfO$ with different amounts of $Zn(TfO)_2$ between 740 and 780 cm^{-1} are shown in Fig. 3.8.10. The average number of TfO^- coordinated to each Zn^{2+} ions as calculated above is 4.5 in $[Py_{1,4}]TfO$. The results suggest that in comparison to [EMIm]TfO more TfO^- anions are associated to Zn^{2+}. The difference can be attributed to the different cation-anion interactions occurring in these two ionic liquids. The weaker hydrogen bond between $[Py_{1,4}]^+$ and TfO^- seems to lead to an enhanced association of TfO^- anions with zinc ions. The species present in [EMIm]TfO are $[Zn(TfO)_4]^{2-}$ and $[Zn(TfO)_3]^-$, while a mixture of $[Zn(TfO)_4]^{2-}$ and $[Zn(TfO)_5]^{3-}$ is present in $[Py_{1,4}]TfO$. The difference of zinc species present in the two ionic liquids may also account for their different electrochemical performance and morphology of zinc deposits. The deposition of zinc from $[Py_{1,4}]TfO$ needs larger overpotentials than that one from [EMIm]TfO and nanocrystalline zinc is obtained from $[Py_{1,4}]TfO$ while microstructured zinc is obtained from [EMIm]TfO, which also has to do with interfacial reactions.

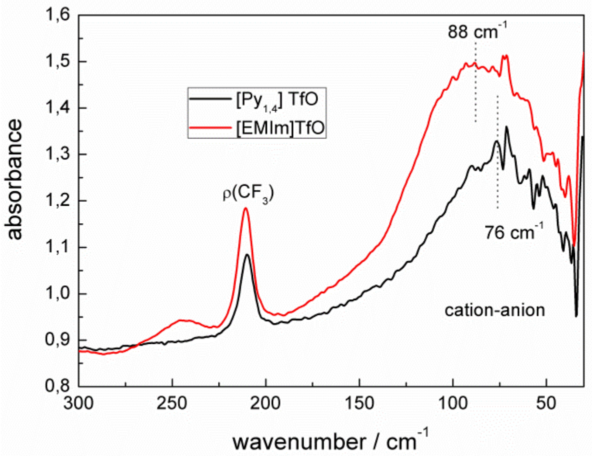

Fig. 3.8.9 *FIR spectra of [EMIm]TfO and of [Py$_{1,4}$]TfO between 30 and 300 cm^{-1}.*

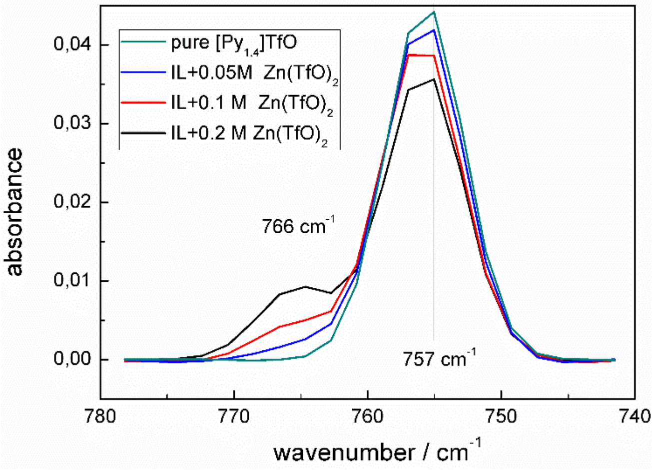

Fig. 3.8.10 *Raman spectra of [Py$_{1,4}$]TfO with different amounts of Zn(TfO)$_2$ between 740 and 780 cm^{-1}.*

3.8.10 Conclusions

The bulk coordination of [EMIm]TfO, [EMIm]TfO+water mixtures and the solvation of zinc ions were investigated by FT-IR and Raman spectroscopy. In neat [EMIm]TfO, imidazolium cations and TfO$^-$ anions are hydrogen bonded through C(2)…H and/or C(4,5)…H. If water is added, the bulk interaction networks between cations and anions are interrupted by association with water molecules and the structure is changed from ionic liquid like to aqueous like, the more water is added.

The solvation of Zn ions in ionic liquid and in ionic liquid+water mixtures was investigated by Raman spectroscopy. The vibrational band at 757 cm^{-1} is a probe for “free” TfO$^-$ anions. Upon addition of Zn salts, a new band appears at 766 cm^{-1} in the case of [EMIm]TfO which is assigned to Zn coordinated TfO^{-}. The average number of coordinated TfO^{-} per Zn^{2+} cation (n) is estimated to be 3.8, which indicates $[Zn(TfO)_4]^{2-}$ and $[Zn(TfO)_3]^{-}$. However, in the presence of water, only one peak is observed at 759 cm^{-1}, indicating that the Zn speciation is different, presumably Zn^{2+} ions are mainly associated with water. In $[Py_{1,4}]TfO$, the average coordination number is 4.5. The species present in $[Py_{1,4}]TfO$ are likely a mixture of $[Zn(TfO)_4]^{2-}$ and $[Zn(TfO)_5]^{3-}$.

4. Summary

In the present thesis the electrodeposition of Zn films from ionic liquids and ionic liquid+water mixtures was studied. The effect of an additive on the Zn deposition was also investigated. Macroporous structured zinc and free standing zinc nanowires were synthesized. In addition, Cu-Zn and Zn-Sn films and free standing nanowires were synthesized. Zn electrodeposition in the under- and overpotential regime was investigated by means of *in situ* Scanning Tunneling Microscopy (STM). The solvation properties of Zn^{2+} in the ionic liquids and ionic liquid+water mixtures were investigated by Raman and FTIR spectroscopy. Finally, the deposition/stripping cycling behavior of Zn in ionic liquid polymer gel electrolytes were examined.

The essential results of the present study can be summarized as follows:

- The electrodeposition of zinc films from 1-butyl-1-methylpyrrolidinium trifluoromethylsulfonate, $[Py_{1,4}]$TfO, and 1-ethyl-3-methylimidazolium trifluoromethylsulfonate, [EMIm]TfO, was studied. Nanocrystalline Zn deposits can be obtained in $[Py_{1,4}]$TfO, while microcrystalline Zn deposits were obtained from [EMIm]TfO. The addition of water has a great influence on the electrochemical behavior of Zn and the resultant morphologies of the Zn deposits. The additive 1,2-dimethyl-3-(trifluoromethyl)-1H-pyrazol-2-ium trifluoromethylsulfonate, can be strongly absorbed on the electrode surface and inhibit the Zn deposition, resulting in nanocrystalline Zn deposits.

- Highly ordered two- or three-dimensional macroporous zinc films were made by electrodeposition from the ionic liquid $[Py_{1,4}]$TfO using polystyrene (PS) spheres as templates. The obtained macroporous films showed diffractive light when illuminated with white light. Vertically aligned arrays of zinc nanowires were synthesized by electrochemical deposition into ion track-etched polycarbonate membranes in the ionic liquid [EMIm]TfO. These nanostructured zinc materials might be potential anode candidates for future generation lithium ion batteries or Zn based batteries.

- The initial stages of Zn electrodeposition in the underpotential (UPD) and overpotential (OPD) deposition regimes were investigated by *in situ* STM. First, monoatomically high Zn islands grow on the Au(1 1 1) surface to form a thin Zn layer in the UPD regime. Upon further reducing of the potential, bulk Zn deposition sets in and a 3D layer is obtained. Furthermore, *in situ* STM images reveal evidence of Au-Zn surface alloying after dissolution of the deposited Zn. The study also shows that the gold surface gets somehow activated by electrodeposition and stripping of zinc.

- An ionic liquid-based polymer gel electrolyte is prepared by combining the ionic liquid [Py$_{1,4}$]TfO with Zn(TfO)$_2$ and poly(vinylidene fluoride-co-hexafluoropropylene)(PVdF-HFP). The ionic liquid polymer gel electrolyte exhibits good conductivity (2.2 mS cm^{-1}) and good mechanical stability. The gel electrolyte exhibits a promising electrochemical stability and allows a quasi-reversible zinc deposition/stripping. The morphology of the zinc deposits after 10 cycles of zinc deposition/stripping is compact and dense, and deposits without any dendrite formation can be obtained. The quasi-reversibility of the electrochemical deposition/stripping of zinc in the ionic liquid polymer gel electrolyte is of interest for rechargeable zinc-based batteries.

- The interactions between the ionic liquid [EMIm]TfO and water, and the solvation structure of zinc in the ionic liquid (IL) and IL+water mixtures were studied by FTIR and Raman spectroscopy. The strong hydrogen bonding network between cations and anions present in the IL was modified and largely disturbed by addition of water. The structure and physicochemical properties of the [EMIm]TfO+water mixtures was strongly dependent on the interactions between cations, anions and water. The Zn^{2+} coordinated environment was changed in the presence of water. Zn^{2+} cations are more likely to associate with water molecular rather than with TfO^{-}. A comparative study of imidazolium and pyrrolidinium cation-anion interactions shows that the cation-anion interaction strength in [EMIm]TfO ionic liquid is stronger than that in [Py$_{1,4}$]TfO ionic liquid, which results in different physical properties of the two ionic liquids (melting point and viscosity) and coordination environments of the Zn^{2+}.

5 Outlook

This thesis has presented some fundamental information on the electrodeposition of zinc from ionic liquids. However, there are still some issues to be addressed in order to fully understand the systems for energy storage applications.

First, the zinc electrodeposition from the ionic liquids solution requires a large overpotential to drive the nucleation process. Although increasing the temperature of the system can significantly increase the diffusion behavior of Zn^{2+} and reduce the overpotential, the development of new electrolytes with better diffusion properties and lower overpotential will improve the performance of the electrolyte system for rechargeable zinc based battery applications.

Secondly, it has been shown in this study that additives have a strong effect on the electrodeposition of zinc. However, the role of additives on the deposition behavior from ionic liquid electrolytes is still unknown. The additive can absorb on the electrode surface or form complexes with the metal species. As the ionic liquid can also adsorb on the electrode surface, the *in situ* STM images cannot distinguish them from each other easily. More efforts are required to understand the role of various additives or impurities on the deposition of metals.

Finally, it was found that pyrrolidinium ions rather lead to nanocrystalline zinc deposits, whereas imidazolium ions rather lead to microcrystalline zinc deposits. Such morphology can be caused by ionic liquid solvation layers adsorb on the electrode surface. While the FTIR and Raman spectroscopy results revealed that the interaction between cations and anions are different, resulting in different zinc solvation structure in the ionic liquids. Understanding the relationship between the metal speciation, the interaction between cations and anions, electrodeposition mechanism and deposit morphology is critical for designing proper ionic liquids in better applications.

6 References

1. P. Walden, *Bulletin of the Russian Academy of Sciences*, 1914, 405-422.
2. F. H. Hurley and T. P. Wier, *Journal of The Electrochemical Society*, 1951, **98**, 207-212.
3. J. A. Boon, J. A. Levisky, J. L. Pflug and J. S. Wilkes, *Journal of Organic Chemistry*, 1986, **51**, 480-483.
4. J. E. Enderby and G. W. Neilson, *Advances in Physics*, 1980, **29**, 323-365.
5. R. J. Gale and R. A. Osteryoung, *Electrochimica Acta*, 1980, **25**, 1527-1529.
6. M. J. Earle and K. R. Seddon, *Pure and Applied Chemistry*, 2000, **72**, 1391-1398.
7. J. G. Huddleston, A. E. Visser, W. M. Reichert, H. D. Willauer, G. A. Broker and R. D. Rogers, *Green Chemistry*, 2001, **3**, 156-164.
8. J. G. Huddleston, H. D. Willauer, R. P. Swatloski, A. E. Visser and R. D. Rogers, *Chemical Communications*, 1998, 1765-1766.
9. R. Sheldon, *Chemical Communications*, 2001, 2399-2407.
10. T. Welton, *Chemical Reviews*, 1999, **99**, 2071-2083.
11. J. Dupont, R. F. de Souza and P. A. Z. Suarez, *Chemical Reviews*, 2002, **102**, 3667-3691.
12. N. V. Plechkova and K. R. Seddon, *Chemical Society Reviews*, 2008, **37**, 123-150.
13. R. D. Rogers and K. R. Seddon, *Science*, 2003, **302**, 792-793.
14. R. P. Swatloski, S. K. Spear, J. D. Holbrey and R. D. Rogers, *Journal of the American Chemical Society*, 2002, **124**, 4974-4975.
15. S. Zhang, N. Sun, X. He, X. Lu and X. Zhang, *Journal of Physical and Chemical Reference Data*, 2006, **35**, 1475-1517.
16. Y. U. Paulechka, D. H. Zaitsau, G. J. Kabo and A. A. Strechan, *Thermochimica Acta*, 2005, **439**, 158-160.
17. C. Ye, W. Liu, Y. Chen and L. Yu, *Chemical Communications*, 2001, 2244-2245.
18. C.-M. Jin, C. Ye, B. S. Phillips, J. S. Zabinski, X. Liu, W. Liu and J. M. Shreeve, *Journal of Materials Chemistry*, 2006, **16**, 1529-1535.
19. J. F. Brennecke and E. J. Maginn, *AIChE Journal*, 2001, **47**, 2384-2389.
20. M. E. V. Valkenburg, R. L. Vaughn, M. Williams and J. S. Wilkes, *Thermochimica Acta*, 2005, **425**, 181-188.
21. A. Noda, K. Hayamizu and M. Watanabe, *Journal of Physical Chemistry B*, 2001, **105**, 4603-4610.

22. K. Tochigi and H. Yamamoto, *Journal of Physical Chemistry C*, 2007, **111**, 15989-15994.

23. J. A. Widegren and J. W. Magee, *Journal of Chemical and Engineering Data*, 2007, **52**, 2331-2338.

24. M. Hayyan, F. S. Mjalli, M. A. Hashim, I. M. Alnashef and T. X. Mei, *Journal of Industrial and Engineering Chemistry*, 2013, **19**, 106-112.

25. F. Endres, A. P. Abbott, D. R. MacFarlane, Electrodeposition from Ionic Liquids, Wiley-VCH, 2008.

26. F. Endres, M. Bukowski, R. Hempelmann and H. Natter, *Angewandte Chemie International Edition*, 2003, **42**, 3428-3430.

27. A. P. Abbott and K. J. McKenzie, *Physical Chemistry Chemical Physics*, 2006, **8**, 4265-4279.

28. F. Endres and S. Zein El Abedin, *Physical Chemistry Chemical Physics*, 2006, **8**, 2101-2116.

29. J.-K. Chang, S.-Y. Chen, W.-T. Tsai, M.-J. Deng and I. W. Sun, *Electrochemistry Communications*, 2007, **9**, 1602-1606.

30. M.-J. Deng, P.-Y. Chen and I. W. Sun, *Electrochimica Acta*, 2007, **53**, 1931-1938.

31. S. I. Hsiu, C. C. Tai and I. W. Sun, *Electrochimica Acta*, 2006, **51**, 2607-2613.

32. J. F. Huang and I. W. Sun, *Journal of the Electrochemical Society*, 2004, **151**, C8-C14.

33. J. F. Huang and I. W. Sun, *Electrochimica Acta*, 2004, **49**, 3251-3258.

34. C. C. Tai, F. Y. Su and I. W. Sun, *Electrochimica Acta*, 2005, **50**, 5504-5509.

35. M. H. Yang and I. W. Sun, *Journal of Applied Electrochemistry*, 2003, **33**, 1077-1084.

36. A. P. Abbott, J. C. Barron, K. S. Ryder and D. Wilson, *Chemistry-A European Journal*, 2007, **13**, 6495-6501.

37. A. P. Abbott, G. Capper, D. L. Davies and R. Rasheed, *Inorganic Chemistry*, 2004, **43**, 3447-3452.

38. A. P. Abbott, G. Capper, K. J. McKenzie and K. S. Ryder, *Journal of Electroanalytical Chemistry*, 2007, **599**, 288-294.

39. A. P. Abbott, K. El Ttaib, G. Frisch, K. J. McKenzie and K. S. Ryder, *Physical Chemistry Chemical Physics*, 2009, **11**, 4269-4277.

40. A. P. Abbott, K. S. Ryder and U. Koenig, *Transactions of the Institute of Metal Finishing*, 2008, **86**, 196-204.

41. M. Armand, F. Endres, D. R. MacFarlane, H. Ohno and B. Scrosati, *Nature Materials*, 2009, **8**, 621-629.

42. F. Endres, *ChemPhysChem*, 2002, **3**, 144-154.
43. F. Endres, *Zeitschrift Für Physikalische Chemie-International Journal of Research in Physical Chemistry & Chemical Physics*, 2004, **218**, 255-284.
44. S. Zein El Abedin, E.M. Moustafa, H. Natter, R. Hempelmann and F. Endres, *Electrochemistry Communications* 2005, **7**, 1111-1116.
45. S. Zein El Abedin and F. Endres, *ChemPhysChem*, 2006, **7**, 58-61.
46. W. R. Pitner and C. L. Hussey, *Journal of the Electrochemical Society*, 1997, **144**, 3095-3103.
47. P. Y. Chen and I. W. Sun, *Electrochimica Acta*, 2001, **46**, 1169-1177.
48. S. I. Hsiu, J. F. Huang, I. W. Sun, C. H. Yuan and J. Shiea, *Electrochimica Acta*, 2002, **47**, 4367-4372.
49. Y. F. Lin and I. W. Sun, *Journal of the Electrochemical Society*, 1999, **146**, 1054-1059.
50. A. P. Abbott, J. C. Barron and K. S. Ryder, *Transactions of the Institute of Metal Finishing*, 2009, **87**, 201-207.
51. A. P. Abbott, G. Capper, D. L. Davies, R. K. Rasheed and V. Tambyrajah, *Transactions of the Institute of Metal Finishing*, 2001, **79**, 204-206.
52. T. J. Simons, D. R. MacFarlane, M. Forsyth and P. C. Howlett, *ChemElectroChem*, 2014, **1**, 1688-1697.
53. T. J. Simons, A. A. J. Torriero, P. C. Howlett, D. R. MacFarlane and M. Forsyth, *Electrochemistry Communications*, 2012, **18**, 119-122.
54. M. J. Deng, P. C. Lin, J. K. Chang, J. M. Chen and K. T. Lu, *Electrochimica Acta*, 2011, **56**, 6071-6077.
55. N. Doan, T. Vainikka, E. L. Rautama, K. Kontturi and C. Johans, *International Journal of Electrochemical Science*, 2012, **7**, 12034-12044.
56. S. Ernst, M. C. Henstridge and R. G. Compton, *Journal of Solid State Electrochemistry*, 2012, **16**, 2329-2333.
57. C. C. Ho, J. W. Evans and P. K. Wright, *Journal of Micromechanics and Microengineering*, 2010, **20**, 9.
58. T. J. Simons, P. C. Howlett, A. A. J. Torriero, D. R. MacFarlane and M. Forsyth, *The Journal of Physical Chemistry C*, 2013, **117**, 2662-2669.
59. T. J. Simons, P. M. Bayley, Z. Zhang, P. C. Howlett, D. R. MacFarlane, L. A. Madsen and M. Forsyth, *The Journal of Physical Chemistry B*, 2014, **118**, 4895-4905.
60. M. Xu, D. G. Ivey, Z. Xie, W. Qu and E. Dy, *Electrochimica Acta*, 2013, **97**, 289-295.

61. R. Fukui, Y. Katayama and T. Miura, *Electrochimica Acta*, 2011, **56**, 1190-1196.
62. Y. L. Zhu, Y. Katayama and T. Miura, *Electrochimica Acta*, 2012, **85**, 622-627.
63. J. Sniekers, N. R. Brooks, S. Schaltin, L. Van Meervelt, J. Fransaer and K. Binnemans, *Dalton Transactions*, 2014, **43**, 1589-1598.
64. G. H. Lane, A. S. Best, D. R. MacFarlane, M. Forsyth and A. F. Hollenkamp, *Electrochimica Acta*, 2010, **55**, 2210-2215.
65. N. M. Pereira, C. M. Pereira and A. Fernando Silva, *ECS Electrochemistry Letters*, 2012, **1**, D5-D7.
66. A. P. Abbott, J. C. Barron, G. Frisch, K. S. Rydera and A. Fernando Silva, *Electrochim Acta*, 2011, **56**, 5272-5279.
67. N. M. Pereira, P. M. V. Fernandes, C. M. Pereira and A. Fernando Silva, *Journal of the Electrochemical Society*, 2012, **159**, D501-D506.
68. J. C. Ballesteros, P. Diaz-Arista, Y. Meas, R. Ortega and G. Trejo, *Electrochimica Acta*, 2007, **52**, 3686-3696.
69. A. Gomes and M. I. D. Pereira, *Electrochimica Acta*, 2006, **51**, 1342-1350.
70. J.-C. Hsieh, C.-C. Hu and T.-C. Lee, *Journal of the Electrochemical Society*, 2008, **155**, D675-D681.
71. M. A. M. Ibrahim and E. M. A. Omar, *Surface & Coatings Technology*, 2013, **226**, 7-16.
72. M. C. Li, L. L. Jiang, W. Q. Zhang, Y. H. Qian, S. Z. Luo and J. N. Shen, *Journal of Solid State Electrochemistry*, 2007, **11**, 549-553.
73. L. E. Moron, A. Mendez, J. C. Ballesteros, R. Antano-Lopez, G. Orozco, Y. Meas, R. Ortega-Borges and G. Trejo, *Journal of the Electrochemical Society*, 2011, **158**, D435-D444.
74. K. O. Nayana, T. V. Venkatesha, B. M. Praveen and K. Vathsala, *Journal of Applied Electrochemistry*, 2011, **41**, 39-49.
75. G. Trejo, H. Ruiz, R. O. Borges and Y. Meas, *Journal of Applied Electrochemistry*, 2001, **31**, 685-692.
76. A. K. Padhi, K. S. Nanjundaswamy and J. B. Goodenough, *Journal of The Electrochemical Society*, 1997, **144**, 1188-1194.
77. H. Li, X. Huang, L. Chen, Z. Wu and Y. Liang, *Electrochemical and Solid-State Letters*, 1999, **2**, 547-549.
78. C. K. Chan, H. Peng, G. Liu, K. Mcilwrath, X. F. Zhang, R. A. Huggins and Y. Cui, *Nature Nanotechnology*, 2008, **3**, 31-35.

79. K. Xu, *Chemical Reviews*, 2004, **104**, 4303-4417.

80. M. S. Whittingham, *Chemical Reviews*, 2004, **104**, 4271-4301.

81. B. Scrosati and J. Garche, *Journal of Power Sources*, 2010, **195**, 2419-2430.

82. M. Kar, T. J. Simons, M. Forsyth and D. R. MacFarlane, *Physical Chemistry Chemical Physics*, 2014, **16**, 18658-18674.

83. Y.-S. Ye, J. Rick and B.-J. Hwang, *Journal of Materials Chemistry A*, 2013, **1**, 2719-2743.

84. G. G. Kumar and S. Sampath, *Solid State Ionics*, 2003, **160**, 289-300.

85. G. G. Kumar and S. Sampath, *Journal of the Electrochemical Society*, 2003, **150**, A608-A615.

86. S. Ikeda, Y. Mori, Y. Furuhashi and H. Masuda, *Solid State Ionics*, 1999, **121**, 329-333.

87. A. Lewandowski and I. Majchrzak, *Journal of New Materials for Electrochemical Systems*, 2001, **4**, 135-141.

88. A. Hofmann, M. Schulz and T. Hanemann, *Electrochimica Acta*, 2013, **89**, 823-831.

89. D. F. Miranda, C. Versek, M. T. Tuominen, T. P. Russell and J. J. Watkins, *Macromolecules*, 2013, **46**, 9313-9323.

90. M. Suleman, Y. Kumar and S. A. Hashmi, *Journal of Physical Chemistry B*, 2013, **117**, 7436-7443.

91. I. Stepniak, *Journal of Power Sources*, 2014, **247**, 112-116.

92. H. Ye, J. Huang, J. J. Xu, A. Khalfan and S. G. Greenbaum, *Journal of the Electrochemical Society*, 2007, **154**, A1048-A1057.

93. W. Lu, K. Henry, C. Turchi and J. Pellegrino, *Journal of the Electrochemical Society*, 2008, **155**, A361-A367.

94. P. Pei, K. Wang and Z. Ma, *Applied Energy*, 2014, **128**, 315-324.

95. F. Kong, *Electrochimica Acta*, 2012, **68**, 198-201.

96. X. Wang, P. J. Sebastian, M. A. Smit, H. Yang and S. A. Gamboa, *Journal of Power Sources*, 2003, **124**, 278-284.

97. X.-Z. Yuan, X. Li, W. Qu, D. G. Ivey and H. Wang, *ECS Transactions*, 2011, **35**, 11-20.

98. F. Endres, O. Hoefft, N. Borisenko, L. H. Gasparotto, A. Prowald, R. Al-Salman, T. Carstens, R. Atkin, A. Bund and S. Zein El Abedin, *Physical Chemistry Chemical Physics*, 2010, **12**, 1724-1732.

99. R. Atkin, S. Zein El Abedin, R. Hayes, L. H. S. Gasparotto, N. Borisenko and F. Endres, *Journal of Physical Chemistry C*, 2009, **113**, 13266-13272.

100. R. Hayes, N. Borisenko, B. Corr, G. B. Webber, F. Endres and R. Atkin, *Chemical Communications*, 2012, **48**, 10246-10248.

101. D. Borissov, A. Pareek, F. U. Renner and M. Rohwerder, *Physical Chemistry Chemical Physics*, 2010, **12**, 2059-2062.

102. P. Scherrer, *Göttinger Nachrichten Gesellschaft*, 1918, **2**, 98-100.

103. M. Hartmann, T. Clark and R. van Eldik, *Journal of The American Chemical Society*, 1997, **119**, 7843-7850.

104. A. M. O'Mahony, D. S. Silvester, L. Aldous, C. Hardacre and R. G. Compton, *Journal of Chemical and Engineering Data*, 2008, **53**, 2884-2891.

105. M. Tariq, M. G. Freire, B. Saramago, J. A. P. Coutinho, J. N. C. Lopes and L. P. N. Rebelo, *Chemical Society Reviews*, 2012, **41**, 829-868.

106. S. Zein El Abedin, A. Prowald and F. Endres, *Electrochemistry Communications*, 2012, **18**, 70-73.

107. A. Prowald, S. Zein El Abedin, N. Borisenko and F. Endres, *Zeitschrift Für Physikalische Chemie-International Journal of Research In Physical Chemistry & Chemical Physics*, 2012, **226**, 121-128.

108. L. Ding, Y. Wang, W. Ma, C. He, T. Xie and Y. Can, *Applied Surface Science*, 2008, **254**, 6775-6778.

109. B. H. Juarez, C. Lopez and C. Alonso, *Journal of Physical Chemistry B*, 2004, **108**, 16708-16712.

110. C. Schönenberger, B. M. I. van der Zande, L. G. J. Fokkink, M. Henny, C. Schmid, M. Krüger, A. Bachtold, R. Huber, H. Birk and U. Staufer, *The Journal of Physical Chemistry B*, 1997, **101**, 5497-5505.

111. M. Motoyama, Y. Fukunaka, T. Sakka and Y. H. Ogata, *Electrochimica Acta*, 2007, **53**, 205-212.

112. Y. Liang, C. Zhen, D. Zou and D. Xu, *Journal of the American Chemical Society*, 2004, **126**, 16338-16339.

113. Z. Liu, S. Zein El Abedin and F. Endres, *Electrochimica Acta*, 2013, **89**, 635-643.

114. P. Giridhar, S. Zein El Abedin and F. Endres, *Journal of Solid State Electrochemistry*, 2012, **16**, 3487-3497.

115. P. Y. Chen, M. C. Lin and I. W. Sun, *Journal of Electrochemical Society*, 2000, **147**, 3350-3355.

116. P. De Vreese, A. Skoczylas, E. Matthijs, J. Fransaer and K. Binnemans, *Electrochimica Acta*, 2013, **108**, 788-794.

117. C. Rousse, S. Beaufils and P. Fricoteaux, *Electrochimica Acta*, 2013, **107**, 624-631.

118. Z. Liu, A. Prowald, S. Zein El Abedin and F. Endres, *Journal of Solid State Electrochemistry*, 2013, **17**, 1185-1188.

119. Z. Liu, S. Zein E. Abedin, M. Shapouri Ghazvini and F. Endres, *Physical Chemistry Chemical Physics*, 2013, **15**, 11362-11367.

120. S. Zein El Abedin, E. M. Moustafa, R. Hempelmann, H. Natter and F. Endres, *ChemPhysChem*, 2006, **7**, 1535-1543.

121. J. Shu, M. Shui, F. Huang, D. Xu, Y. Ren, L. Hou, J. Cui and J. Xu, *Electrochimica Acta*, 2011, **56**, 3006-3014.

122. C. Peng, L. Yang, S. Fang, J. Wang, Z. Zhang, K. Tachibana, Y. Yang and S. Zhao, *Journal of Applied Electrochemistry*, 2010, **40**, 653-662.

123. F. Endres, N. Borisenko, S. Zein El Abedin, R. Hayes and R. Atkin, *Faraday Discussions*, 2012, **154**, 221-233.

124. L. H. S. Gasparotto, N. Borisenko, O. Hoefft, R. Al-Salman, W. Maus-Friedrichs, N. Bocchi, S. Zein El Abedin and F. Endres, *Electrochimica Acta*, 2009, **55**, 218-226.

125. T. Carstens, R. Hayes, S. Zein El Abedin, B. Corr, G. B. Webber, N. Borisenko, R. Atkin and F. Endres, *Electrochimica Acta*, 2012, **82**, 48-59.

126. Y.-Z. Su, J.-W. Yan, M.-G. Li, Z.-X. Xie, B.-W. Mao and Z.-Q. Tian, *Zeitschrift Für Physikalische Chemie-International Journal of Research in Physical Chemistry & Chemical Physics*, 2012, **226**, 979-994.

127. R. Hayes, N. Borisenko, M. K. Tam, P. C. Howlett, F. Endres and R. Atkin, *Journal of Physical Chemistry C*, 2011, **115**, 6855-6863.

128. J.-J. Max and C. Chapados, *The Journal of Chemical Physics*, 2010, **133**.

129. S. Gopalakrishnan, D. Liu, H. C. Allen, M. Kuo and M. J. Shultz, *Chemical Review*, 2006, **106**, 1155-1175.

130. J.-B. Brubach, A. Mermet, A. Filabozzi, A. Gerschel and P. Roy, *The Journal of Chemical Physics*, 2005, **122**.

131. S. Y. Venyaminov and F. G. Prendergast, *Analytical Biochemistry*, 1997, **248**, 234-245.

132. W. B. Fischer, A. Fedorowicz and A. Koll, *Physical Chemistry Chemical Physics*, 2001, **3**, 4228-4234.

133. L. Cammarata, S. G. Kazarian, P. A. Salter and T. Welton, *Physical Chemistry Chemical Physics*, 2001, **3**, 5192-5200.

134. T. Köddermann, C. Wertz, A. Heintz and R. Ludwig, *ChemPhysChem*, 2006, **7**, 1944-1949.

135. Y.-Z. Zheng, N.-N. Wang, J.-J. Luo, Y. Zhou and Z.-W. Yu, *Physical Chemistry Chemical Physics*, 2013, **15**, 18055-18064.

136. Y. Jeon, J. Sung, D. Kim, C. Seo, H. Cheong, Y. Ouchi, R. Ozawa and H. Hamaguchi, *The Journal of Physical Chemistry B*, 2008, **112**, 923-928.

137. P. Stange, K. Fumino and R. Ludwig, *Angewandte Chemie International Edition*, 2013, **52**, 2990-2994.

138. A. A. Niazi, B. D. Rabideau and A. E. Ismail, *The Journal of Physical Chemistry B*, 2013, **117**, 1378-1388.

139. Y. Umebayashi, T. Fujimori, T. Sukizaki, M. Asada, K. Fujii, R. Kanzaki and S. Ishiguro, *The Journal of Physical Chemistry A*, 2005, **109**, 8976-8982.

140. J.-M. Andanson and A. Baiker, *The Journal of Physical Chemistry C*, 2013, **117**, 12210-12217.

141. D. H. Johnston and D. F. Shriver, *Inorganic Chemistry*, 1993, **32**, 1045-1047.

142. S. Tsuzuki, H. Tokuda, K. Hayamizu and M. Watanabe, *The Journal of Physical Chemistry B*, 2005, **109**, 16474-16481.

143. K. Fumino, S. Reimann and R. Ludwig, *Physical Chemistry Chemical Physics*, 2014.

144. K. Fumino, A. Wulf and R. Ludwig, *Angewandte Chemie International Edition*, 2008, **47**, 3830-3834.

145. K. Fumino, K. Wittler and R. Ludwig, *The Journal of Physical Chemistry B*, 2012, **116**, 9507-9511.

146. A. Wulf, K. Fumino and R. Ludwig, *Angewandte Chemie International Edition*, 2010, **49**, 449-453.

147. T. Köddermann, K. Fumino, R. Ludwig, J. N. Canongia Lopes and A. A. H. Pádua, *ChemPhysChem*, 2009, **10**, 1181-1186.

148. K. Fumino, A. Wulf and R. Ludwig, *Physical Chemistry Chemical Physics*, 2009, **11**, 8790-8794.

149. K. Fumino, A. Wulf and R. Ludwig, *Angewandte Chemie International Edition*, 2009, **48**, 3184-3186.

150. Y. Umebayashi, T. Mitsugi, S. Fukuda, T. Fujimori, K. Fujii, R. Kanzaki, M. Takeuchi and S.-I. Ishiguro, *The Journal of Physical Chemistry B*, 2007, **111**, 13028-13032.
151. G. A. Giffin, A. Moretti, S. Jeong and S. Passerini, *Journal of Physical Chemistry C*, 2014, **118**, 9966-9973.
152. J. Kiefer, J. Fries and A. Leipertz, *Applied Spectroscopy*, 2007, **61**, 1306-1311.
153. C. M. Burba, N. M. Rocher and R. Frech, *The Journal of Physical Chemistry B*, 2009, **113**, 11453-11458.
154. M. Brehm, H. Weber, A. S. Pensado, A. Stark and B. Kirchner, *Physical Chemistry Chemical Physics*, 2012, **14**, 5030-5044.
155. S. Zahn, K. Wendler, L. Delle Site and B. Kirchner, *Physical Chemistry Chemical Physics*, 2011, **13**, 15083-15093.
156. C. Spickermann, J. Thar, S. B. C. Lehmann, S. Zahn, J. Hunger, R. Buchner, P. A. Hunt, T. Welton and B. Kirchner, *The Journal of Chemical Physics*, 2008, **129**.

List of abbreviations

$[EMIm]^+$	1-ethyl-3-methylimidazolium cation
$[Py_{1,4}]^+$	1-butyl-1-methylpyrrolidinium cation
CV	Cyclic voltammetry
$DCA^−$	Dicyanamide anion
FIR	Far infrared spectroscopy
FT-IR	Fourier Transform infrared spectroscopy
IL	Ionic liquid
NaCN	Sodium cyanide
NHE	Normal Hydrogen Electrode
$NTf_2^−$	Bis(trifluoromethylsulfonyl)imid anion
OCP	Open cycle potential
OER	Oxygen evolution reaction
ORR	Oxygen reduction reaction
PC	Polycarbonate
PEDOT	Poly(3,4-ethylenedioxythiophene)
PPP	Poly(para-phenylene)
PS	Polystyrene sphere
PVdF-HFP	Poly(vinylidenefluoride-hexafluoropropylene)
RE	Reference electrode
SEM	Scanning electron microscopy
STM	Scanning tunneling microscopy
$TfO^−$	Trifluoromethylsulfonate anion

VS.	Versus
XRD	X-ray Diffraction

Curriculum Vitae

Personal Information:

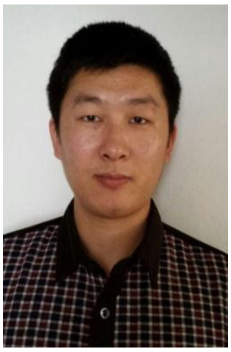

Name: Zhen Liu

Nationality: China

Marital Status: Married with one child

Sex: Male

Date of Birth: 06th. Nov. 1984

E.mail: zhenliu1984@gmail.com or zhen.liu@tu-clausthal.de

Address: Am Ehrenhain str. 7, Clausthal-Zellerfeld

Telephone: 017656576783

Languages: Chinese (mother language), English and a little German

Research experience:

PhD student (Wissenschaftlicher Mitarbeiter): Clausthal University of Technology

Feb. 2012 – Jun. 2015

Project: The electrochemistry of zinc in ionic liquids for rechargeable zinc-air batteries.

Project Assistant: Qingdao Institute of Bioenergy and Bioprocess Technology, Chinese Academic of Sciences (CAS) May 2011 – Jan. 2012

Project: Cellulose materials produced from ionic liquids solutions

Master degree: Institute of Process Engineering, CAS Sep. 2008 - May 2011

Project: Regeneration, Separation and Conversion of Biomass dissolved in Ionic Liquids

Bachelor degree: Zhengzhou University, China Sep. 2004 - July 2008

Major: Chemical Engineering and Technology

Publications within the framework of this thesis:

[A] Electrodeposition of zinc films from ionic liquids and ionic liquid/water mixtures, Z. Liu, S. Zein El Abedin, F. Endres, *Electrochimica Acta*, 2013, **89**, 635–643.

[B] Template-assisted electrodeposition of highly ordered macroporous zinc structures from an ionic liquid, Z. Liu, A. Prowald, S. Zein El Abedin, F. Endres, *Journal of Solid State Electrochemistry*, 2013, **17**, 1185–1188.

[C] Electrochemical synthesis of vertically aligned zinc nanowires using track-etched polycarbonate membranes as templates, Z. Liu, S. Zein El Abedin, M. Shapouri Ghazvini, F. Endres, *Physical Chemistry Chemical Physics*, 2013, **15**, 11362–11367.

[D] Electrodeposition of zinc-copper and zinc-tin films and free-standing nanowire arrays from ionic liquids, Z. Liu, S. Zein El Abedin, F. Endres, *ChemElectroChem*, 2015, **2**, 389–395.

[E] Influence of an additive on zinc electrodeposition in the ionic liquid 1-ethyl-3-methylimidazolium trifluoromethylsulfonate, Z. Liu, S. Zein El Abedin, N. Borisenko, F. Endres, *ChemElectroChem*, DOI: 10.1002/celc.201500108.

[F] Electrodeposition and stripping of zinc from an ionic liquid polymer gel electrolyte for rechargeable zinc-based batteries, Z. Liu, S. Zein El Abedin, F. Endres, *Journal of Solid State Electrochemistry*, 2014, **18**, 2683–2691.

[G] *In situ* STM study of zinc electrodeposition on Au (111) from the ionic liquid 1-ethyl-3-methylimidazolium trifluoromethylsulfonate, Z. Liu, N. Borisenko, S. Zein El Abedin, F. Endres, *Journal of Solid State Electrochemistry,* 2014, **18**, 2581–2587.

[H] Raman and FT-IR spectroscopic studies of 1-ethyl-3-methylimidazolium trifluoromethylsulfonate, its mixtures with water and the solvation of zinc ions,
Z. Liu, S. Zein El Abedin, F. Endres, *ChemPhysChem,* 2015, **16**, 970–977..

Acknowledgement

My stay at Clausthal University of Technology, Germany, has not only been an academic experience but also a fantastic journey in my life that has broadened my horizons, taught me many lessons and helped me grow intellectually as well as personally.

First, I especially would like to thank my supervisor Prof. Dr. Frank Endres for giving me the chance to work in his group, even though my performance in the beginning was not that good. I have very much appreciated his deep insight in the field of electrochemical aspects of ionic liquids. We have a lot of fruitful discussions, guiding me in the right direction along my research path. In addition, Prof. Endres has given me and my family a lot of help in the life. Thank you very much.

I would like to extend my appreciation to Dr. Sherif Zein El Abedin (Professor at NRC Dokki, Cairo, Egypt) for his continued guiding and kind help in my research.

I would like to express my sincere thanks to Dr. Natalia Borisenko for her kind help to pursue my investigations on electrochemical scanning tunnelling microscopy (STM).

I would like to thank my fellow group members for their kind help with my research or coursework.

My family has supported me so much through this process, and I honestly don’t know what I would have done without them.

I am very grateful to my parents for their love, kindness and great assistances. I hope that they will be proud of me.

Finally, I would like to thank my wife Na feng for her continuous support, encouragement, patience and for taking care of our child Andreas Yuxuan Liu. I would also like to thank my son, who keeps reminding me of what are the truly important matters in life.